ABSTRACT

Title of dissertation: JAMMING EFFECTS IN
GLASSES AND BIOPOLYMERS

Hongsuk Kang, Doctor of Philosophy, 2014

Dissertation directed by: Professor Devarajan Thirumalai
Chemical Physics Program
Institute for Physical Science and Technology,
Department of Chemistry and Biochemistry

In this dissertation, jamming effects in highly packed systems are studied in two specific materials: glasses and biopolymers in cellular environments. Suspensions consisting of highly charged colloids, which are well-known glassforming systems, are investigated using molecular dynamics simulations in order to test Random First Order Transition (RFOT) theory. I found that there is a critical volume fraction, ϕ_A, at which ergodictononergodic transitions for three dynamic observables take place in accordance with RFOT. Based on numerical observations, it is also proposed that the dynamic heterogeneity can be attributed to the violation of law of large numbers. In addition, the bond orientational order of colloidal suspensions and softspheres is discussed in the context of liquid-glass transitions. The response of biopolymers to a crowded environment is another interesting issue because 20-40% volume of a cell is occupied by various cellular components such as ribosomes and proteins in vivo. In this work, using low-friction langevin dynamics simulations with

explicit crowding particles, I examined the conformational change of biopolymers in the presence of crowders of various sizes and shapes. The simulation results reveal that cylindrical crowders induce much greater compaction of the polymers than spherical ones at low volume fractions and the stronger crowding effects disappear at higher volume fractions due to local nematic ordering of cylindrical particles. The reduction in the size of polymer is even more dramatic in a mixture of spherical and cylindrical shapes because of cooperative crowding effects explained by the phase separation of spheres and rodlike particles. Finally, the crowding effects of cellular components on bacterial chromosomes are estimated using a mixture of spherical crowders with the composition found in bacterial cytoplasms.

Jamming effects in glasses and biopolymers

by

Hongsuk Kang

Dissertation submitted to the Faculty of the Graduate School of the
University of Maryland, College Park in partial fulfillment
of the requirements for the degree of
Doctor of Philosophy
2014

Advisory Committee:
Professor Devarajan Thirumalai, Chair/Advisor
Professor Theodore R. Kirkpatrick
Professor Garegin Papoian
Professor John D. weeks
Professor David Fushman

Preface

In this dissertation, using dynamic simulations, I studied jamming effects in two different systems: colloidal suspensions and macromolecular crowdings. I aimed to clarify interesting questions that have not been studied in these systems to extend our knowledge for the thermodynamics of highly packed systems.

In chapter 1, I provide some descriptions of charateristic phenomena observed in the glasses and explain theoretical concepts being useful for a understanding of liquid-glass transitions. In chapter 2 and 3, I manifest the Random First Order Transition theory in Wigner glasses using the analysis of Brownian dynamics simulation results. I also investigate the role of bond orientational orders in the vitrification process for a mixture of soft-spheres and Wigner glasses. In chapter 4, I review recent literature regarding the effects of macromolecular crowdings on various biopolymers to address important questions. In chapter 5, I test a universal scaling law, which can be applied to RNAs and proteins, using a polymer model and simulations. In chapter 6, the system of a semi-flexible chain and polydisperse crowding particles are simulated to clarify the crowding effects of the polydisperse macromolecular crowdings on DNAs. The main text of this dissertation is ended with concluding remarks and future perspectives in chapter 7. In appendix A, I discuss the dependencies of glass formation dynamics on microscopic dynamics. Finally, Appendix B explains a multiple layered neighbor list algorithm, which is implemented in my simulations.

Dedication

To My Wife, Mijin

Totus tuus ego sum, et omnia mea tua sunt

Acknowledgments

At last, I would like to ascribe the largest credit to my wife, Mijin. Without her dedication, I would have not finished my Ph.D.

Table of Contents

List of Figures

List of Abbreviations

LGT	Liquid-Glass Transition
BOO	Bond Orientaional Order
RFOT	Random First Order Transition
MCT	Mode-Coupling Theory
PEG	Polyethylene Glycol
SPT	Scaled Particle Theory
SAW	Self Avoiding Walk
WLC	Worm-like Chain
IDP	Intrinsically Disordered Proteins
SS	Soft-Sphere
SC	Spherocylinder
τ_α	α-relaxation time

Chapter 1: Thermodynamics of highly packed system

1.1 Liquid-glass transition (LGT)

1.1.1 Charateristic phenomena of LGT

Glasses are interesting materials. Despite their wide practical uses in our daily lives, a fundamental understanding of glasses has been a great challenge to many chemical physicists and physical chemists [1–3]. Several important questions still remain unresolved and have gained significant attention from researches for several decades because of its profound significance in the establishment of thermodynamic theories. In this chapter, I will summarize some important phenomena and theoretical concepts that are useful to understand the thermodynamics of glasses.

Glasses are amorphous rigid bodies characterized by non-zero shear modulus like crystals but lack ordered structures. The disordered structures of glasses can be captured by a pair correlation function, $g(r)$ or a structure factor, $S(q)$ in Fourier space. Typical $g(r)$ for glass forming liquids and crystals are shown in Fig. 1.1. In crystals, $g(r)$ displays long-range translational order persisting beyond a few nearest neighbors whereas $g(r)$ for liquids or glasses is short-ranged and decays within the first or second nearest neighbors (Fig. 1.1). Since $g(r)$ for glasses is short-ranged
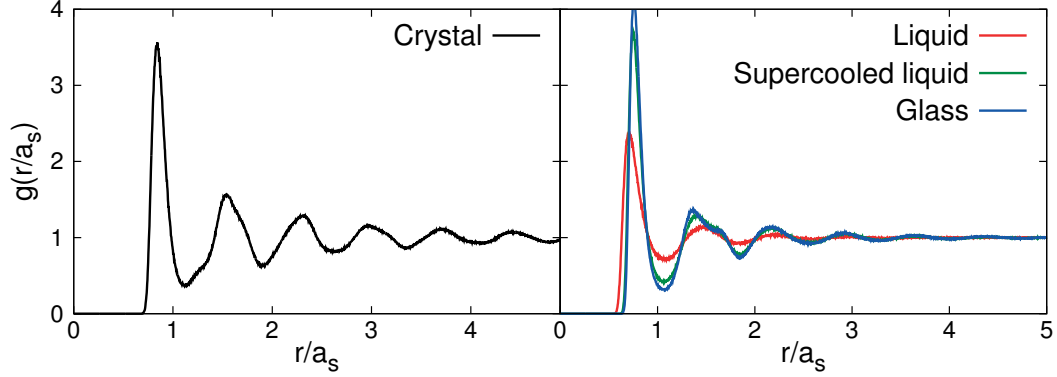
Figure 1.1: Typical pair correlation functions, $g(r)$, of a crystal (left) versus a liquid, a supercooled liquid and a glass (right). There is no significant difference in $g(r)$ between supercooled liquid and glass whereas $g(r)$ displays characteristic long correlation in crystal.

or, at least exhibits intermediate range order, it is hard to distinguish glasses from liquids only based on $g(r)$. Therefore, the static pair function is not helpful to determine whether the system is in liquid or glass phases.

More useful parameters are dynamic quantities such as time-dependent intermediate scattering function, $F(\vec{q}, t)$, which is

$$F(\vec{q}, t) = \frac{1}{N} \langle \rho_{\vec{q}}(t) \, \rho_{-\vec{q}}(0) \rangle \tag{1.1}$$

with $\rho_{\vec{k}}(t) = \sum_{i=1}^{N} \exp\left[-i\vec{k} \cdot \vec{r_i}(t)\right]$ where $\vec{r_i}(t)$ is the position vector of ith particle at time t and N is the number of particles. Because it contains all the information about the structural relaxation of liquids, $F(\vec{q}, t)$ is often used as a measure of the dynamics of glass-forming systems.

One of the most interesting features of glass-forming liquids is that the dynamic quantities such as the viscosity or the the structural relaxation time, τ_α, rapidly increase upon cooling or compressing, as in a hard sphere system. Importantly, a number of experimental and computational studies have shown that τ_α diverges following Vogel-Fulcher-Tamman law (VFT), which reads

$$\tau_\alpha = \tau_0 \exp\left[\frac{DT_K}{T - T_K}\right] \tag{1.2}$$

where τ_0 is a microscopic relaxation time, T_K is a critical temperature, and D is a fragility index measuring the temperature dependency of the relaxation time .

It should be emphasized that T_K is not the same as the laboratory glass-transition-temperature, T_g, which is the temperature where τ_α exceeds experimentally measurable timescales, but approximately equal to Kauzmann temperature, T_K ($< T_g$), below which the entropy of liquids becomes less than that of crystals. At $T = T_K^+$, the relaxation time or the viscosity "truly" diverges so that an ideal glass transition takes place. However, $T_K \approx T_K$ is not experimentally attainable and can only be estimated by extrapolation of heat capacity or other thermodynamic variables.

The fragile index, D, is another important value quantifying how a glass is robust against temperature fluctuations. When the glass has a small D, it is called a fragile glass whereas when the glass has a large D, it is called a strong one.

Another empirical function suggested by Bässler [4],

$$\tau_\alpha = \tau_0 \exp\left[A\left(\frac{T^*}{T}\right)^2\right] \tag{1.3}$$
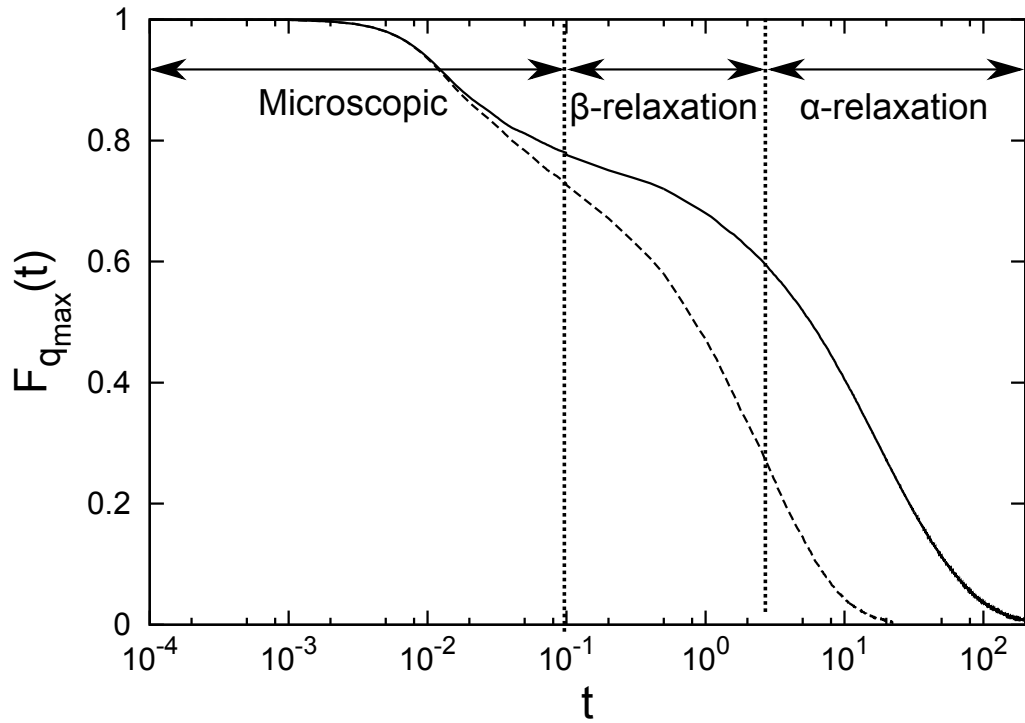
Figure 1.2: A typical plot of dynamic scattering function, $F_q(t)$, to illustrate the relaxation of supercooled liquids and glasses in different time domains. Three characteristic time domains are indicated by arrows. For details, see main text.

, where T^* is an onset temperature from which the dynamics of a liquid becomes sluggish, A is an index corresponding to a fragility index, D, and, τ_0 is a microscopic time constant, also provides reasonable fits of τ_α. In contrast to VFT, however, this function predicts the divergence only as $T \to 0$.

1.1.2   Random First Order Transition Theory (RFOT)

The divergence of the relaxation time described by VFT law can be understood using Random First Order Transition (RFOT) theory, which was introduced by Kirkpatrick, Thirumalai, and Wolynes [11–13]. To explain such a divergence, RFOT utilizes free energy landscape arguments. In typical phase transitions, we may compute a free energy as a function of order parameters to find global minimum that corresponds to a true thermodynamic state. However, this approach is not useful in glasses because glasses have numerous distinct amorphous states and the free energy should be calculated by including contributions from an exponentially large number of such configurations. Therefore, not only the dominant free energy but also the complexity, $s_c(T)$, which is defined by

$$s_c(f, T) = N^{-1} \ln \mathscr{N}(f, T) \tag{1.4}$$

where T is the temperature, N is the system size, and $\mathscr{N}(f, T)$ is the number of local minima in the free energy landscape as a function of the free energy density, f, and T, significantly contributes to free energy of the system.

In the RFOT scenario, when T is higher than a dynamic transition temperature, T_A, the free energy landscape has a single minimum that corresponds to
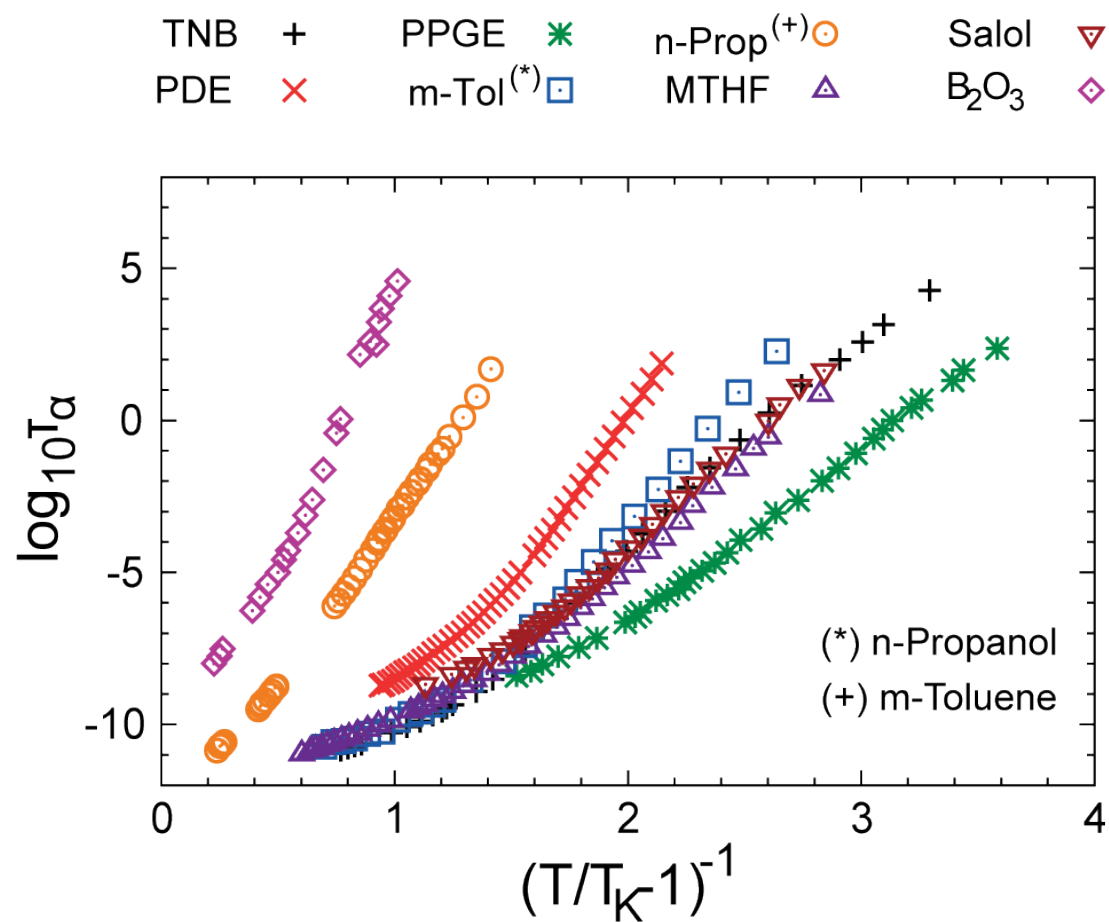
Figure 1.3: Experimentally measured α-relaxation times in various materials. T_K for each material is taken from a fit of τ_α to VFT law in $T < T_A$ where T_A is a dynamic transition point reported in literature (TNB [5], PPGE [6], nProp, MTHF and Salol [7], PDE [8], and m-Tol [9],B_2O_3 [10]). The plot displays VFT-like divergence as $T \to T_K$.

homogeneous liquid states. The system is ergodic in experimentally measurable timescales. At $T < T_A$, the free energy barriers rapidly increase upon cooling, and as a result the free energy space is fragmented into many subspaces which are not mutually accessible. Hence, the system is no longer ergodic and a long time average of thermodynamic variables estimated from a single trajectory deviates from its thermodynamic ensemble average. However, on time scale for exceeding the observation times, the free energy barriers can be overcome by thermally activated transports driven by entropic driving force so that the system is relaxed and the ergodicity is restored. As T is decreased below T_A, finally, the relaxation time diverges at $T = T_K^{(+)}$, and an ideal glass transition occurs.

Scaling relation: The scaling relation of correlation lengths in the vicinity of $T = T_K$ are predicted by RFOT based on an entropic droplet picture, which will be explained in following paragraphs, and a scaling hypothesis [11]. Suppose that free energy space consists of multiple disjoint states denoted by s and the free energy of each state is F_s. Then, a canonical free energy, F_c, is given by

$$F_c = -\frac{1}{\beta} \ln \left[\sum_s \exp\left(-\beta F_s\right) \right] \tag{1.5}$$

where $\beta = (k_B T)^{-1}$, N is the number of particles. Considering the free energy per particle, $f = F/N$, and the relation $F = E - TS$, F_s is written as

$$F_s = N \left[f - \beta^{-1} s_c\left(f, T\right) \right], \tag{1.6}$$

where $s_c\left(f, T\right)$ is a complexity per particle, which is the anologue of an entropy per particle, $s = S/N$. Substituting Eq. 1.6 into Eq. 1.5 and reformulating Eq. 1.6 in

7

f-space,

$$F_c = -\frac{1}{\beta} \ln N \int df \exp\left[N\left\{s_c\left(f, T\right) - \beta f\right\}\right]. \tag{1.7}$$

With a canonical partition function, $Z_c = \exp\left(-\beta F_c\right)$, and the probability of the system being in s-state, $P_s = Z_c^{-1} \exp\left[-\beta F_s\right]$, a component-averaged free energy, $\tilde{F}$, is

$$\tilde{F} = \sum_s P_s F_s = \frac{N}{Z_c} \int df\, f \exp\left[N\left\{s_c\left(f, T\right) - \beta f\right\}\right] \tag{1.8}$$

In the thermodynamic limit, using saddle point approximation $\int dx \exp[Ng(x)] \approx \exp[Ng(x')]$ with $\left.\frac{\partial g(x)}{\partial x}\right|_{x=x'} = 0$, the canonical free energy, F_c is simplified as

$$F_c = \tilde{F} - Nk_B T s_c\left(f', T\right) \tag{1.9}$$

with $\beta = \left.\frac{\partial s_c(f,T)}{\partial f}\right|_{f=f'}$. Then, considering a general form of a free energy, $F = E - TS$, we may define the state entropy, $S_s\left(T\right)$ as

$$S_s\left(T\right) = Nk_B s_c\left(f', T\right). \tag{1.10}$$

One of main assumptions of RFOT is that the activated transport restoring ergodicities of supercooled liquids is driven by the gradient of the state entropy S_s. Letting s_s be the state entropy per unit volume, an entropic force driven by the free energy gradient is $Ts_s L^d$ in d-dimensional space. On the other hand, the free energy cost for the formation of glassy droplet is proportional to the free energy surface area $\approx \sigma L^{d-1}$ with the assumption that the surface tension, σ, is independent of the size of the droplet. Since the typical size of glassy cluster, $L^* = \xi$, is determined by the balance between driving force and free energy cost, ξ reads

$$\xi \sim \frac{\sigma}{Ts_s}. \tag{1.11}$$

The free energy barriers between two states, ΔF^*, are

$$\Delta F^* \sim \sigma \xi^{d-1} \sim \sigma \left(\frac{\sigma}{Ts_s}\right)^{d-1}. \tag{1.12}$$

Suppose that near the critical temperature T_K the correlation length, ξ, diverges as $\xi \sim t^{-\nu}$ with a correlation length exponent, ν, and $t = (T - T_K)/T_K$. Because the free energy barrier is similar to the entropic driving force, near $T = T_K$, ΔF^* scales as

$$\Delta F^* \sim Ts_s L^d \sim Ts_s \xi^d \sim t\xi^d \sim t^{1-\nu d} \tag{1.13}$$

in d-dimensional space when s_s linearly vanishes at $T = T_K$. The exponent, ν, can be determined by the discontinuity of the second moment of the density fluctuation, q, called the Edwards-Anderson order parameter and finite-size-scaling argument.

The Edwards-Anderson order parameter, q, is defined by

$$q \equiv \overline{[\delta n(\vec{x})]^2} = \frac{1}{L^d} \int d\vec{x} \, [\delta n(\vec{x})]^2 \tag{1.14}$$

where d is the dimensionality of the system, $\delta n(\vec{x})$ is the density fluctuation at the position $\vec{x}$ from liquid density, n_l, ie, $\delta n(\vec{x}) = n(\vec{x}) - n_l$. Note that $\int \delta n(\vec{x}) \, d\vec{x} = \int [n(\vec{x}) - n_l] \, d\vec{x} = n_l - n_l = 0$. If we consider $h = \mu(T, p) - \mu(T_K, p_K)$, where $\mu(T, p)$ is a chemical potential, the free energy density for given h and the size of the system, L, denoted by $f(h, L)$, is given by

$$f(h, L) = L^{-d} \mu(T, p) \int n(\vec{x}) \, d\vec{x} = [h + \mu(T_K, p_K)] \int n(\vec{x}) \, d\vec{x}. \tag{1.15}$$

Suppose that q is discontinuous at $T = T_K$ and the free energy density behaves as

$$f(h, L) \sim L^{-\varsigma} Z\left(L/\tilde{\xi}\right) \tag{1.16}$$

where $\tilde{\xi}$ is the correlation length in finite size system. If we consider an asymptotic form $\xi \sim h^{-\nu}$, we can rewrite Eq. 1.16 in terms of L as

$$L^{-\zeta} Z \left(L/\tilde{\xi} \right) \approx L^{-\zeta} Z \left(h^{\nu} L \right) \equiv L^{-\zeta} Y \left(h L^{\theta} \right) \tag{1.17}$$

with $\theta = -1/\nu$ [14]. If we take a derivative of $f(h, L)$ with respect to h, then we may obtain

$$\frac{\partial f}{\partial h} = L^{-d} \int n\left(\vec{x}\right) d\vec{x}. \tag{1.18}$$

Using the above equation and $\int \delta n\left(x\right) d\vec{x} = 0$,

$$\left(\frac{\partial f}{\partial h} \right)^2 = L^{-2d} \left[\int n\left(\vec{x}\right) d\vec{x} \right]^2 = L^{-2d} \int n\left(\vec{x}\right) d\vec{x} \int n\left(\vec{y}\right) d\vec{y} \tag{1.19}$$

$$= L^{-2d} \int \left\{ \delta n\left(\vec{x}\right) + n_l \right\} \left\{ \delta n\left(\vec{y}\right) + n_l \right\} d\vec{x} d\vec{y} \tag{1.20}$$

$$= L^{-2d} \iint \left\{ \delta n\left(\vec{x}\right) \delta n\left(\vec{y}\right) + n_l \delta n\left(\vec{x}\right) + n_l \delta n\left(\vec{y}\right) + n_l^2 \right\} d\vec{x} d\vec{y} \tag{1.21}$$

$$= L^{-2d} \left[\iint \left\{ \delta n\left(\vec{x}\right) \delta n\left(\vec{y}\right) \right\} d\vec{x} d\vec{y} + \iint \left\{ n_l \delta n\left(\vec{x}\right) + n_l \delta n\left(\vec{y}\right) \right\} d\vec{x} d\vec{y} \right. \tag{1.22}$$

$$\left. + \iint n_l^2 d\vec{x} d\vec{y} \right] \tag{1.23}$$

$$\sim L^{-d} \int \left[\delta n\left(\vec{x}\right) \right]^2 d\vec{x} \sim L^{-d} q. \tag{1.24}$$

On the other hand, using Eq. 1.16,

$$\left(\frac{\partial f}{\partial h} \right)^2 \sim L^{-d} q \sim L^{-2\zeta + 2\theta} \left[Y' \left(h L^{\theta} \right) \right]^2. \tag{1.25}$$

Because q is discontinuous at T_K, θ and ζ must hold

$$2\theta - 2\zeta = -d. \tag{1.26}$$

Also, considering the assumption that $\chi(h, L) \equiv \frac{\partial^2 f}{\partial h^2}$ is discontinuous so that

$$\frac{\partial^2 f}{\partial h^2} \sim L^{-\zeta + 2\theta} Y'' \left(h L^{\theta} \right) \tag{1.27}$$

10

one may obtain the relation,

$$2\theta - \zeta = 0. \tag{1.28}$$

Combining Eq. 1.26 and Eq. 1.28, we may get

$$\theta = \frac{d}{2} \quad , \quad \zeta = d. \tag{1.29}$$

Therefore, the correlation length, ξ, scales as

$$\xi \sim h^{-\nu} \sim h^{-\frac{1}{\theta}} \sim h^{-\frac{2}{d}}. \tag{1.30}$$

, and because when the pressure is fixed $h \sim T - T_K$, we may obtain

$$\xi \sim t^{-\frac{2}{d}}. \tag{1.31}$$

, and, thus,

$$\nu = \frac{2}{d}. \tag{1.32}$$

Putting these results into Eq. 1.13, the free energy barrier is

$$\Delta F^* \sim t^{1-\nu d} \sim t^{-1}. \tag{1.33}$$

Assuming that the free energy barrier is overcome by diffusion, from Kramers results [15], the relaxation time, τ, is

$$\ln \tau = D\Delta F^* + \ln \tau_0. \tag{1.34}$$

$$\tau = \tau_0 \exp\left[D\Delta F^*\right] = \tau_0 \exp\left[\frac{DT}{T - T_K}\right], \tag{1.35}$$

ie, VFT equation.

1.1.3   Mode Coupling Theory (MCT)

MCT starts with a following equation involved with a dynamic scattering function, $F(q,t)$, at time t and for a wave vector $\vec{q}$,

$$\frac{d^2 F(\vec{q},t)}{dt^2} + \frac{q^2 k_B T}{mS(\vec{q})} F(\vec{q},t) + \int_0^t d\tau M(\vec{q},\tau) \frac{d}{dt} F(\vec{q},t-\tau) = 0, \qquad (1.36)$$

where $S(\vec{q}) = F(\vec{q},0)$ is the static structure factor, $M(\vec{q},\tau)$ is the memory kernel for a given particle mass m. Although the derivation of above MCT equation is our interesting topic, I will not discuss the details because it is beyond the scope of my dissertation. The detailed derivation of the MCT equation is explained in ref [16] and [17]. Solving Eq. 1.36 for a given $S(\vec{q})$ depends on a few essential approximations for $M(\vec{q},\tau)$. The basic idea of MCT is that $M(\vec{q},\tau)$ is dominated by slow modes. By the projection of $M(\vec{q},t)$ onto the dominant slow modes, we can derive the following equation for the kernel,

$$M(\vec{q},t) = \frac{\rho k_B T}{16\pi^3 m} \int d\vec{q}' \left| \vec{V}_{\vec{q}-\vec{q}',\vec{q}'} \right|^2 F(\vec{q}',t) F(|\vec{q}'-\vec{q}|,t) \qquad (1.37)$$

with

$$\vec{V}_{\vec{q}-\vec{q}',\vec{q}'} \equiv [(\hat{q} \cdot \hat{q}')c(q') + \hat{q} \cdot (\vec{q}-\vec{q}')c(|\vec{q}-\vec{q}'|)]. \qquad (1.38)$$

Using recursive relations Eq. 1.36 and 1.37, $F(\vec{q},t)$ can be numerically calculated.

Scaling relations and exponents: The solution of MCT equation reveals the detailed structure of $F(\vec{q},t)$ in time domain (Fig. 1.2). First, the short time relaxation of the order of τ_0 where all particles are transported by microscopic dynamics takes a place, and, then, $F(\vec{q},t)$ acquires a plateau related to caging by surrounding

12

neighbors. This relaxation regime is called microscopic or fast relaxation regime. In the fast relaxation regime, $F(\vec{q}, t)$ behaves as,

$$F(\vec{q}, t) = f_{\vec{q}} + \frac{h(\vec{q})}{t^a}. \tag{1.39}$$

Importantly, the exponent a is the solution of following equation,

$$\frac{\Gamma(1-a)^2}{\Gamma(1-2a)} = \lambda \tag{1.40}$$

where Γ is Gamma function and λ is a number independent of order parameters. Beyond the plateau, the system starts to relax on the order of the relaxation time, τ_β. This regime is called β-relaxation regime. In β-relaxation regime, $F(\vec{q}, t)$ follows

$$F(\vec{q}, t) \approx f_{\vec{q}} + \sqrt{\epsilon} h(\vec{q}) g\left(\frac{t}{\tau_\beta}\right), \quad \begin{cases} g(x) \sim x^{-a} & \text{if } x \ll 1 \\ \\ g(x) \sim x^b & \text{if } x \gg 1 \end{cases} \tag{1.41}$$

where $\epsilon = (T - T_A)/T_A$ and b is another MCT parameter that satisfies

$$\frac{\Gamma(1+b)^2}{\Gamma(1+2b)} = \lambda. \tag{1.42}$$

1.1.4 Dynamic heterogeneity and four-point susceptibility

Several recent computational and experimental studies reveal that the onset of LGT is manifested in the so-called "dynamic heterogeneity" [18–21]. In order to clarify the meaning of "dynamic heterogeneity", let us consider the velocities of molecules in liquids. In normal liquids, which is at the temperature much higher than T_A or T_{MCT}, the velocities of molecules are distributed following well-defined Gaussian distribution in which an average is not very far from a typical value. Hence, the average velocity can be regarded as a representative value describing

the dynamics of the system. On the other hand, this relation does not hold in supercooled liquids. In other words, the distribution no longer fits to Gaussian distribution and the average velocity of the molecules devaites from the typical value [22, 23]. Therefore, at least, for deeply supercooled liquids, the dynamics cannot be described by a few thermodynamic average values that were sufficient to determine the thermodynamic status of the whole system in normal liquids, and, thus, the fluctuations and the distributions of dynamic variables should be taken into account for the accurate calculations of thermodynamic quantities.

More systematically, the dynamic heterogeneity is quantified by four-point susceptibility, χ_4, defined by the spatial integral of four-point correlation, $G_4\left(\vec{s},t\right)$. In details, for any dynamic observable, $A\left(\vec{r},t\right)$, $G_4\left(\vec{s},t\right)$ and $\chi_4\left(t\right)$ read

$$G_4\left(\vec{s},t\right) = \int d\vec{r}\left\langle A\left(\vec{r}+\vec{s},t\right) A\left(\vec{r},t\right) A\left(\vec{r}+\vec{s},t_0\right) A\left(\vec{r},t_0\right)\right\rangle$$
$$-\left\langle A\left(\vec{r},t\right) A\left(\vec{r},t_0\right)\right\rangle^2 \tag{1.43}$$

$$\chi_4\left(t\right) = \int d\vec{s}\, G_4\left(\vec{s},t\right) \tag{1.44}$$

where $\left\langle\cdots\right\rangle$ is an ensemble average. In various glass-forming liquids and model systmes, it has been reported that $\chi_4\left(t\right)$ has a maximum at the time around an order of τ_α and the peak value diverges near a dynamic transition temperature, T_A [21, 24–26]. Hence, it is believed that the dynamic heterogeneity plays a key role in the divergence of relaxation time near T_A.

1.2 Unresolved problems in LGT

With these several-decades-long developments of theoretical concepts and experimental techniques, however, interesting fundamental problems remain unresolved. For instance, the existence of ideal glass transitions is still debated because the diverging static length scale has not been found yet. Although the recently developed point-to-set length scale is considered a strong candidate for diverging static length scale, the fact that experimentally measured critical length scale is only a few interparticle distance makes it difficult to prove or disprove the existence of such a diverging static length scale. Indeed, recent theoretical and computational studies such as random-pinning are focusing on this problem.

Also, it is still not clear whether the mechanism responsible for LGT is universal for all glass-forming systems or not. Even if we may conclude that the liquid-glass transition is a true thermodynamic phase transition at $T = T_K$ for a certain glass-forming liquid, it does not guarantee that the result may apply to all other glass-forming systems. Various model systems for glass forming liquid such as the 8:2 mixture of differently-sized Lennard-Jones (LJ) particles, so called Kob-Anderson mixture, the binary mixture of small and large hard spheres, the mixture of soft spheres, and poly-disperse LJ mixture have been used in computational studies to test theories but there is no concrete conclusion about the universality of LGT over various models. Furthermore, the dependency of thermodynamics of LGT on ensemble (NVE or NVT) and microscopic dynamics (Newtonian or Brownian dynamics) is another interesting question that is still in controversy for many theorists and

experimentalists.

With these lights, following chapters, I examine the validity of MCT and RFOT for highly charged colloidal suspension that has been identified as a glass forming system about twenty years ago but that has not been gained much research attention for many years.

Chapter 2: Manifestation of RFOT in colloidal suspension

In this chapter, I will discuss about suspensions consisting of highly charged micrometer-sized polystyrene spheres (polyballs) that are frozen into glasses (so-called Wigner glasses) at sufficiently high volume fractions. Despite the ease of tracking the positions of individual particles, successive experiments and numerical simulations have been rarely studied since 1990s and, thus, many important theoretical findings discovered in a recent decade such as dynamic heterogeneity as well as RFOT have not been discussed for this system. With these considerations, in this chapter, I will present the simulation results of a colloidal suspension to manifest some predictions of RFOT theory and will propose the origin of dynamic heterogenity that may apply to other glass-forming systems. The results and discussions presented in this chapter are published in ref [27].

2.1   Literature review

In pioneering work by Lindsay and Chaikin [28], the system consisting of highly charged colloidal particles suspended in water was studied in the context of a "Wigner crystal" or a "Wigner glass". They measured the elastic shear modulus of polydisperse polystyrene spheres from a mechanical resonance technique. The

apparatus was designed to detect standing shear modes, which correspond to the peak frequencies in the amplitude of the bobbin oscilations driven by an external pair of Helmholtz coils.

In the experiment, the mixture of small and large polyballs, which have the average radii of 545Åand 1100Å, respectively, was suspended in water. Electrostatic charges of polyballs were determined by the shear modulus analysis of the monodisperse suspension assuming Derjaguin-Landau-Verwey-Overbeek (DLVO) potential, which is

$$V_{ij}\left(r_{ij}\right) = \frac{e^2 Z_i Z_j}{\epsilon} \left(\frac{\exp\left[qa_i\right]}{1+qa_i}\right) \left(\frac{\exp\left[qa_j\right]}{1+qa_j}\right) \frac{\exp\left[-qr_{ij}\right]}{r} \tag{2.1}$$

where $Z_i e$ is the charge of the macroparticle i, q^2, the square of the inverse Debye screening length is $q^2 = \frac{4\pi e^2}{\epsilon k_B T}\left(Z\rho + \sum Z_k \rho_k\right)$, ρ_k is the number density of the kth species, Z is the valence of any added electrolyte, ρ is the corresponding number density, and, ϵ is the dielectric constant of water. The estimated charges of small and large polyballs were $300e$ and $600e$, respectively, where e is the charge of an electron. The mixing ratio of two species was controlled with the fixed total number density of $1.4 \times 10^{13} \mathrm{cm}^{-3}$. This number density approximately corresponds to the volume fraction, $\phi = 0.06$ for 1:1 mixing ratio.

They observed non-zero shear moduli with little Bragg scattering for the binary mixutre of small and large particles, which indicates that it has a finite rigidity but lacks an ordered structure. Hence, this observation suggests that the mixture is frozen into a homogeneous glass rather than a seperated crystalline structure at the volume fraction of 0.06.

The formation of a glass in the charged colloidal suspension was computationally confirmed by R.O. Rosenberg, D. Thirumalai, and R. D. Mountain [29, 30]. They varied the volume fraction of polyspheres and found that the binary mixture of polyspheres is frozen at $\phi = 0.1$ into a glassy state. The existence of the glassy state in charged colloidal suspensions has been constantly confirmed by other numerical studies in wide range of ϕ. With these lights, I performed Brownian dynamics simulations of charged colloidal suspensions to test some RFOT and MCT predictions and to discuss the dynamic heterogeneity of Wigner glasses.

2.2 Simulation details

DLVO potential   A binary mixture of charged colloidal suspensions consisting of N_1 colloidal particles with radius a_1 and N_2 particles with radius a_2 was simulated. The interaction potential between the colloidal particles is modeled by DLVO potential [29, 31–34]. Since DLVO potential is not as long ranged as the Coulomb potential, I found that it is unnecessary to use Ewald summation. I neglected, without loss of accuracy, interactions beyond a cut-off distance r_c determined by $V_{ij}(r_c) = 0.001 k_B T$, which is only 0.001% of the average energy per particle at the volume fractions simulated here. The parameters used in the simulations, listed in Table 2.1, correspond to the experimental system [28]. The colloidal system is specified by ρ and temperature T, which is fixed at 298K. I use the volume fraction, $\phi = \frac{4\pi}{3V}(N_1 a_1^3 + N_2 a_2^3)$ as a measure of ρ. In most cases I measure distances in units of $a_s = \rho^{\frac{1}{3}}$.

	N_k	Z_k	a_k	m_k	D_{k0}
k=1	5000	300	545Å	4.3×10^8 amu	$4.53\mu\mathrm{m}^2/\mathrm{s}$
k=2	5000	600	1100Å	34.4×10^8 amu	$2.24\mu\mathrm{m}^2/\mathrm{s}$

Table 2.1: Values of the number of particles (N_k), electrostatic charge in units of e (Z_k), radius (a_k), mass (m_k) and diffusion coefficient (D_{k0}) used in the simulations are presented. Here k refers to particle type. The values of D_{k0} are computed using the Stokes-Einstein formula. All parameters are chosen to simulate the experimental system of Lindsay and Chaikin [28].

Brownian dynamics   I performed Brownian dynamics simulations by integrating the following equations of motion,

$$\frac{\mathrm{d}\vec{r}_i(t)}{\mathrm{d}t} = -\nabla_{\vec{r}_i} U(\vec{r}_1, \cdots, \vec{r}_N) \frac{D_i}{k_B T} + \sqrt{2D_i}\vec{R}_i(t) \tag{2.2}$$

where $\vec{r}_i(t)$ is the position of ith particle, $U(\vec{r}_1, \cdots, \vec{r}_N)$ is $\sum_{i \neq j} V_{ij}(r_{ij})$, D_i is the diffusion coefficient of the ith particle, $\vec{R}_i(t)$ is the random noise satisfying $\left\langle \vec{R}_i(t) \cdot \vec{R}_j(t') \right\rangle = 6D_i\delta_{ij}\delta(t-t')$ with δ_{ij} being the Kronecker delta and $\delta(t-t')$ is the Dirac delta function.

The integration step, δt, must be smaller than the time, a_s^2/D_1, where the characteristic distance between particles is $a_s = \rho^{-\frac{1}{3}}$ where $\rho = \frac{(N_1+N_2)}{V}$ with V being ρ-dependent size of the simulation box. The neglect of inertial effects in Eq. (2.2) is justified if δt is larger than the characteristic decay time, $m_1 D_1/k_B T$ of the

20

velocity correlation function. The values of D_{k0} ($k = 1$ or 2) are obtained using $D_{k0} = \frac{k_B T}{6\pi\eta a_k}$ where $\eta = 0.89\,\mathrm{mPa}\cdot\mathrm{s}$ for water. With these values the range for δt turns out to be from 10 ns to 1 ms. I chose $7\mu s$ for δt as a compromise between accuracy and computational costs. The use of real times is only for estimates, and need not correspond to experimental times.

I equilibrated the system of 10^4 particles by placing them initially at the sites of a body-centered cubic lattice in a periodic simulation box. The size of the box was adjusted to obtain the desired ϕ, and it ranged from (2,500 - 5,000) nm ($\approx (46 - 92)a_1$) depending on ϕ. To achieve thermal equilibration, I carried out slow-quenching by controlling the concentration of electrolytes following the method used by Sanyal and Sood [32]. The ratio of the concentration of electrolytes to colloids $\bar{\rho} = \rho/Z^{-1}\sum_k Z_k\rho_k$ was initially set to 5, and the equations of motion were integrated for $2 \times 10^5\delta t$ in the liquid phase (low ϕ), and $10^6\delta t$ in a highly jammed glassy state (high ϕ). Subsequently, I reduced $\bar{\rho}$ by half, and the simulations were further carried out with the reduced $\bar{\rho}$. This procedure was repeated until $\bar{\rho}$ reached $5/2^{10}$. After reaching the final value, $\bar{\rho}$ was set to zero. The protocol used here accelerates the equilibration times [32]. After equilibration, data were collected for 10^5 time steps. Since this time is not long enough to obtain structural relaxation dynamics for $\phi \geq 0.075$, I performed additional simulations for times ranging from $10^6\delta t$ to $4 \times 10^6\delta t$ when the system reached a high density compressed state. For example, at $\phi = 0.2$, the total simulation time was $5 \times 10^6\delta t$, which is still not long enough to accurately extract structural relaxation times. I generated 20 trajectories at each ϕ and ensemble averages, where appropriate, were performed

21

over the trajectories.

2.3 Results and discussion

2.3.1 Radial distribution functions:

The radial distribution functions, and the associated structure factors for various volume fractions are shown in Fig. 2.1. As has been established in many previous studies the static pair functions, $g_{11}(r)$, $g_{12}(r)$, and $g_{22}(r)$ do not vary significantly except for some very minor changes in the first peak. In addition, there is clear evidence for split second peak, which is often found in glass forming systems [35]. The longer (compared to systems interacting with soft sphere and Lennard-Jones potential) range and strength of the interaction leads to short range order that persists for several values of a_s even at low volume fractions. For the highly charged micron-sized particles studied here the effective hard sphere diameter is considerably larger than the bare particle size [33, 36]. Thus, although technically these can be thought of as low-density low-density systems even the lowest value of ϕ would correspond to a dense equivalent hard sphere liquid [36].

2.3.2 Mean squared displacement and diffusion coefficient

The mean-square displacement (MSD) as a function of t,

$$\langle \Delta r_\alpha^2(t) \rangle = \frac{1}{N_\alpha} \sum_{i=1}^{N_\alpha} \langle [r_i(t) - r_i(o)]^2 \rangle \tag{2.3}$$
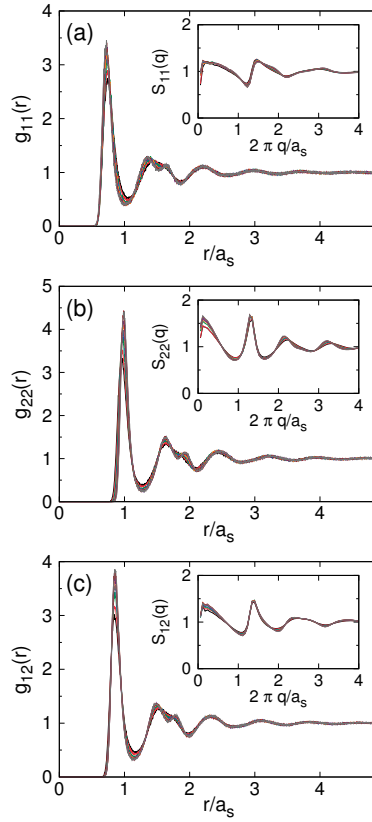
Figure 2.1: Pair correlation functions for binary charged colloidal particles. (a) Radial distribution functions, $g_{11}(r)$, between type-1 (smaller-sized) particles. The corresponding structure factors $S_{11}(q)$ are in the inset. (b) Same as (a) except these curves are for the larger-sized particles. The inset contains $S_{22}(q)$ plots. (c) Pair functions between type-1 and type-2 particles and the corresponding $S_{12}(q)$. In all panels distance is measured in units of a_s and the scattering wave vector is in unit of $\frac{2\pi}{a_s}$. Volume fraction, ϕ, presented here are 0.2, 0.175, 0.15, 0.125, 0.1, 0.075, 0.06, 0.05, 0.04, 0.03, 0.02 and 0.01 from top to bottom.

with $\alpha = 2$ (large size particles) is shown in Fig. 2.2(a). There are three discernible regimes. At short times $t \leq \frac{a_s^2}{D_{\alpha 0}}$, $\langle \Delta r_\alpha^2 \rangle$ increases linearly with t with a slope that is proportional to the bare diffusion constant, $D_{\alpha 0}$. This regime represents essentially free diffusion of a test particle. At intermediate times there is a plateau, whose duration increases as ϕ increases. In this time regime the particles are pinned by their neighbors. Finally, at much longer times the particles undergo diffusive motion, and $\langle \Delta r_\alpha^2 \rangle$ again increases linearly now with D_α being determined by collective effects arising from interaction with particles.

The values of $D_{\alpha 0}$, obtained from the slopes of the initial increase in $\langle \Delta r_\alpha^2(t) \rangle$ do not change significantly as ϕ increases, because the extent of caging is weak in this initial time regime. However, D_α, calculated from the slopes of $\langle \Delta r_\alpha^2(t) \rangle$ at long times (see Fig. 1(a)), decreases rapidly as ϕ increases (Fig. 1(b)), and approaches $\phi_A \sim 0.1$, which is the first signature of the onset of glassy behavior. The dependence of D_α for $\alpha = 1$ and 2 on ϕ are well fit using $D_\alpha \approx (\frac{\phi_A}{\phi} - 1)^{\gamma_D}$, where I have identified $T_A \sim \phi_A^{-1}$. The fits, shown in Fig. 1(b), yield $\phi_A \approx 0.10$ and $\gamma_D \approx (1.0 - 1.2)$ depending on the particle type α. Three comments about the dependence of the translational diffusion on ϕ are worth making. (1) The values of γ_D are smaller than what is typically expected based on the mode coupling theory predictions. (2) I expect, based on RFOT predictions [37, 38], that ϕ_A is the characteristic volume fraction at which there is an effective ergodic to non-ergodic transition. (3) The duration of the plateau in $\langle \Delta r_\alpha^2 \rangle$ increases rapidly as ϕ exceeds 0.10 further indicating that this represents the dynamical transition density.
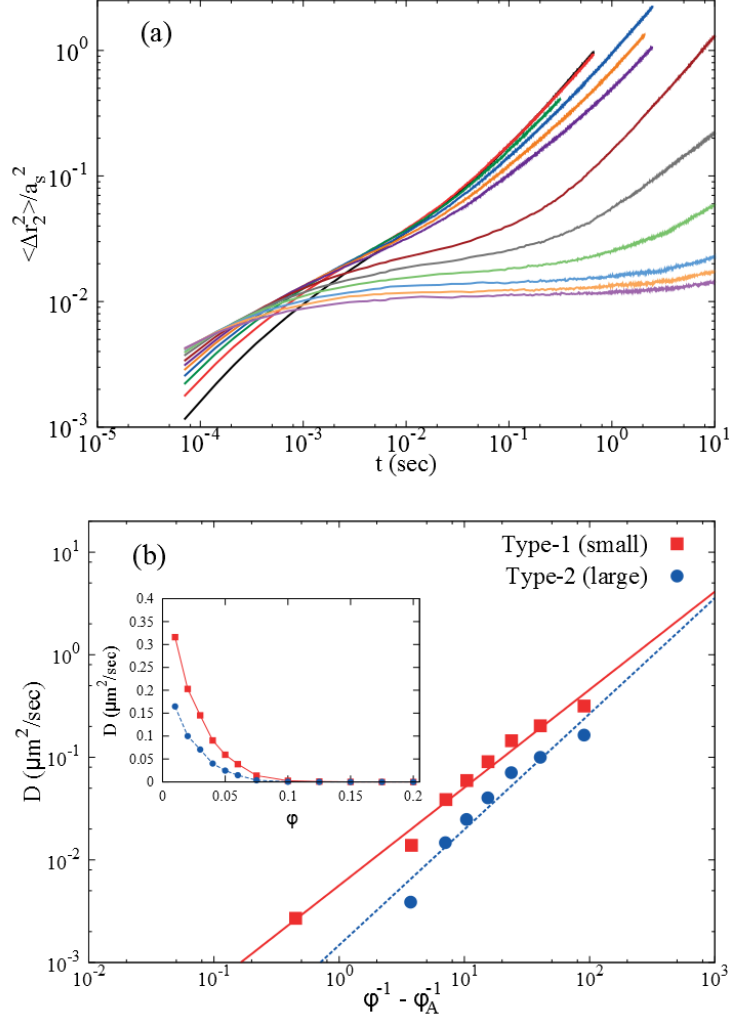
Figure 2.2: Mean-squared displacements (MSD) as a function of time, t. (a) Changes in MSD, $\langle \Delta r_2^2(t) \rangle / a_s^2$ as a function of time for large particles at ϕ values are 0.01, 0.02, 0.03, 0.04, 0.05, 0.06, 0.075, 0.1, 0.125, 0.15, 0.175 and 0.2 from top to bottom. (b) The values of the diffusion coefficients, calculated from the long time values of $\langle \Delta r_\alpha^2(t) \rangle$, as a function of ϕ are shown in the inset. Diffusion coefficients are fit to power-law $\approx \left(\phi^{-1} - \phi_A^{-1} \right)^{\gamma_D}$. The fits yield $\phi_A = 0.11$ for small particles (red, filled square) and 0.10 for type-2 particles (blue, filled circle), with $\gamma_D = 1.0$ and 1.2 for small and large particles, respectively.

25

2.3.3 ϕ-dependence of relaxation of density-density correlation function and activated transport:

The collective variable that slows down as ϕ approaches and then exceeds ϕ_A is $F_q(t)$, the density-density correlation function,

$$F_{\vec{q}}(t) = \frac{1}{N} \sum_{j=1}^{N} e^{i\vec{q}\cdot\vec{r_j}(t)} \sum_{k=1}^{N} e^{-i\vec{q}\cdot\vec{r_k}(0)} \tag{2.4}$$

where $\vec{r_i}(t)$ is the position of ith particle at time t. The isotropic scattering function $\langle F_q(t) \rangle$ is estimated by integrating the ensemble averaged $\langle F_{\vec{q}}(t) \rangle$, with $\langle \cdots \rangle$ denoting ensemble average, over space with $q = |\vec{q}|$. The plots of the time dependence of $\langle F_{\vec{q}}(t) \rangle$, for various values of ϕ in Fig. 2.3 at $q = q_{max} = \frac{2\pi}{r_s}$ (where r_s is the location of the first maximum in the total pair function calculated using both the particle types at $\phi = 0.20$), show that $\langle F_{q_{max}}(t) \rangle$ vanishes in the liquid state at long times $\phi < \phi_A$. The solid lines in Fig. 2.3 are fits of the simulation data (for times exceeding ~ 0.1s) to a stretched exponential function $\langle F_{q_{max}}(t) \rangle \approx C exp(-(\frac{t}{\tau_\alpha})^\beta)$ where the stretching exponent $\beta \approx 0.45$ is fairly independent of ϕ.

I expect that the dynamics in the vicinity of ϕ_A and above ϕ_A should be described by Mode-Coupling Theory (MCT) [39, 40], which has been applied to study relaxation near the glass phase of a restricted primitive model [41]. According to MCT, $F_{\vec{q}}$ should decay in two steps. At early times,

$$F_{\vec{q}}(t) \sim f_{\vec{q}} + A_{\vec{q}} t^{-a} \tag{2.5}$$

followed by

$$F_{\vec{q}}(t) \sim f_{\vec{q}} - B_{\vec{q}} t^b \tag{2.6}$$
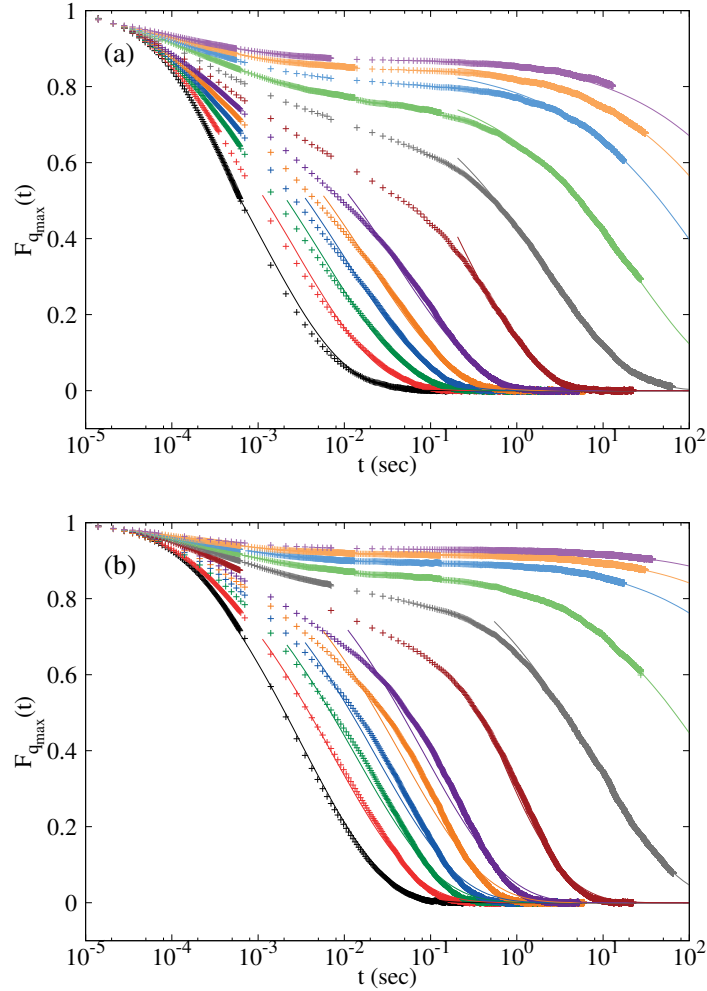
Figure 2.3: Characteristics of the density-density correlation function. (a) Scattering function $F_q(t)$ at $q = q_{max}$ for the small particles as a function of ϕ. (b) Same as (a) except these curves are for the large particles. In both (a) and (b), I fixed q_{max} at the values where the total static structure factor has a peak at $\phi = 0.2$. All the displayed $F_q(t)$ curves are fit to a stretched exponential function $C \exp\left[-(t/\tau_\alpha)^\beta\right]$ with $\beta = 0.45$ over a range of fitting. The thin solid lines are examples of fits for $t > \sim 0.1$s.

for a range of longer times. The material-dependent parameter λ satisfies

$$\lambda = \frac{\Gamma\left(1-a\right)^2}{\Gamma\left(1-2a\right)} = \frac{\Gamma\left(1+b\right)^2}{\Gamma\left(1+2b\right)} \tag{2.7}$$

The excellent fits in Fig. 2.4 with $a = 0.29$, $b = 0.47$ and $\lambda = 0.78$ shows that the MCT accurately predicts the slow dynamics in $F_{\vec{q}}$ in the vicinity of ϕ_A.

In the insets in Figs. 2.4(a) and 2.4(b) I show the dependence of τ_α obtained from the $\langle F_{\vec{q}_{max}}(t)\rangle \approx e^{-(t/\tau_\alpha)^\beta}$ fits given in Figs. 2.4(a) and 2.4(b). For both types of particles $\tau_\alpha \approx \left(\phi^{-1} - \phi_A^{-1}\right)^\gamma$ with $\gamma = 1.6$ and $\phi_A \approx 0.1$ in the range $\phi \leq \phi_A$. When ϕ exceeds about 0.15, the dynamics is so sluggish that $\langle F_{\vec{q}_{max}}(t)\rangle$ does not decay fast enough, which is an indication that there could be another characteristic volume fraction, $\phi_K > \phi_A$ at which Wigner glass undergoes an ideal glass transition. In order to estimate the value of ϕ_K, I show in the right insets in Figs. 2.4(a) and 2.4(b), the dependence of τ_α on ϕ, with the line being the Vogel-Fulcher-Tamman (VTF) fit,

$$\tau_\alpha \approx \tau_{\text{VTF}} \exp\left[\frac{D}{\left(\frac{\phi_K}{\phi} - 1\right)}\right]. \tag{2.8}$$

By fitting τ_α to the VTF equation I obtain $\tau_{VTF} = 0.01s$, the fragility index $D = 23$, $\phi_K = 0.47$, which should be taken to be approximate given the paucity of data. The VTF also provides only a semi-quantitative fit of the entire data set. Because of the extremely slow dynamics at values of ϕ far greater than ϕ_A, it is difficult to obtain numerically converged results for τ_α, which would be needed to obtain a more accurate value for ϕ_K. Nevertheless, given that $\phi_K \gg \phi_A$ I surmise that ϕ_K should be associated with an ideal glass transition density at which the relaxation time essentially diverges. The finding that ϕ_A and ϕ_K (with somewhat imprecise

estimate) exist for Wigner glass validates a key aspect of the RFOT theory.

2.3.4 Ergodicity breaking near ϕ_A:

In order to determine if ergodicity is broken at $\phi \approx \phi_A$, I calculated the energy metric, which is a general measure for assessing the necessary condition for establishing ergodic behavior in classical many body systems [42, 43]. The energy metric is calculated by trajectories using two replicas (different initial conditions) of the system at the same volume fraction. For each replica I define the time average value of the energy of the ith particle,

$$\bar{E}_\alpha^j(t) = t^{-1} \int_0^t E_\alpha^j(t')\, \mathrm{d}t' \tag{2.9}$$

where $E^j(s)$ is energy of particle j at time s, and α labels the replica. The energy metric $d_{\alpha\beta}(t)$ is,

$$d_{\alpha\beta}(t) = \sum_{k=1}^{2} N_k^{-1} \sum_{i=1}^{N_k} \left[\bar{E}^k_{\alpha;i}(t) - \bar{E}^k_{\beta;i}(t)\right]^2 \tag{2.10}$$

where N_k is the number of particles of type k, $\bar{E}_\alpha^j(t)$ and $\bar{E}_\beta^j(t)$ are the energies of particle j in replica α and β averaged over time t, respectively. If the system is ergodic on the observation time scale (τ_{obs}) then $d_{\alpha\beta}(t)$ vanishes as $t \to \tau_{obs}$. Thus, when ergodicity is established I expect that $\bar{E}^k_{\alpha;i}(\tau_{obs}) = \bar{E}^k_{\beta;i}(\tau_{obs})$ independent of α or β or i. This is the situation that pertains to the liquid phase. If ergodicity is broken, then $d_{\alpha\beta}(\tau_{obs}) \to C$ (C is a constant) suggesting that the two initial states do not mix on the time scale τ_{obs}. It is the development in time [42] of appropriate dynamical variables, rather than equal time correlation functions, that distinguishes

29
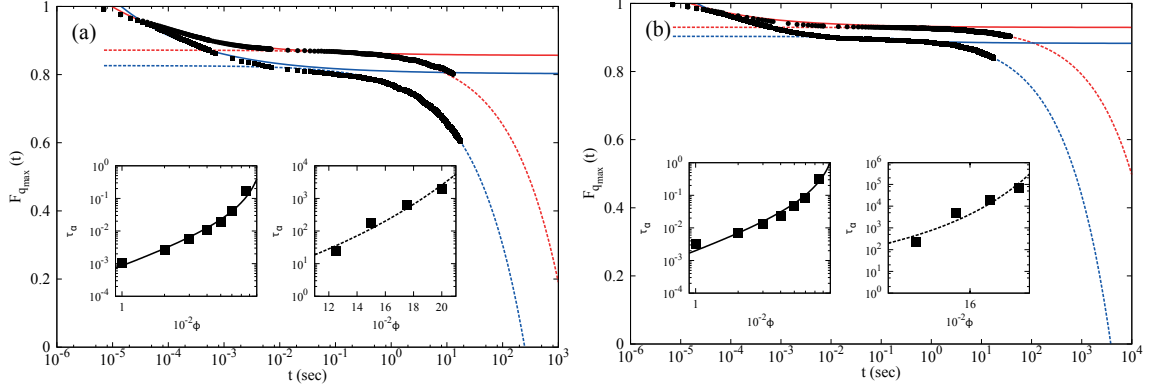
Figure 2.4: (a) Decay of $F_q(t)$ at $q = q_{max}$ for small particles. The data points in black on the top curve are for $\phi = 0.20$, and the results in the curve below are for $\phi = 0.15$. Solid red and blue lines are fits to Eq. (2.5), and the dashed lines are the fits to Eq. (2.6). (b) Same as (a) expect the results are for the large particles. The MCT parameters for both the small and large particles are $a = 0.290$, $b = 0.494$, and $\lambda = 0.780$. The relaxation times τ_α as a function of ϕ are shown in the insets in (a) and (b). In the insets on the left I show τ_α as a function of ϕ for $\phi \leq 0.1$ in a log-log plot. The solid lines are power law, $\tau_\alpha \approx (\phi^{-1} - \phi_A^{-1})^\gamma$, fits to the data with $\phi = 0.1$ and $\gamma \approx 1.56$ for both small and large particles. The right insets show the dependence of τ_α on ϕ for $\phi > 0.10$ with the dashed lines being fits to the VFT-law $\tau_0 \exp\left[\frac{D}{(\phi_K/\phi - 1)}\right]$. The value of $\phi_K \approx 0.47$.

a glass from a liquid. Scaling-type arguments show that $d_{\alpha\beta}(0)/d_{\alpha\beta}(t) \approx D_E t$ at long times where the inverse of the ergodic diffusion constant, D_E^{-1}, sets the approximate time scale in which the two configurations (α and β) mix. Thus, $N d_{\alpha\beta}(0)/d_{\alpha\beta}(t)$, which is extensive in both N and τ_{obs} in the liquid phase, remains only extensive in N in the glassy phase because $\tau_\alpha \gg \tau_{obs}$.

The reciprocal of the energy metric, $d_{\alpha\beta}(0)/d_{\alpha\beta}(t)$, (Fig. 4(a)) increases linearly with t at low densities, and saturates as ϕ increases (exceeds $\sim \phi_A$). From the linear dependence of $d_{\alpha\beta}(0)/d_{\alpha\beta}(t)$ I calculated the dependence of D_E on ϕ (Fig. 4(b)). I find that $D_E \ll 1$ decreases sharply at $\phi \approx \phi_A$, which implies that ϕ_A is the volume fraction at which the time and ensemble averages start to deviate from each other [38]. The dependence of D_E on ϕ can be fit using $D_E \approx (\phi^{-1} - \phi_A^{-1})^{\gamma_E}$ (Fig. 4(b)) with $\phi_A \approx 0.12$ and $\gamma_E \approx 1.2$. Interestingly, ϕ_A extracted from the ϕ dependence of D_E nearly coincides with the value of ϕ_A at which diffusion effectively ceases. Thus, ϕ_A can be identified with the volume fraction at which ergodicity is broken.

2.3.5 Four point dynamical correlation function:

In order to distinguish between liquid and glass-like states as ϕ approaches ϕ_A it is necessary to consider fluctuations in multi-particle correlation functions because there is no obvious symmetry breaking as the liquid becomes a glass [42]. The rationale for considering multi-particle correlation functions is that the natural order parameter that describes the onset of SGT is the two particle correlation
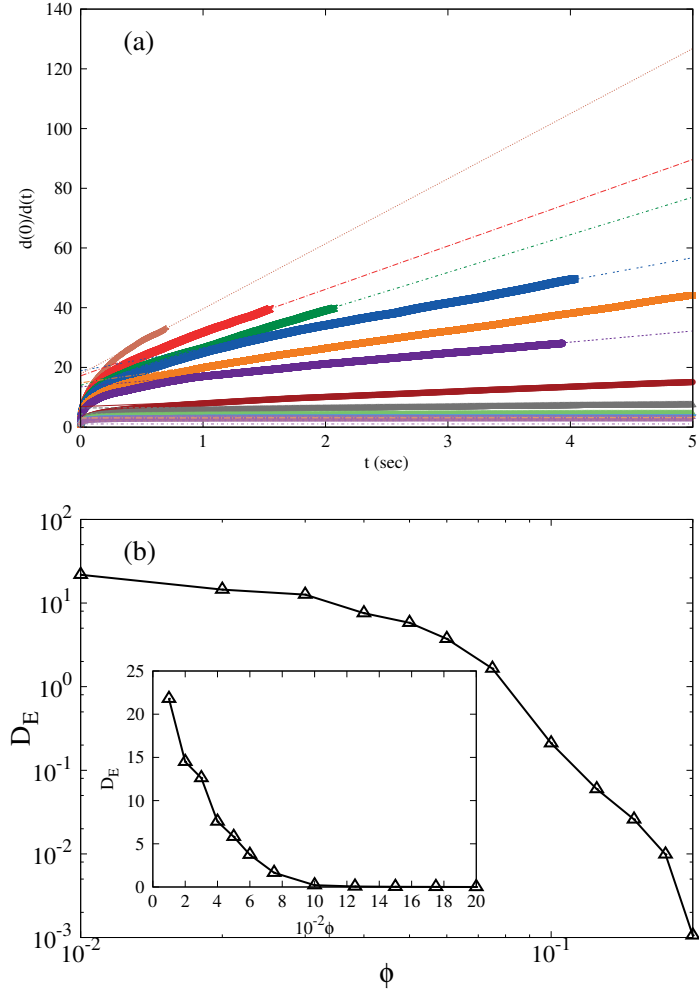
Figure 2.5: (a) Plots of the reciprocal of the energy metric, $d(0)/d(t)$, as a function of t to $D_E t$ at ϕ values are 0.2, 0.175, 0.15, 0.125, 0.1, 0.075, 0.06, 0.05, 0.04, 0.03, 0.02 and 0.01 (from top to bottom). (b) The ergodic diffusion coefficients are extracted from the theoretically predicted scaling behavior $d(0)/d(t) \sim D_E t$. Dependence of D_E on ϕ is fit using $D_E \approx (\phi^{-1} - \phi_A^{-1})^{\gamma_E}$ with $\phi_A \approx 0.10$ and $\gamma_E \approx 1.2$ (shown in log-log plot). Inset shows D_E as a function of ϕ.

function, $F_q(t)$, which decays to zero in the liquid phase, and saturates in the glassy phase at long times (Fig. 2.3). Thus, only the fluctuations in $F_q(t)$, which plays the role of generalized susceptibility, $\chi_4(q|t)$, can distinguish between the states below ϕ_A [38]. A number of studies have used $\chi_4(q|t)$ to produce evidence for growing dynamical correlation length [18, 26, 44, 45].

The four point correlation function $\chi_{4|F_q}$ is the variance in $F_q(t)$, and is given by

$$\chi_{4|F_q}(t) = \left\langle F_q(t)^2 \right\rangle - \left\langle F_q(t) \right\rangle^2 \tag{2.11}$$

I calculated $\chi_{4|F_q}(t)$ using a moving time averaging procedure in order to minimize numerical errors. The plots of $\chi_{4|F_q}(t)$, evaluated at q_{max} for various values of ϕ, (Fig. 2.6(a)) show that the amplitude of the peak in $\chi_4(t)$ increases as ϕ increases. The dependence of the time, t^*, at which $\chi_{4|F_q}(t^*)$ is a maximum is shown in the inset of Fig. 2.6(a). Although I am unable to compute $\chi_{4|F_q}(t)$ accurately for $\phi > 0.075$, the changes in t^* as ϕ changes can be fit to a power law. The details of the fit are in the caption to Fig. 2.6. It is noteworthy that ϕ_A extracted from the fit is essentially the same as that obtained by analyzing the dependence of D_E on ϕ (Fig. 2.5(b)), thus establishing that the four-point susceptibility does probe the onset of ergodic - non-ergodic transition at ϕ_A.

Although it is most natural to use fluctuations in $F_q(t)$ to determine the four-point susceptibility others have considered different variables. One of these is the total overlap function, $\Omega(\delta, t)$, defined as [46],

$$\Omega(\delta, t) = N^{-1} \sum_{i=1}^{N} \omega\left(\left| \vec{r}_i(t) - \vec{r}_i(0) \right|, \delta \right) \tag{2.12}$$

33

where $\vec{r}_i(t)$ is position of the ith particle, N is number of particles, and $\omega(x, \delta)$ is step function which is 1 when $x \leq \delta$. $\Omega(\delta, t)$ depends on δ and it is fixed at $0.3a_s$. The four-point function involving the fluctuations in $\Omega(\delta, t)$ is defined as,

$$\chi_{4|\Omega}(t) = N\left[\langle\Omega(t)^2\rangle - \langle\Omega(t)\rangle^2\right]. \tag{2.13}$$

In Fig. 2.6(b) I show the time evolution of $\chi_{4|\Omega}(t)$ for various ϕ values. Both $\chi_{4|\Omega}(t)$ and $\chi_{4|F_q}(t)$ evaluated at q_{max} are nearly identical. The dependence of t^* on ϕ calculated using $\chi_{4|\Omega}(t)$ also shows a power law dependence (Fig. 2.6(b)). The only difference is that the exponent characterizing the divergence of t^* as $\phi \to \phi_A$ is 1.20 as opposed to 1.05 obtained in Fig. 5(a). The values of ϕ_A as well as the exponents (γ_D, γ_E, and γ_χ) characterizing the dependence of the translational diffusion coefficients, ergodic diffusion coefficient, and t^* on ϕ ($< \phi_A$) are similar.

2.3.6 Dynamical heterogeneity is a consequence of violation of law of large numbers:

A tenet of statistical mechanics is that many body systems obey the law of large numbers, implying that equilibrium properties of a large subsample is on an average identical to the entire sample. In the liquid phase ($\phi < \phi_A$) the statistical properties of any subsample should coincide with that of the entire sample provided the subsample contains a large number of particles and the observation time is long enough compared to D_E^{-1} (Fig. 2.5(b)). In contrast, in the glassy phase, I expect that statistical properties (distribution of energies of individual particles for example) of even a large subsample can deviate from that of the entire sample [42].
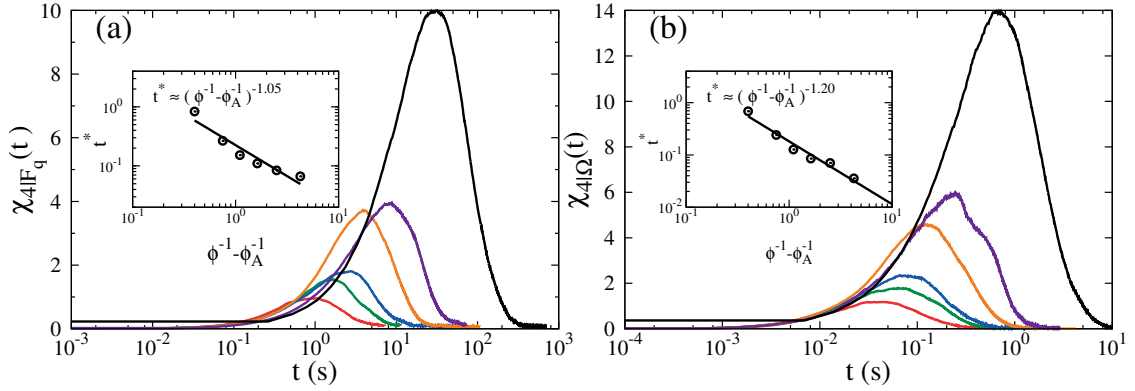
Figure 2.6: (a) Four-point susceptibility $\chi_4(t)$ function determined by fluctuations of the scattering function $F_q(t)$ for all pairs of particles. q is fixed at the first peak of total structure factor calculated irrespective of particle identity. Results for $\phi = 0.02$, 0.03, 0.04, 0.05, 0.06 and 0.075 from left to right. The position of the peak, t^*, as a function of $\phi^{-1} - \phi_A^{-1}$ is shown as open circles in the inset. The solid line represents a power-law $\left(\phi^{-1} - \phi_A^{-1}\right)^{-\gamma_\chi}$ fit with $\phi_A \approx 0.1$ and γ_χ is 1.05. (b) Evolution of the four-point function $\chi_{4|\Omega}(t)$ defined by variation of total overlap function $\Omega(\delta, t)$ (Eq. (12)) for all pairs of particles for the same ϕ values as in (a). Inset shows the dependence of the position of the peak t^* in $\chi_{4|\Omega}(t)$ (circles). The solid line is a fit to a power-law $\left(\phi^{-1} - \phi_A^{-1}\right)^{-\gamma_\chi}$ with $\phi_A \approx 0.1$ with $\gamma_\chi = 1.20$.

One would then expect that two distinct subsamples, which become equivalent in a liquid when viewed over a short period time, would remain inequivalent (or do not exchange) at volume fractions less than ϕ_A even when $\tau_{obs}D_E \gg 1$. Thus, no single subsample can characterize the distribution of observables of the entire sample in highly supercooled liquids. In other words, in the glassy phase the law of large numbers is violated, and, hence, there are ought to be subsample to subsample fluctuations. Only by examining the entire sample on time scale $\tau_{obs} \gg \tau_\alpha$ can the equivalence of time and ensemble averages be established. These arguments suggest that dynamical heterogeneity, which is one of the characteristics of glass forming systems [47, 48], is a consequence of the emergence of glassy clusters that remain inequivalent even when $t \gg \tau_{obs}$. Because of the variations in both equilibrium and relaxation properties from subsample to subsample, a glassy phase, in which equivalence between particles is lost, is inherently heterogeneous.

In order to illustrate the violation of large numbers, I first consider an approximate measure of structural entropy s_3 [49],

$$s_3 = \frac{\rho}{2} \int 4\pi r^2 \left[g\left(r\right) \ln g\left(r\right) - \left\{ g\left(r\right) - 1 \right\} \right] \mathrm{d}r \qquad (2.14)$$

where $g\left(r\right)$ is the pair-correlation function, and ρ is the number density. I define a local structural entropy measure $s_3^{(j)}$ for particle j using,

$$s_3^{(j)} = \frac{\rho}{2} \int 4\pi r^2 \left[g^{(j)}\left(r\right) \ln g^{(j)}\left(r\right) - \left\{ g^{(j)}\left(r\right) - 1 \right\} \right] \qquad (2.15)$$

where $g^{(j)}\left(r\right)$ is pair-correlation with respect to the jth particle. I calculated the
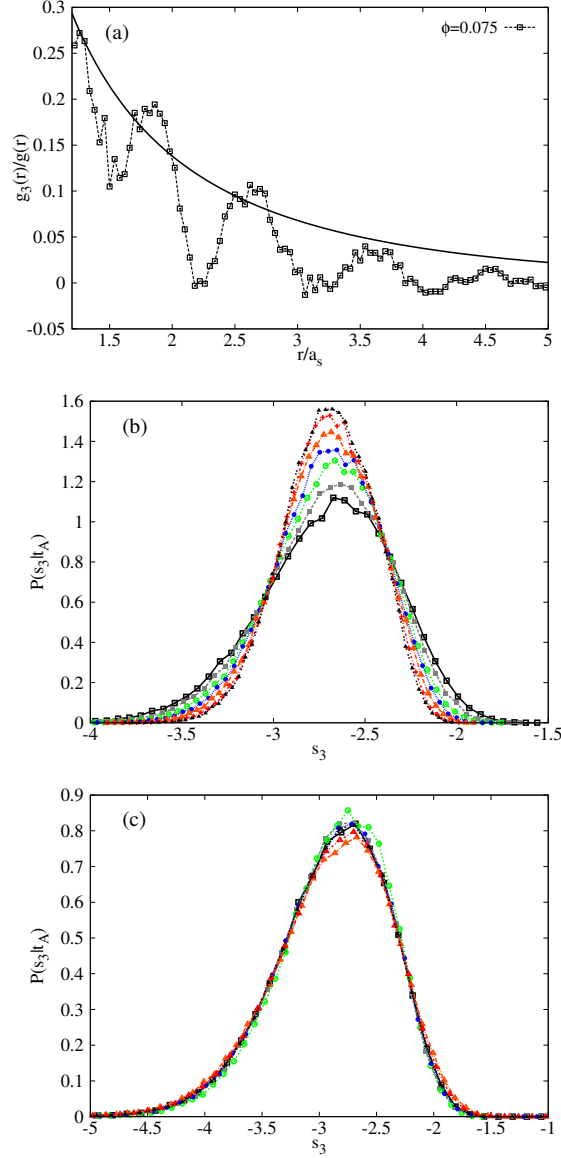
Figure 2.7: (a) $g_3(r)/g(r)$ (Eq. (16)) as a function of r for $\phi = 0.075$. The fit of the peak positions to $r^{-1}\exp(-r/\xi_s)$ yields $\xi_s \approx 3.3a_s$. (b) Distribution of time-averaged $\bar{s}_3$ (Eq. (17)) for liquid ($\phi = 0.02$) at various values of t. The time interval t_A is 12.5, 7.5, 5, 2.5, 1.25, 1 and $0.5D_E^{-1}$ from top to bottom. (c) The same graph for glass ($\phi = 0.2$) with the same time interval as in (a).

spatial correlation of s_3 as a function of distance, r, using

$$g_3(r) = \frac{\sum_{i \neq j} \delta(r - r_{ij}) \bar{s}_3^i \bar{s}_3^j - \langle \bar{s}_3 \rangle^2}{4\pi r^2 \Delta r (N-1) \rho} \tag{2.16}$$

where r_{ij} is the distance between a pair of particles, and $\langle s_3 \rangle$ is the average value of the structural entropy. A fit of $g_3(r)$ to $Cr^{-1} \exp(-r/\xi_s)$ for $\phi = 0.075$ yields $\xi_s = 3.3a_s$ (Fig. (2.7(a))), a value I use to illustrate fluctuation among subsamples.

The time evolution of the distribution of $P(\bar{s}_3|t_A)$ of the time-averaged $\bar{s}_3$ (see below) for the entire sample and a subsample of size $\xi \approx 3.3a_s$ (containing large enough particles) are used to demonstrate the violation of large numbers. The time-averaged local structural entropy associated with particle j is given by,

$$\bar{s}_3^{\ j}(t_A) = t_A^{-1} \int_0^{t_A} s_3^j(s) \, \mathrm{d}s. \tag{2.17}$$

In Fig. 2.7(b) I show the distribution, $P(\bar{s}_3|t_A)$ at different values of t_A for $\phi = 0.02$. As t_A increases $P(\bar{s}_3|t_A)$ converges and the its width narrows as expected for a system approaching equilibrium. In contrast, $P(\bar{s}_3|t_A)$ for $\phi = 0.2$ (Fig. 6(c)) is essentially frozen in time indicating that the transport of particles required for ergodicity to be reached does not occur on $t_A = 12.5D_E^{-1}$.

It is instructive to simultaneously compare the time evolutions of a large subsample and the whole sample for $\phi = 0.02$ and $\phi = 0.2$. Figs. 7(a) and 7(b) show that in the liquid phase ($\phi = 0.02$) the distributions $P(\bar{s}_3|t_A)$ are almost the same for all t_A values as is to be expected based on the law of large numbers. In contrast, at higher volume fractions ($> \phi_A$) where ergodicity is effectively broken, the $P(\bar{s}_3|t_A)$ for the subsample are substantially different from that of the entire sample, thus violating the law of large numbers (see Figs. 7(c) and 7(d)). Interestingly, there are

subsample to subsample variations in $P(\bar{s}_3|t_A)$ even with $t_A = 12.5 D_E^{-1}$ as shown in the inset in Fig. 7(d). Because different subsamples behave in a distinct manner and do not become equivalent the dynamics below ϕ_A is heterogeneous. Thus, dynamical heterogeneity is a consequence of violation of law of large numbers.

Pictorially, I can see how the frozen dynamics is manifested in Wigner glasses. In the top panel in Fig. 2.9 I show the time evolution of particles within $\xi \approx 3.3 a_s$ (see Fig. 6(a) for estimate of ξ) for $\phi = 0.02$. There are changes in the configuration, which explains how ergodicity is established by particles of a given type becoming equivalent on $t \sim D_E^{-1}$. In sharp contrast, the particles at high density ($\phi = 0.2$) are frozen. These represent low entropic droplets with local orientational order, which do not propagate across the entire sample [50, 51].

2.4 Summary

In this section, I manifested some predictions of MCT and RFOT using highly charged colloidal suspensions. The simulations results confirmed that this system forms a Wigner glass with increasing volume fractions and the relaxation time diverges following power-law for $\phi < \phi_A$ and VFT-law for $\phi > \phi_A$ where ϕ_A is a dynamic transition points. I emphasize that all dynamic quantities measured in this work, ie, the relaxation time of intermediate scattering functions, mean-squared displacements, energy metrics diverges at the same $\phi_A \approx 0.12$. $\chi_4(t)$, which quantifies the dynamic heterogeneity, is also estimated for this system. The analysis indicates that the dynamic heterogeneity seems to play a key role in diverging nature of dy-
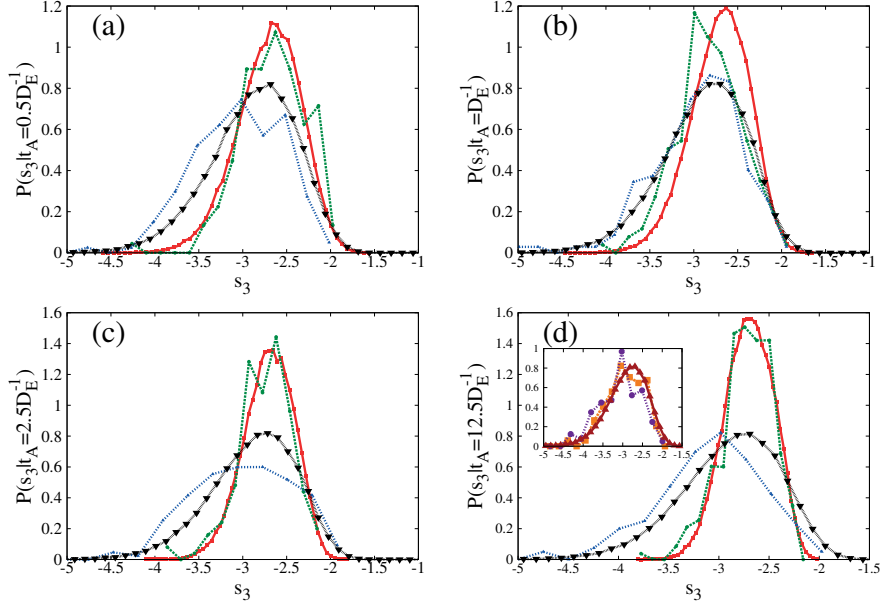
Figure 2.8: (a) The red and green curves correspond to the entire sample and a subsample with size $\xi \approx 3.3a_s$, respectively for $P\left(\bar{s}_3 | t_A\right)$. The volume fraction is $\phi = 0.02$. The blue curve gives $P(\bar{s}_3 | t_A)$ for a subsample of a glassy state, and the black is the corresponding result for the entire simulation box. The value of $t_A = 0.5D_E^{-1}$. (b-d) same as (a) except the values of t_A vary as indicated. In the inset in (d) I also show $P(\bar{s}_3 | t_A)$ for another subsample in red. The structural features of the two subsamples are shown in Fig. 2.9.
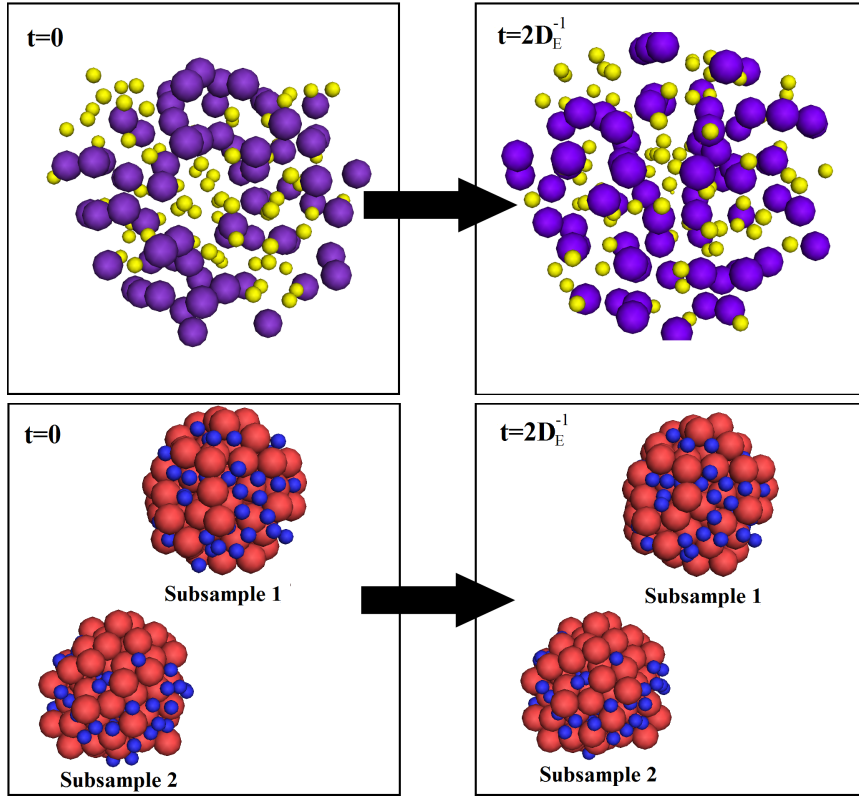
Figure 2.9: Illustration of the time evolution of particles within $\xi = 3.3a_s$. The panels on top are for a liquid ($\phi = 0.02$) at two times ($t = 0$ and $t = 2D_E^{-1}$). Small particles are colored in yellow and large particles are in violet. The bottom panels show two different subsamples at $\phi = 0.2$, whose $P(\bar{s}_3|(t_A))$ for $t_A = 12.5D_E^{-1}$ are shown in the inset in Fig. 7(d), evolve over time. Blue spheres represent small particles and red corresponds to large particles.

namics of supercooled liquids and the reason for emerging dynamic heterogeneity is attributed to the violoation of law of large numbers. Furthermore, to illustrate the latter argument, I calculate the structural entropy, s_3, in 3-dimensions, and show that the law of large numbers is violated regarding s_3 in supercooled liquids and glassy phases.

With the confirmation of the establishment of glasses for colloidal suspensions, in following chapters, I will discuss about the other interesting questions regarding supercooled liquids and glasses addressed.

Chapter 3: Bond orientational order (BOO)

3.1 Bond orientational order in supercooled liquids and glasses

As discussed in previous chapters, a structural order that can be directly linked to the slowing-down of dynamics has not been found in glass-forming liquids. Indeed, as we have seen in Wigner glasses, the static structures of glass-forming liquids, which are characterized by pair correlation functions, change little so that no divergence in any static length scale is observed in supercooled phases as well as in glassy phases. On the other hand, some recent studies claim [51–53] that some sort of bond rather than a positional ordering linked to a static pair correlation plays a key role during the vitrification processes of glass-forming liquids. They found a strong correlation between an emergence of bond orientational order (BOO) and mean-squared displacements, which suggests that the sluggish dynamics of supercooled liquids is attributed to the emergence of orientationally structured clusters impeding the movements of surrounding particles. In fact, because the glassy states are attainable only when the crystalization is suppressed due to the geometric frustrations, we can relate the role of BOO in the crystalization process to the formation of glasses.

In this chapter, I examine the static and dynamic aspects of bond orientational

order in soft sphere mixtures and Wigner glasses in order to shed light on the role of BOO in the formation of glasses. In addition, the dynamic behaviors of BOO are analyzed within the MCT framework to clarify the connection of BOO with the slowing down of dynamics in supercooled liquids.

3.2 Definitions

3.2.1 Bond Orientational Order

Bond orientational order parameter, Q_l, which was first introduced by Steinhardt et al [54], measures the extent of orientational ordering of liquids and glasses in three dimensions. The basic idea of Q_l is that the orientational order of bonds can be quantified by spherical harmonics Y_l^m. Because l represents the symmetry group of rotations, $l = 4$ corresponds to a simple cubic bond order whereas $l = 6$ an icosahedral order. More systematically, in order to calculate Q_l, a set of bonds should be defined first. Note that a bond does not indicate a chemical bond such as a hydrogen bond or a salt bridge but a vector joining two adjacent particles separated by the distance less than a cut-off distance r_0. Although 1.2 times average particle-particle distance $(1.2a_s)$ was used for r_0 in the original paper, the exact value of r_0 may vary according to the system. In the work presented this chapter, I fixed r_0 at $1.4a_s$ that corresponds to first local minimum in $g(r)$. Once the bonds are chosen, m-dependent BOO parameter, q_{lm}, is defined by

$$q_{lm} = Y_l^m (\varphi, \theta) \tag{3.1}$$

where $Y_l^m(\varphi, \theta)$ is spherical harmonics, φ and θ are an azimuthal and a polar angle of each bond, respectively. Then, q_l is calculated by

$$q_l = \sqrt{\frac{4\pi}{2l+1} \sum_{m=-l}^{l} |\langle q_{lm} \rangle|^2} \qquad (3.2)$$

where $\langle \cdots \rangle$ means average over an appropriate set of bonds. If we only consider even l-values, q_l is rotationally invariant.

One of recent advances regarding BOO is that the crystal structures of liquid and glasses can be detected more accurately by averaging BOO parameters over first neighbors including the particle itself [55]. Thus, it is of interest to calculate the averaged value, Q_l, that reads

$$Q_l \equiv \frac{1}{N_k+1} \sum_{k=0}^{N_k} q_l^{(k)} \qquad (3.3)$$

where k is the index for neighbors, N_k is the number of neighbors including the particle itself, and $q_l^{(k)}$ is the value of Q_l for kth neighbor. Zeroth neighbor stands for the particle itself. By taking average Q_l over all the neighbors, we can take into account second shell neighbors as well as first shell. Finally, a time-average of Q_l over the structural relaxation time τ_α, $\bar{Q}_l$ is given by

$$\bar{Q}_l \equiv \frac{1}{\tau_\alpha} \int_0^{\tau_\alpha} Q_l dt. \qquad (3.4)$$

3.2.2 Dynamic anisotropic measures: $\psi(t)$ and $K_{xy}(t)$

Alternative measures of BOO, $\psi(t)$ and $K_{xy}(t)$, were also used previously in the context of supercooled liquids [56]. Contrary to Q_l, these quantities were used to probe the dynamic behavior of BOO. $\psi(t)$ is a time-dependent parameter

45

quantifying the rotation of bond orientations as a function of time. In details after a suitable sets of bonds are chosen in a similar way to being done with Q_l, $\psi(t)$ is calculated from the autocorrelation of the directional cosines of each bond, $\hat{r} = (\cos\alpha, \cos\beta, \cos\gamma)$ which is

$$\psi(t) = \langle \hat{r}(t) \cdot \hat{r}(0) \rangle \tag{3.5}$$

where $\langle \cdots \rangle$ means an average over ensembles. Evidently, $\psi(t)$ is related to the relaxation of local bond orientation.

Another quantity $K_{xy}(t)$, which was first considered by Alder [57] in one component hard sphere system, defined by

$$K_{xy}(t) = \langle \cos\alpha(t)\cos\beta(t)\cos\alpha(0)\cos\beta(0) \rangle \tag{3.6}$$

is an alternative measure of the local bond orientational orders. It is known that $K_{xy}(t)$ is associated with the influence of pair correlation on a stress tensor correlation function in hard sphere system but there is no clear interpretation of K_{xy} for other systems. Nevertheless, I expect that K_{xy} measures a relaxation of BOO as $\psi(t)$.

As it has been done for Q_l, time average can also be taken to compute $\bar{\phi}$ and $\bar{K}_{xy}$ following

$$\bar{\psi} = \frac{1}{\tau_\alpha} \int_0^{\tau_\alpha} \psi(t)dt \quad , \quad \bar{K}_{xy} = \frac{1}{\tau_\alpha} \int_0^{\tau_\alpha} K_{xy}(t)dt \tag{3.7}$$

3.3   Models and simulation details

I numerically studied two different systems: one is a soft-sphere mixture and the other is a binary mixture of highly charged colloidal suspensions. For soft-spheres, the interaction between two particles i and j seperated by r_{ij} is,

$$V_{SS}\left(r_{ij}\right) = \epsilon \left(\frac{\sigma_i + \sigma_j}{2r_{ij}}\right)^{12} \tag{3.8}$$

where σ_i (σ_j) is the diameter of ith (jth) particle. For the colloidal suspensions, DLVO potential given by Eq. 2.1 is used.

In the soft-sphere system, I simulated a binary mixture of small and large spheres using two different size ratios, $\sigma_1/\sigma_2 = 1.1$ or 1.3. For colloidal suspensions, I prepared the mixtures of small and large particles with two different mixing ratios. In first set, I used the same number of small and large particles whereas in the other four times larger number of small particles are used so that the resulting molar ratio of small to large particles is 4. All other parameters are the same as described in chapter 2.

The control parameter tunned to induce glas transition is different for soft-spheres and suspensions. In soft-spheres, a volume fraction is fixed at 0.5 but a temperature is used as a control parameter. The thermodynamic state of soft-sphere system can be characterized by a single parameter Γ [58,59], which is defined by

$$\Gamma_{\text{eff}} = \frac{n\sigma_{\text{eff}}^3}{T^{1/4}} \tag{3.9}$$

where n is the number density, T is the temperature in tfhe unit of ϵ/k_B, and, σ_{eff}

is the effective size of the particle equivalent to a single component fluid,

$$\sigma_{\text{eff}}^3 = X^2\sigma_{11}^3 + 2X(1-X)\sigma_{12}^3 + (1-X)^2\sigma_{22}^3 \qquad (3.10)$$

with the molar ratio of small particles is X, and $\sigma_{nm} = (\sigma_n + \sigma_m)/2$ for $n, m = 1, 2$ [60]. Therefore, I use Γ as the control parameter in soft-spheres rather than the temperature. In contrast, for colloidal suspensions, the control parameter is volume fraction (or density of particles) instead of temperature so that the temperature was fixed at $298K$ in the simulation and ϕ was varied.

I integrated Brownian dynamics equation of motion for both systems. For the soft-sphere systems, the simulation was started from the highest temperature, and subsequently the system was cooled down to obtain the desired temperatures. For colloidal suspensions, the simulation procedure was the same as used in the chapter 2.

3.4 Results

One may argue that the growth of bond orientational orders is merely a consequence of positional ordering. To rule out this possibility, I calculated the orientational distributions of short-time displacements, $P(\varphi, \cos\theta)$, of an azimuthal angle, φ, and a cosine of a polar angle, $\cos\theta$, of each displacement vector. Here, the orientations of the displacements are estimated with respect to an arbitary reference frame, which is spatially fixed. Because translational diffusions that are responsible for the positional ordering are isotropic, if the ordering of BOO is subordinate to the positional ordering, we would observe no dependence on specific orientations

in $P(\varphi, \cos\theta)$. However, it turns out that the displacements even in short time are correlated with the orientations. The plot of $P(\varphi, \cos\theta)$ presented in Fig. 3.1 visualizes that the diffusive motions of the particles are anisotropic for supercooled liquids ($\phi = 0.1$). By contrast, the orientaional distribution of short-time displacements in liquids ($\phi = 0.03$) have no directionality. Thus, we may deduce that the ordering of bond orientations is not just a consequence of the positional ordering but play a role in the development of supercooled liquid states.

Afterwards, I analyzed the mean-squared displacements and the radial distributions of soft-sphere systems to determine the thermodynamic states of each trajectory. Both quantities show that the mixture of soft-spheres with $\sigma_1/\sigma_2 = 1.1$ is frozen into a crystal at $\Gamma \geq 1.47$ whereas the mixture with $\sigma_1/\sigma_2 = 1.3$ crystalization is avoided resulting in glass formed at high Γs. However, the type of the crystal was not easily identified solely by the pair correlation functions. For colloidal suspensions, in both mixing ratios, the system undergoes the liquid-to-glass transition without the crystalizations.

For further investigation of orientational ordering, I calculated the BOO parameter, Q_l, in soft-spheres and collidal suspensions. In Fig. 3.4, I plot $(x, y) = (Q_4, Q_6)$ for individual particles to characterize BOO for various Γs and ϕs. Because Q_l does not contain any time information, the correlation map (Q_4, Q_6) is considered a static quantity. The correlation map shown in Fig. 3.4a suggests that the crystal made of soft-sphers for weakly frustrated system (the size ratio is 1.1) is a face centered cubic (FCC) which has a broad distribution of Q_4 and a relatively large value of $Q_6 \approx 0.5$ [61]. Also, the correlation map reveals that although liquids
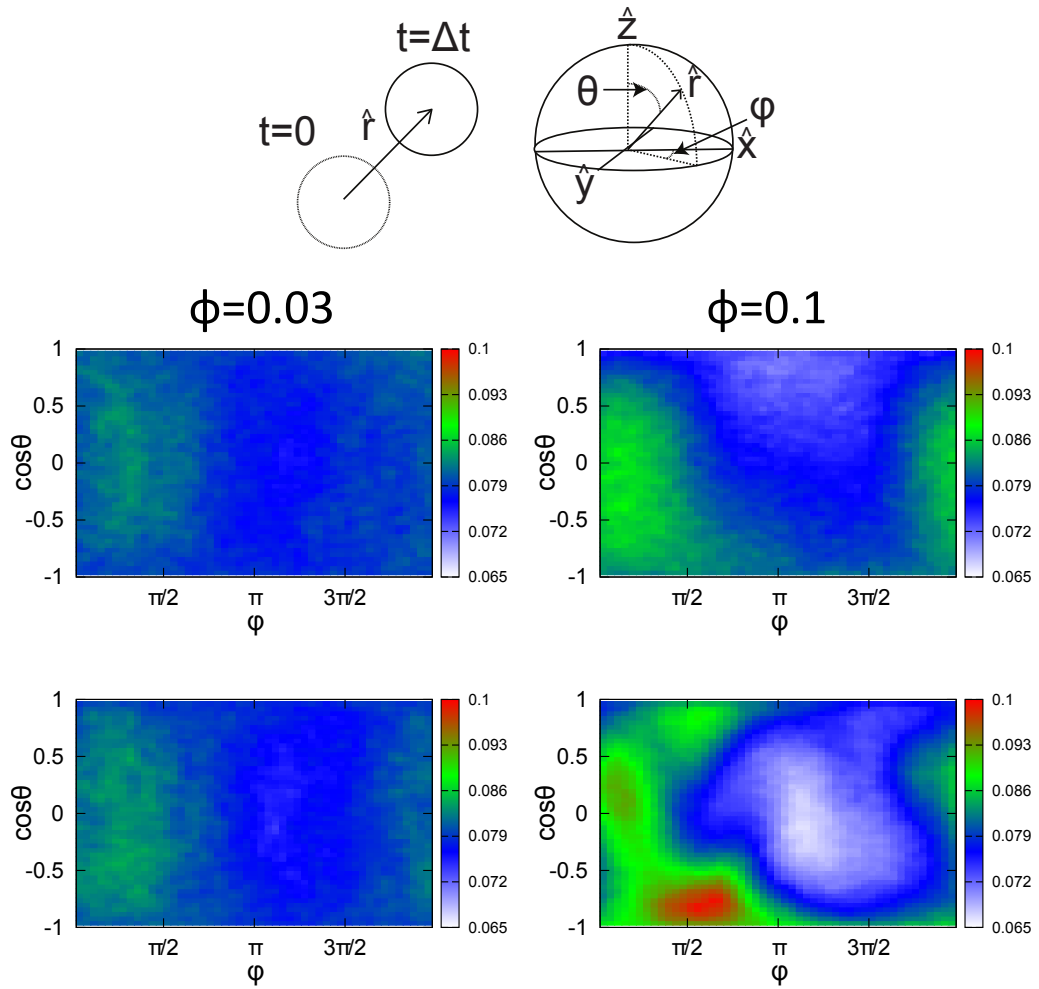
Figure 3.1: Two dimensional distribution of the orientations of the displacements during a short time interval, $P(\varphi, \cos\theta)$, in colloidal suspensions with 1:1 molar ratios. An orientation of the displacement is expressed in terms of an azimuthal angle, φ, and a cosine of a polar angle, $\cos\theta$ with respec to an arbitary reference frame. Upper and bottom panes correspond to $\Delta t \approx \sqrt{0.25a_s^2/D}$ and $\Delta t \approx \sqrt{0.5a_s^2/D}$, respectively, where a_s is the average particle-particle distance and D is a diffusion coefficient. The results for two different ϕs, $\phi = 0.03$ and $\phi = 0.1$ are shown in left and right columns, respectively.

and glasses have slightly different average values for Q_4 (0.20 for liquids and 0.16 for glasses) the correlation maps are generally overlapped with each other. This implies that liquids and glasses cannot be distinguished only using Q_4 and Q_6. For Wigner glasses, the determination of thermodynamic states using Q_l is more difficult. Fig. 3.4b illustrates that liquid, supercooled liquid, and glassy phases are degenerate so that the static quantity Q_l cannot be used for the detection of glassy phases.

In order to ascertain that the structure of soft-spheres of $\sigma_1/\sigma_2 = 1.1$ system is FCC, I calculated the pair correlation functions. Fig. 3.4 shows that the resulting structures of the soft-spheres at high Γ is a crystal whereas the mixture of soft-spheres of $\sigma_1/\sigma_2 = 1.3$ does not exhibit long range orders.

On the other hand, the dynamic bond orientational orders, $\psi(t)$ and $K_{xy}(t)$, are strongly correlated with the dynamic transitions in Wigner glasses. Estimated $\psi(t)$ and $K_{xy}(t)$ are presented in Fig. 3.4 and Fig. 3.5. In order to extract the relaxation time of BOO, I fit both quantities to stretched exponential $\sim \exp\left[-(\omega_r t))^\delta\right]$ (Fig. 3.5a-d). In the stretched exponential fits, the structural relaxation time, τ_α, is substituted into ω_r^{-1} so that ω_r^{-1} measures the relaxation of bond orientational orders. Fig 3.4c and Fig 3.5e clearly show the divergence of relaxation in bond orientational orders with increasing ϕ. As it has been done with τ_α, ω_r is fit to the power-law, $\omega_r \sim \omega_r^{(0)} \left(\phi^{-1} - \phi_A^{-1}\right)^{-\gamma_{\omega_r}}$. Both ω_r^{-1} for $\psi(t)$ and $K_{xy}(t)$ are fit well to the power-law with a universal exponent $\gamma_{\omega r} \approx 1.0$ and different $\phi_A \approx 0.1$ for the binary mixtures and $\phi_A \approx 0.12$ for 4:1 mixtures (Fig. 3.5f).
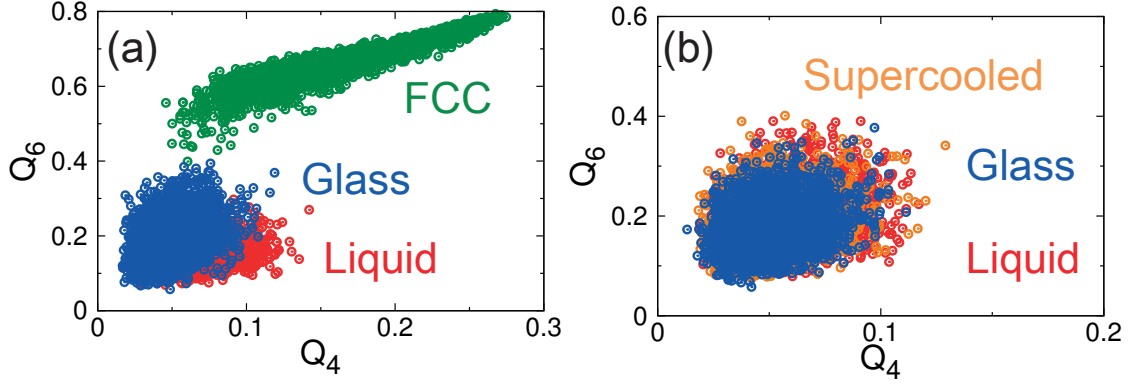
Figure 3.2: (a) A correlation map of 6th order BOO parameter, Q_6, and 4th order parameter, Q_4, for liquids, glasses and face-centered cubic (FCC) crystals made of soft-spheres. Liquid samples are taken from $\Gamma = 0.95$, and glass ones are from $\Gamma = 1.50$ of $\sigma_1/\sigma_2 = 1.3$ whereas FCC crystals are made of soft-spheres with $\sigma_1/\sigma_2 = 1.1$ and $\Gamma = 1.47$. The plot shows clear separation of FCC phase from liquid and glassy phases but glassy and liquid phases are moderately overlapped. A snapshot of FCC structure taken from the simulation is also presented. (b) The same correlation map for colloidal suspensions. In contrast to soft-spheres, the distributions are the same for liquids ($\phi = 0.03$), supercooled liquids ($\phi = 0.1$), and glasses ($\phi = 0.2$).
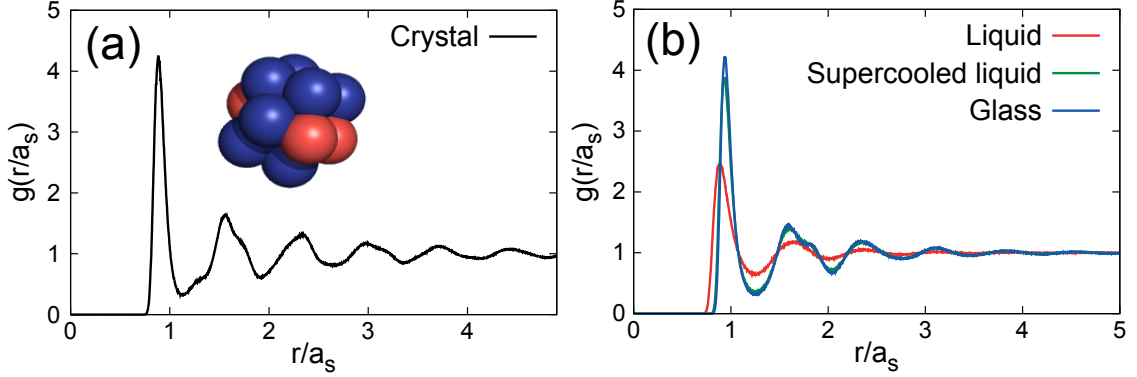
Figure 3.3: (a) Pair correlation function, $g(r)$ of soft-spheres for $\Gamma = 1.5$ and $\sigma_1/\sigma_2 = 1.1$ (Crystal) (b) $g(r)$ for $\Gamma = 0.95$(Liquid), 1.43(Supercooled liquid) and 1.5(Glass) using $\sigma_1/\sigma_2 = 1.3$. This system is not crystalized but vitrified.

3.5 Discussion

First, I found that a diffusion is no longer isotropic but has a directionality in deeply supercooled liquids. However, the anisotropic feature was smeared out when an ensemble average is taken. That is because the orientation of a reference frame is arbitarily chosen so that the distributions of φ and θ from each sample are superimposed with random offsets for φ and θ. These offsets may cancel out the deviation in the distribution functions. Thus, this phenomenon can be understood as an onset of an ergodic-to-nonergodic transition in BOO in that the anisotropicity observed in time average disappers in ensemble averages.

Another remark is that the diverging behavior of BOO for different mixing

ratios are similar to each other. Only a critical volume fraction where the ergodic-to-nonergodic transition occurs differs for 8:2 mixtures and 1:1 mixtures. This result implies that the mechanism that controls the relaxation in MCT regimes is uncorrelated with the degree of frustration that is determined by a polydispersity of the systems. The meaning of this observation becomes more straightforward by the comparison with monodisperse cases. Rosenberg et al reported in ref [29] that a monodisperse system consisting of small particles is frozen into a body centered cubic (bcc) at $\phi \approx 0.023$, which is much lower than the dynamic transition volume fraction, $\phi_A \approx 0.1$. Thus, we can surmise that the polydispersity of the system has nothing to do with the relaxation mechansim in ergodic states but only prevents a crystalization by providing geometric frustrations. It might be interesting to examine the role of polydispersity in non-ergodic phases beyond $\phi > \phi_A$ but it was formidable because of diverging relaxation time.

Finally, the relation of a static BOO parameter, Q_l, to dynamic BOO parameters, $\psi(t)$ and $K_{xy}(t)$, should be discussed. Despite the rapid increases of $\psi(t)$ and $K_{xy}(t)$ at $\phi \to \phi_A$, Q_l seems to remain stationary. Also, I could not detect so called Medium Range Crystal Order (MRCO) that is identified by a group of particles having non-zero Q_l. These results are inconsistent with the studies regarding very weakly frustrated systems such as polydisperse LJ particles or hard spheres with the fluctuations in sizes less than 6% where the strong correlations between Q_l and the mean-squared displacements are reported in ref [51, 53]. Furthermore, the authors argue that the dynamic heterogeneity may be a consequence of the emergence of MRCO. However, this possibility is ruled out in soft spheres and

Wigner glasses because these systems still exhibit significant dynamic heterogeneity without any crystal-like order. In addition, the discrepancy in the behavior of static BOO parameters and dynamic ones near critical points reminds us that the sluggish structural relaxations in ergodic regime ($\phi < \phi_A$) may be purely dynamic phenomea rather than thermodynamic. Such decorrelations of static and dynamic quantities are also reported in hard sphere systems where the dynamic length scales grows faster than static length scales by four order of magnitudes [62,63]. Therefore, the dynamic transition points T_A or ϕ_A can be considered a critical point at which all dynamic length scales related to both positional and bond orientational orders diverge but static length scales are still finite.

3.6   Summary

The static and dynamic aspects of BOO are under investigations using soft-spheres and Wigner glasses. In contrast to static BOO parameters, Q_l, which change little upon cooling or compressing, the dynamic parameters of bond orientations diverge following a power-law with a universal critical exponent varying according to the system as T or ϕ approaches to a critical temperature or volume fraction. As observed in translational ordering, the static quantity Q_l appears to have nothing to do with the dynamics of BOO, which supports the idea that the relaxation mechanism in ergodic regimes is attributed to purely dynamic factors rather than static structures. However, because the role of BOO in the RFOT regime ($T < T_A$ or $\phi > \phi_A$) is still obscure, further investigations for glassy phases would be desirable

in the future with more powerful computational resources and techniques.
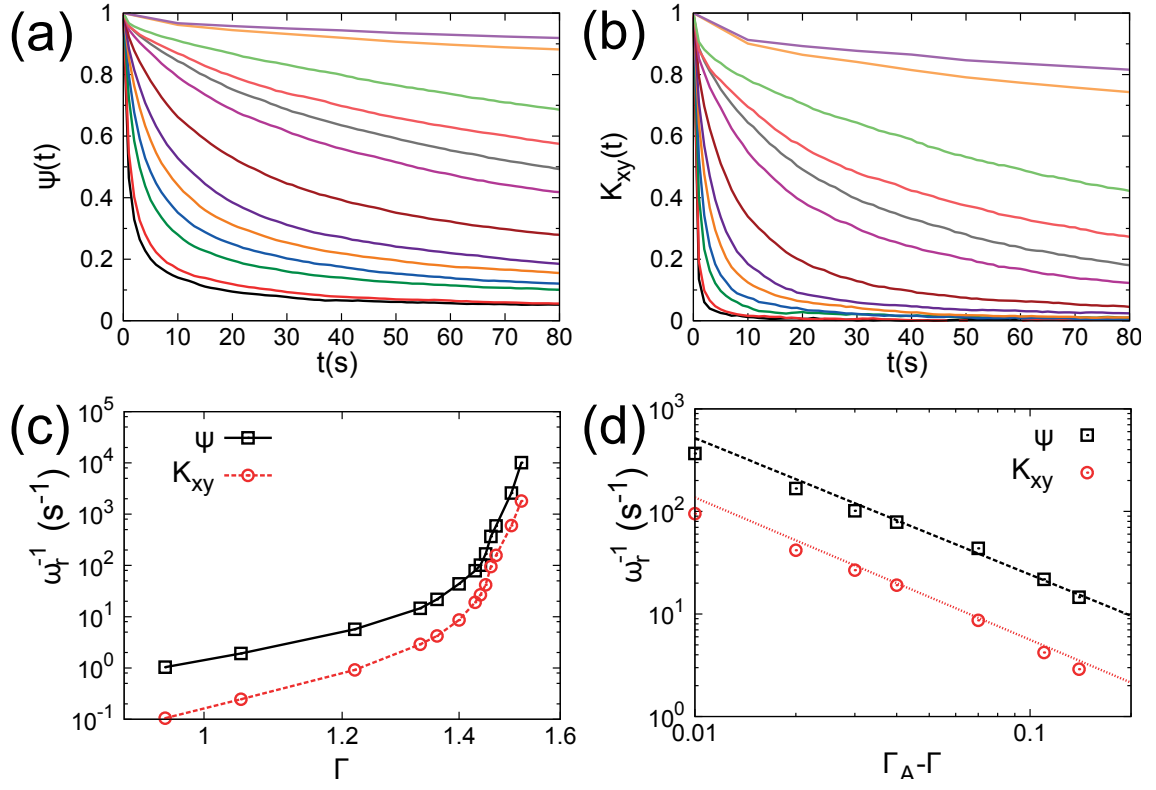
Figure 3.4: (a) (b) Dynamic BOO parameters, $\psi(t)$ and K_{xy} for soft-spheres. The presented results are $\Gamma = 0.95, 1.05, 1.22, 1.33, 1.36, 1.40, 1.43, 1.44, 1.45, 1.46, 1.47, 1.5$ and 1.52 from bottom to top. (c) The inverse of ω_r, which is estimated from the stretched exponential fits $\psi(t)$ or $K_{xy}(t) \sim A \exp\left[-(\omega_r t)^\delta\right]$. (d) Power-law fits of ω_r^{-1}. Both ψ and K_{xy} fit well to the power-law $\sim (\Gamma_A - \Gamma)^{-\gamma}$ with $\Gamma_A = 1.47$. The resulting exponent, γ, is 1.33 for ψ and 1.38 for K_{xy}.
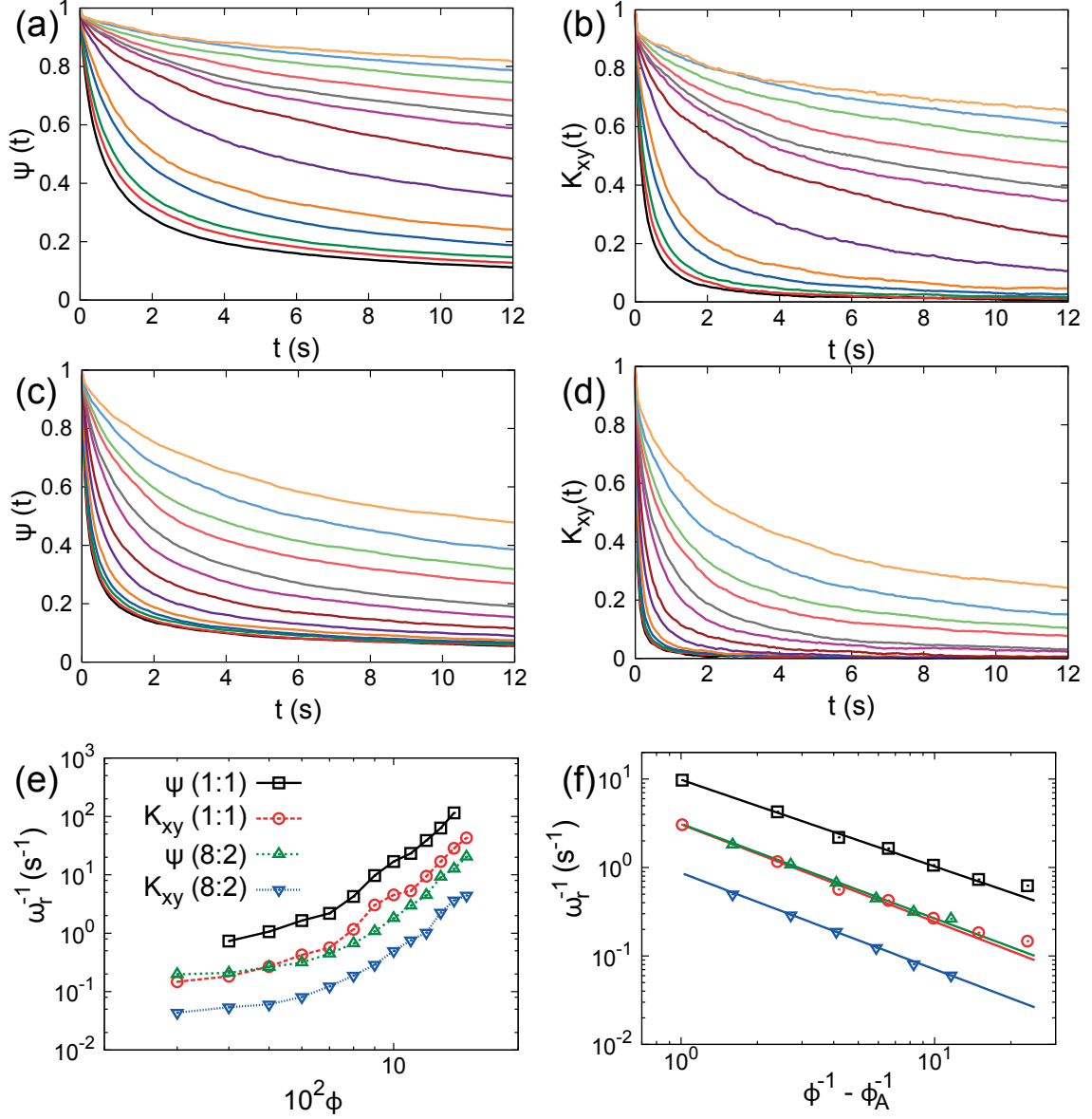
Figure 3.5: (a) (b) (c) (d) The same data shown in Fig 3.4a-b for colloidal suspensions with 1:1 (a,b) and 8:2 (c,d) mixtures of small and large polyballs. The volume fractions presented here are from 0.03 to 0.15 with 0.01 increment from bottom to top. (e) The same plot as in 3.4c. (f) The power-law fits of ω_r^{-1}. The power-law exponent, $\gamma \approx 1.0$, seems to be universal regardless of a mixing ratio and a type of parameters (ψ or K_{xy}).

Chapter 4:   Macromolecular crowdings: Literature review

In previous chapters, I examine thermodynamics of dense fluids that is frozen into glasses at a certain volume fractions. Not surprisingly, such a dense-fluid-like system is universally found in nature. Among those, in this and following chapters, I will study the biological applications of highly packed systems in the context of the macromolecular crowding effects of inert particles on biopolymers.

A living cell contains various kinds of biomolecules from tiny Ubiquitins to gigantic cytoskeleton structures that are necessary in maintaining their biological activities. These biomolecules occupy significant fraction of cell volume and create macromolecular crowding environment inside of the living cells. The exact volume fraction is still controversial, but several experimental, theoretical, and computational researches have shown that 20%-40% of volume occupancy by crowding particles can dramatically affect thermodynamics and kinetics of crucial biochemical reactions such as protein folding, enzyme kinetics, and ligand bindings [64,65]. The influence of crowding effects on biopolymers has been illustrated by a number of experimental and computational studies.

In this chapter, I review recent experiments and computational studies related to the effects of macromolecular crowding on various biopolymers.

4.1 Toward *in vivo* conditions: mimicking *in vivo* crowding in *in vitro* experiments

4.1.1 Composition and volume fractions of *in vivo* crowdings

Macromolecular crowding environments of a cell has been intensively studied in the connection to the realization of *in vivo* conditions. For instance, a part of a bacterial cytoplasm taken from an electron tomography and a computational modeling shown in Fig. 4.1 [66,67] reveal us how the interior of a cell is crowded. Indeed, these such dense-fluid-like environments can make huge impacts on bio-reactions that cannot be captured in *in vitro* experiments. Notwithstanding long history of the recognition of macromolecular crowding *in vivo*, however, even the exact volume fractions in the interior of a cell are still obscure. The problem is that because the excluded volume of crowding particles are very dependent on the compositions and the shapes of crowders, the calculation of volume fractions would be very inaccurate without the considerations of actual compositions of cellular components that are still unknown. For example, with 400g/L of concentrations of macromolecules, which is a typical value for the concentration of biomolecules in bacterial cytoplasms, the estimated volume fraction ranges from 5% to 40% according to the shapes and the sizes of molecules. This large variation in volume fractions often make it difficult to directly compare *in vitro* experiments to some phenomena observed *in vivo*. Therefore, the volume fractions of crowding agents have been considered just a guide for a qualitative analysis not a quantitative one.
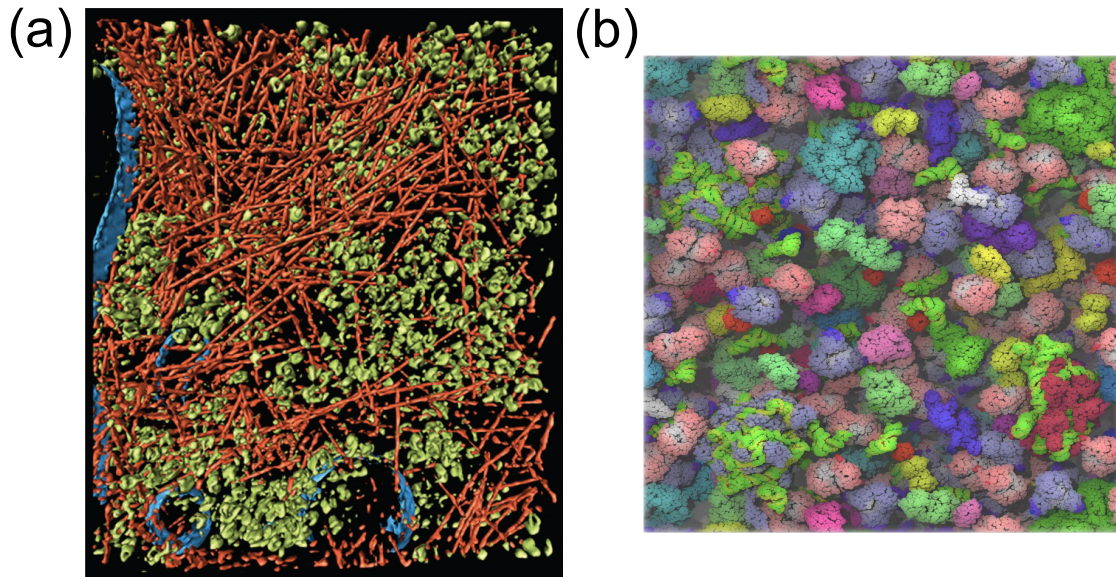
Figure 4.1: Visualization of crowded cell interior. (a) An electron to-mography of *Dictyostelium discoideum* illutstrates that the interior of a cell is occupied by complex cytoskeleton structures and a variety of molecules. Red lines are actin filaments and green bodies are ribosomes. The picture is adapted from ref [66] . (b) An example of computational modeling of bacterial cytoplasms. The figure is taken from ref [67].

4.1.2 Crowding agents

In *in vitro* experiments, various polymers and polysaccharides are used as crowding agents to generate a cell-like crowding environment. Among those molecules, the most popular one is Polyethylene glycol (PEG). PEG is a polymer of ethylene oxide that generally has little attractive interaction with proteins and nucleic acids. Thus, PEG only has purely repulsive interactions that are responsible for the excluded volume. Because it lacks attractive interaction with other molecules, in most of experimental and numerical studies, it is modeled by a hard or soft sphere whose radius is approximated by its radius of gyration, R_g, which can be estimated from an equation, $R_g = 0.0215 M_w^{0.583 \pm 0.031}$ nm where M_w is a molecular weight of PEG in Da [68, 69].

Ficoll is an alternative crowding agent used in recent crowding experiments. Ficoll is a highly branched hydrophilic polysaccharide whose radius ranges from 2-7nm. Because of its high degree of branching, it has more spherical shape than other linear polymers. It has little activity with other reagents as well as proteins and nucleic acids. Other polysaccharides and proteins lacking attractive interactions such as dextrans, defatted bovine serum albumin are also often used as crowding agents.

4.2 Crowding effects on various biopolymers

With the aforementioned crowding agents, a number of *in vitro* experiments have been performed to elucidate the crowding effects on various biopolymers.

4.2.1 Proteins

The influence of macromolecular crowdings on proteins have gained attentions since pioneering researches on the activity of proteins in polymer solutions revealed the substantial effects of excluded volume interactions 1960s and early 1970s [70]. After that, the quantitative assays using various experimental techniques have shown that the R_g of proteins such as ω-MVIIa-gly, BPTI and α-TS can be decreased by up to 60% of its original value in the presence of crowding agents [71]. Some circular dichroism spectroscopy, fluorescence correlation spectroscopy, and NMR spectroscopy studies also reported that the stability of folded states of proteins such as ribonuclease A and α-synuclein is largely enhanced by increasing the concentrations of dextrans, Ficolls and PEG [72,73]. There are putative experimental and numerical evidences confirming that crowding agents induce the stabilization of compact native structures of proteins.

The existence of crowding agents affect not only the stability of folded states but also the folding and unfolding rate of proteins. For example, the folding rate of VIsE protein is enhanced by two orders of magnitude in 30% (w/v) of Ficoll solutions [74]. By contrast, the unfolding rate changes little at the same concentration of Ficoll . This result indicates that the free energy landscape of unfolded states are shifted to make more compact structures favorable whereas the folded states are unaffected by crowding agents.

4.2.2 RNA

The conformational change of RNAs under crowding conditions has been elucidated through a number of *in vitro* studies. In a recent experimental paper, it was reported that the activity of ribozyme is considerably enhanced in the solution of neutral cosolutes by a factor of 2-6.6 [75]. To identify the origin of the enhanced activity, the structure of ribozyme in PEG solutions was examined by a small angle X-ray scattering (SAXS) experiment [76]. The SAXS measurement reveals that the R_g of ribozyme significantly decreases as the concentration of PEG increases, which indicates that the increased activity of ribozyme is mainly due to more population of folded RNA and the role of PEG is to generate attractive interaction between nucleic acid and stabilizes compact structures. These findings are consistently observed in other RNA such as the structural transition of human telomerase RNA [77].

4.2.3 DNA and chromatin fibers

The crowding effects on long DNA is first recognized in the sedimentation measurement of T4 DNA in poly-ethylene oxide (PEO) and poly-vinyl pyrrolidinone (PVP) solutions [78]. In his pioneering work, the author discovered that a long DNA is surprisingly collapsed into a small globular conformation at a certain concentration of monovalent salts and PEO or PVP. This remarkable condensation of DNA has gained further attention in the context of DNA packaging of bacteria phage [79, 80]. The first-order-like transition of DNA from a random coil to a globule is confirmed by a visualization using a fluorescent microscopy by Ueda

Random coil	Meta stable	Globule
0 v/v%	35 v/v%	40 v/v%

$20\,\mu\,\text{m}$
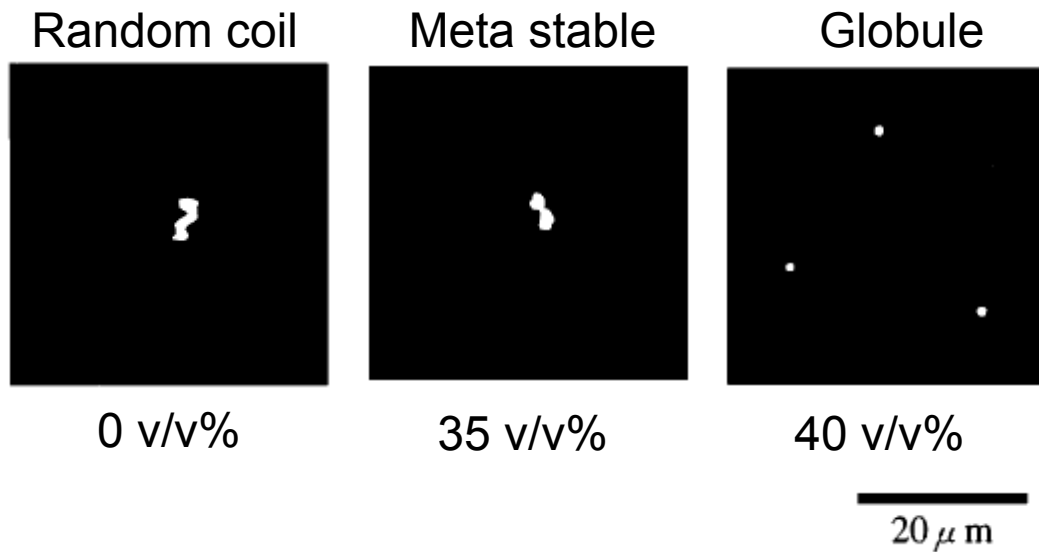
Figure 4.2: Condensation of $T4$ DNA. The figure shows that the conformational change of DNA in various concentration of 2-propanol. As the concentration of alcohol labeled below the picture increases, the size of DNA is reduced. The figure is reconstructed from FIG. 1 of ref [81].

and Yoshikawa [81]. They monitored the conformation of single molecule of 166kbp $T4$ DNA in various concentration of 2-propanol and observed a sudden drop in a long axis length at a certain concentration of the alcohol. Although the role of 2-propanol molecules is not clarified in their work, it can be considered an evidence for the existence of macromolecular crowdings effects on DNA.

Another interests in the crowding effects on DNA is the role of macromolecular crowdings in the looping dynamics of eukaryotic chromatin fibers. Because the size of chromatin fibers is gigantic compared to other biomolecules, the crowding

effects on the dynamics of the chromatin fibers would be very different from RNA and proteins. Although some researches shed light on these problems [82], a fundamental understanding of macromolecular crowding is still unsatisfactory and further investigation would be required.

4.3 Polydispersity of macromolecular crowding

Most of crowding experiments have been performed in monodisperse polymer solutions for a couple of reasons. First, from the bottom-up strategy's point of view, it is advantageous to dissect polydisperse crowding environments into several component systems and build up the final result from the analysis of simple rudimentary system. This strategy is beneficial because we can avert the difficulties resulting from the possible interactions between different crowding particles and focus on quantifying crowding effect itself. Second, because the theory for the thermodynamic effects of a polydisperse medium has not been established yet, the experimental discovery from polydisperse crowding environments cannot be appreciated in the traditional theories such as Scaled-Particle Theory (SPT). As pointed out in a recent review article by A.D. Elcock [64], however, relying on these theories that have successfully predicted the effects of excluded volume interactions "qualitatively" but have failed in explaining the experimental discoveries "quantitatively" is outdated. Thus, it would be strongly encouraged to scrutinize the conformational and kinetic changes of biopolymers in polydisperse polymer solutions that are closer to "real" situations *in vivo* in order to understand the influence of a cytoplasm-like environment on

biological functions of a variety of biomolecules. Furthermore, as I discussed in previous chapters, the impact of polydispersity in highly packed system is much more profound than in dilute solutions. Many interesting features observed in binary mixture of colloids such as diverging relaxation time, dynamic heterogeneity and broken ergodicity cannot be captured by the analysis of single component systems.

With these lights, a number of studies have been performed in the mixtures of various crowding particles. A typical example is the refolding dynamics of denatured muscle creatine kinase. In the refolding experiment of denatured kinase, it was shown that the refolding rate is largely increased in the mixture of calf thymus DNA and Ficoll70 [83]. This cooperative impacts of differently sized crowding agents are theoretically and numerically supported by subsequent papers [84, 85]. However, because the size of CT DNA is huge ($\sim 1.6\mu$m), the non-additive effects of these crowding agents should be considered limited case. The effects of polydispersity in the sizes of crowders are examined in more biologically relevant regimes with human telomerease RNA [77]. Denesyuk et al numerically studied the melting temperature of telomerases in the mixture of 10.4, 5.2, 2.6, 1.2 and 0.6nm hard spheres and showed that the effects of polydisperse medium of differently sized crowders are additive when the size of crowders is smaller than the size of the polymer. In other words, the crowding effects of polydisperse crowders are equivalent with the sum of the effects from each monodisperse component system.

The fluctuations in the shapes as well as the sizes of crowders have been examined. Waegele et al [86] investigated the changes of melting temperatures of Ubiquitin using IR measurements and found that the enhancement of the stability of

Ubiquitins due to crowding is more dramatic in dextran than Ficoll. They argue that the larger increase of the crowding effects in dextran solutions compared to Ficoll results from its aspherical shape rather than the chemical compositions or size effects. The larger impacts of anisotropic crowding particles are also claimed by some computational studies on homopolymers and proteins [87, 88].

These recent discoveries raise the issues for the necessity of more rigorous studies using polydisperse crowding environments. More systematic researches for the size and shape effects of crowding agents would be desirable.

4.4   Theoretical considerations

The effect of macromolecular crowding is qualitatively explained by entropy argument. Considering a system consisting of hard sphere solutes and crowding particles, the entropy loss of the system is roughly proportional to the volume of the sphere accessible to crowders. Thus, the hard spheres aggregate by vacating the crowding particles residing in interstitial space in order to reduce their excluded volume and to gain the entropy.

Scaled-Particle Theory (SPT) developed by Reiss et al [89] provides quantitative predictions based on this entropy argument. Following SPT, the chemical potential for inserting a hard sphere cosolute is given by

$$\frac{\Delta\mu}{kT} = -\ln\left(1 - \phi\right) + A_1\left(\frac{\phi}{1-\phi}\right) + A_2\left(\frac{\phi}{1-\phi}\right)^2 + A_3\left(\frac{\phi}{1-\phi}\right)^3 \qquad (4.1)$$

where

$$A_1 = R^3 + 3R^2 + 3R \qquad (4.2)$$

68

$$A_2 = 3R^3 + 4.5R^2 \tag{4.3}$$

$$A_3 = 3R^3 \tag{4.4}$$

where ϕ is the volume fraction of crowders, k_B is Boltzman constant, T is a temperature, and R is a radius of a hard sphere normalized by the size of crowders. However, not only the original SPT but the revised theory proposed by Minton [71] also have failed to predict the amount of reduction in R_g for some proteins and RNAs [76, 90]. The failure of SPT and the extended interests to the crowding effects in DNA and chromatin fibers invoke the further development of the theory explaining the phenomena in recent crowding experiments.

4.5   Questions addressed in this thesis

In this chapter, I reviewed various research effort on crowding effects of biopolymers from proteins to chromatin fibers. However, as we discussed above, a unified framework that can be applied to wide range of length scales for the sizes of a polymer and crowders is absent.. Although SPT provides some quantitative predictions, it turns out that SPT is insufficient to explain recent crowding experiments for RNAs and some intrinsically disordered proteins. Hence, the systematic approaches using all possible ranges of length scales would be interesting to extend our knowledge of crowding effects.

The crowding effects on semi-flexible chains are another intriguing question. Because DNA has about 50nm of a persistence length this length scale is not negligible for the crowders whose size is typically nano-meter scale. Thus, it would be

compelling to pose a question how the effects of crowders may change by introducing the bending rigidity of the polymer.

As we examined in previous sections, polydispersity of crowding medium recently has been focused on crowding researches. In particular, the effects of the aspherical crowders on semi-flexible chains has not been elucidated in computational works.

With these considerations, in following chapters, I will present Langevin dynamics simulation results using model systems consisting a polymer and explicit crowding particles to resolve the issues mentioned above. In chapter 5, first I examine the crowding effects on a self-avoiding walk model in the wide range of the size of crowders to provide some insight for the effect of crowders' size on macromolecular crowding. In chapter 6, the system of a semi-flexible chain, spherical and cylindrical crowders is examined to investigate the relation of polydispersity of macromolecular crowding to the conformational changes of DNAs.

Chapter 5: Effects of macromolecular crowders on the collapse of biopolymers

The crowding effects of inert particles have been intensively examined through many experiments and simulations using various crowding agents and compuational models. By "inert" I mean that interactions between the crowding agents and the biopolymer is determined by excluded volume interactions. However, a systematic quantitative anlysis relating the size of crowders to the crowding effects on finite-sized biological macromolecules has not been performed in the literatures. To resolve this problem, in this chapter, I will present molecular dynamics simulation results using a simple polymer model dispersed in explicit crowding particles and analyze the results with scaling arguments. Finally, the simulations results will be compared with recent experimental observation, which is a caricuture of intrinsically disordered proteins and unfoloded states of proteins.

5.1 Scaling arguments

In the crowding problems, the experimentally observable variable is the radius of gyration of a polymer as a function of volume fractions of crowders, ϕ, denoted by $R_g(\phi)$. Another relevant length scale is a radius of crowders, σ_c, and equivalently an

average crowder-crowder distance, D, which is obtained from $D = (4\pi/3)^{1/3} \sigma_c \phi^{-1/3}$.
If correlation between crowding particles is neglected, as in the case of small ϕ, then
the scaling ansatz for the crowindg problem is given by

$$R_g(\phi) = R_g(0) f(x) \tag{5.1}$$

where $x = R_g(0)/D$. In limit that the number of monomers in chain is sufficiently
large (ie $L \gg a$ where L is a contour length and a is a bond length of a polymer),
we can predict the behavior of $R_g(\phi)$ in two limiting cases.

(i) $x \sim O(1)$ case

When D is comparable to or less than $R_g(0)$, the crowding effects would be
not sufficient to alter global behavior of the chain. Therefore, we expect that the
chain properties such as the scaling relation, $R_g(0) \sim N^\nu$, are preserved for $R_g(\phi)$.
Thus, $f(x) \sim O(1)$, and

$$x = \frac{R_g(0)}{D} \sim \frac{R_g(0) \phi^{1/3}}{\left(\frac{4\pi}{3}\right)^{1/3} \sigma_c} \sim \frac{R_g(\phi) \phi^{1/3}}{f(x) \left(\frac{4\pi}{3}\right)^{1/3} \sigma_c} \sim 1. \tag{5.2}$$

Thus,

$$R_g(\phi) \sim \phi^{-1/3} f(x) \sim \phi^{-1/3} \tag{5.3}$$

(ii) $x \gg O(1)$ case

When the D is much smaller than $R_g(0)$, the crowding particles exert osmotic
pressure on the polymer. Thus, the resulting $R_g(\phi)$ would be $R_g(\phi) \sim N^{1/d}$, where
d is the dimensionality. Assuming $f(x) \sim x^\alpha$, we can obtain $\alpha = -\frac{4}{9}$ from $R_g(\phi) = R_g(0) f(x)$. As a result, the ϕ dependence of $R_g(\phi)$ is

$$R_g(\phi) \sim \phi^{-\frac{4}{27}} \tag{5.4}$$

With the scaling hypothesis as an approximate guide, I performed low-friction Langevin dynamics simulation of a self avoiding walk, which models a polymer in good solvent and can describe IDPs and unfolded proteins, in the presence of explicit crowding particles.

5.2   Methods

5.2.1   Model

I used a bead-spring model for the flexible polymer. A large spring constant is chosen so that the distance between two successive monomers remains approximately a constant. I chose Weeks-Chandler-Anderson (WCA) potential for excluded volume interactions between monomers, and soft-sphere potential for crowder-crowder and crowder-monomer interaction.

The energy function for the system consisting of the self-avoiding walk (polymer) and soft spherical crowders is

$$H_{tot} = H_B + H_{m-m} + H_{m-c} + H_{c-c}. \tag{5.5}$$

Here $H_B = K \sum_{i=1}^{N-1} (|\vec{r}_{i+1} - \vec{r}_i| - l_0)^2 / l_0^2$ is the bond potential along the polymer chain, K is the spring constant with l_0 being the bond length. I used WLC potential for soft-core repulsion potentials, so that $H_{m-m} = \sum_{i<j}^{N} \epsilon \left[(\frac{\sigma_{ij}}{r_{ij}})^{12} - (\frac{\sigma_{ij}}{r_{ij}})^6 \right] \Theta \left(\frac{\sigma_{ij}}{r_{ij}} - 1 \right)$ with $\Theta(\dots)$ being a Heaviside step function; The Lennard-Jones energy constant, ϵ, controlling the strength of the excluded volume interaction, and σ_{ij} is the distance between two particles in direct contact, given by $\sigma_{ij} = \sigma_i + \sigma_j$ with σ_i being the ra-

dius of a bead, where i and j are either the index for monomers in polymer chain or for crowding particles. Lastly, $H_{m-c} = \sum_i^N \sum_j^{n_c} \epsilon \left(\frac{\sigma_{ij}}{r_{ij}}\right)^{12}$ and $H_{c-c} = \sum_{i<j}^{n_c} \epsilon \left(\frac{\sigma_{ij}}{r_{ij}}\right)^{12}$ are the monomer-crowder and crowder-crowder repulsions, respectively. I simulated for N =50, 100, and adjusted n_c to achieve the range of crowder volume fraction ($\phi = n_c \times \frac{4}{3}\pi\sigma_c^3/V$, where $V = L_x \times L_y \times L_z$ is the volume of periodic box) between 0 and 0.4.

In order to compare my results with the results obtained from simulations with implicit crowders [91], I chose the same parameters used in ref [91]. In particular, the number of monomers is $N = 50$ and $\sigma_m = 5\sigma_c$. Other simulation parameters are listed in Table 5.1. Also, in order to investigate the effect of the size of crowders, I used $N = 100$ with $\sigma_c = 2.0\sigma_m$, $3.6\sigma_m$ and $7.2\ \sigma_m$ for $N = 100$.

5.2.2 Simulation details

In order to obtain adequate sampling of the conformational space of the system, I performed low friction Langevin dynamics (LFLD). I followed the same simulation procedure described in detail elsewhere [77,92]. The data for analysis were collected after 2×10^5 time steps for equilibration. The number of crowders varies according to chain conformation with the the average value being $\sim 10^4$ for $\phi = 0.3$. In particular, I implemented a multiple layered neighbor list to expedite the simulations. Details of this step needed to speed up the simulation are described in Appendix B

K	l_0	k_BT	Δt	ζ_m	ζ_c
1500ϵ	$1.11\ \sigma_m$	$0.6\ \epsilon$	$0.01\ \tau$	$0.05m\tau^{-1}$	$\zeta_m\left(\frac{\sigma_c}{\sigma_m}\right)$

Table 5.1: Parameters characterizing the model. Lennard Jones energy constant ϵ, the diameter of monomer σ_m and $\tau = \sqrt{\frac{m\sigma_m^2}{\epsilon}}$ are used as the unit energy, the unit length and the unit time. K is a spring constants for a chain connectivity between monomers, l_0 is a bond length between monomers of a chain, k_BT is a temperature, Δt is a simulation time step, ζ_m and ζ_c are the frictional coefficient for monomer and crowding particles, respectively.

5.3   Results and discussion

In the simulations, I defined a dimensionless quantity, $\lambda = R_g\left(0\right)/\sigma_c$ as a parameter for the size of crowders. Because λ is inversely proportional to σ_c, a large λ means a smaller crowder when $R_g\left(0\right)$, which only depends on the number of monomers, is fixed.

5.3.1   Compaction due to large crowders $(\lambda \sim 1)$

As described earlier, in order that the scaling arguments work for large crowders $(x \sim 1)$, the assumption that the statistical properties of the chain should not
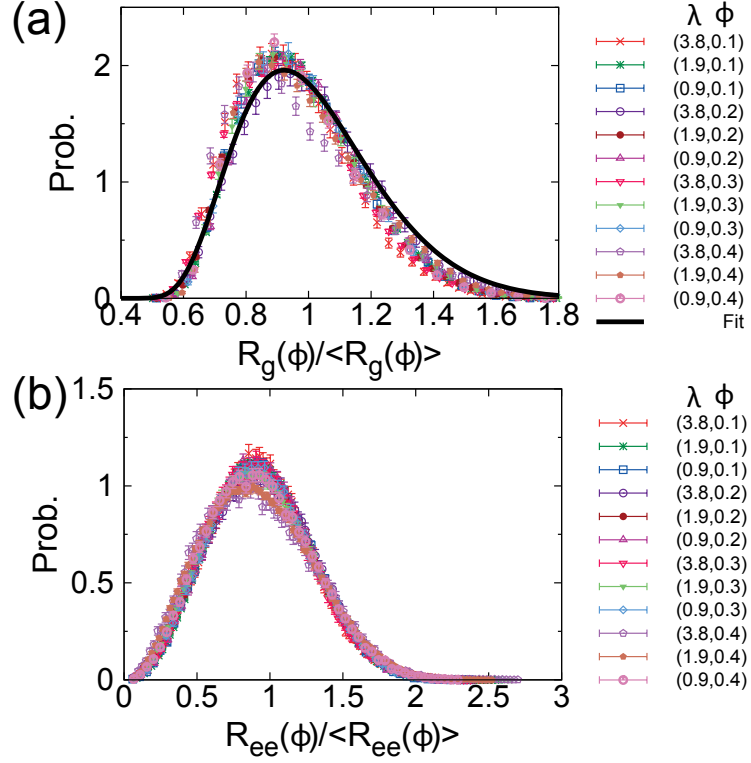
Figure 5.1: The distribution of the radius of gyration, R_g (a), and the end-to-end distance distribution R_{ee} (b), in the presence of large ($\lambda \sim 1$) for various λ and ϕ. All distributions are collapsed into a single curve. In particular, the distribution of R_g is fit well to the formula $P(t) = \mathcal{N} e^{-(bt)^{-15/4} - (bt)^{5/2}}$ with b=1.158 and $N = 13.92$.

be affected in non-zero ϕs. To test this hypothesis, first I calculated the distribution of R_g, and the end-to-end distance, R_{ee}. Fig. 5.1 confirms the hypothesis holds, for the SAW. In particular, the distribution of R_g denoted by $P(R_g)$ fit well to a universal equation [93],

$$P(t) = \mathcal{N}e^{-(bt)^{-15/4}-(bt)^{5/2}}, \tag{5.6}$$

where $t = R_g(\phi)/\overline{R}_g(\phi)$, b and $\mathcal{N}$ are parameters. Further analysis is carried out for $R_g(\phi)$ with various λ values.

Fig. 5.2a reveals that the crowding effects, which is measured by the reduction in R_g with increasing ϕ, becomes larger as λ increases. However, the amount of compaction is less than 8%. In particular, for $\lambda = 0.9$, the maximum reduction is only 3% from the $R_g(0)$. The compaction of the chain is consistently observed in $P(R_g)$. The distribution shows the gradual shift to more compact structures (Fig. 5.2b). The relation $R_g \sim \phi^{-1/3}$ derived from the scaling arguments fit well for $\phi = 0.2 - 0.4$ for $\lambda = 1.9, 3.8$ and 6.9 except $\phi = 0.4$ and $\lambda = 6.9$. These parameters correspond to the x values ranging from 0.7 to 2.9.

The radial distribution functions, $g(r)$, of crowding particles from the center of polymer [94] in Fig.5.2d illustrate that the crowding particles are depleted from the center of mass of the chain as visualized by the snaphot from the simulation (Fig.5.2a, the right panel). In these small x cases, the interstitial spaces of crowders are comparable to or larger than the size of polymer so that the polymer can experience only modest impact from crowding particles.

Also, I plotted $R_g(\phi)$ in log-log scale to test the scaling hypothesis (Fig. 5.3).
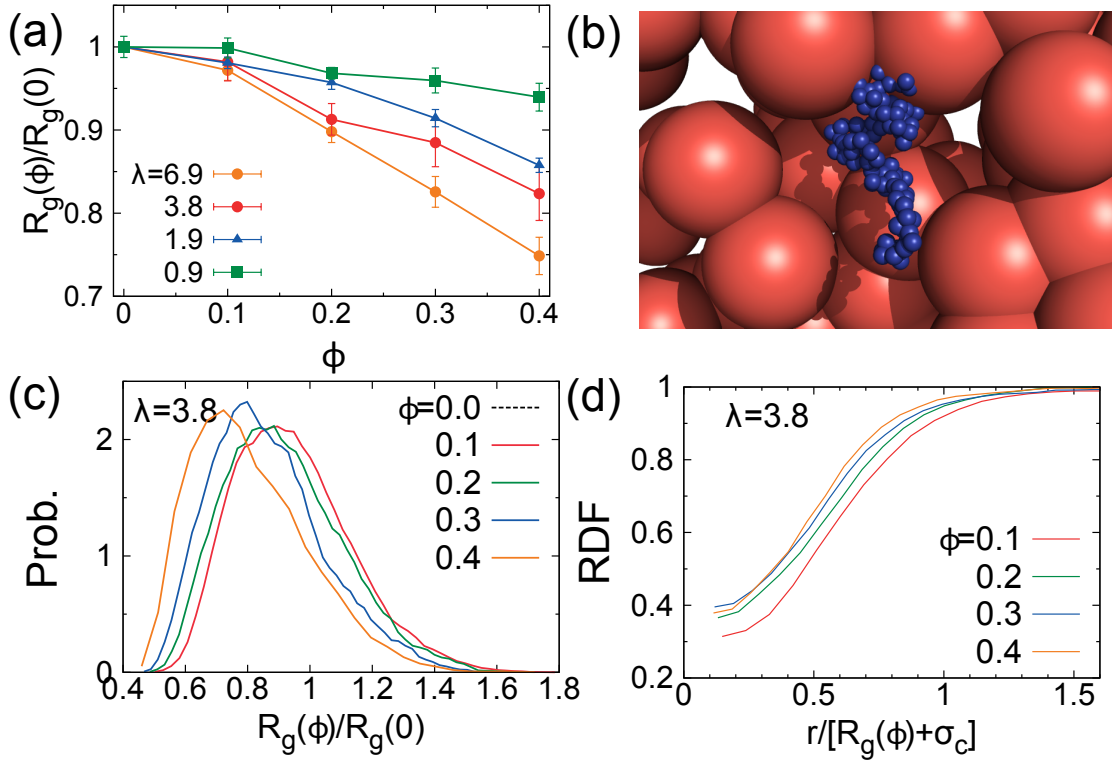
Figure 5.2: The crowding effects of large ($\lambda \sim 1$) crowders on the polymer. (a) $\overline{R}_g$ as a function of crowder volume fraction (ϕ). From the top to bottom is shown the crowding effect as a function of λ. (b) A snapshot of SAW chain and crowding particles for $\lambda = 1.9$ at $\phi = 0.3$. (c) Distribution of R_g, $P(R_g(\phi))$, as a function of ϕ at $\lambda = 3.8$. (d) Radial distribution function of crowders from the cneter of mass in the SAW for varying ϕ.
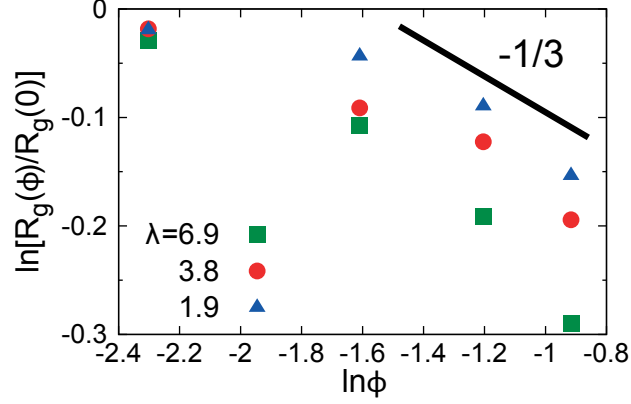
Figure 5.3: $R_g(\phi)$ for large crowders in log-log scale. The plot shows that $R_g \sim \phi^{-1/3}$ works adequetely for large crowders.

The relation $R_g \sim \phi^{-1/3}$ derived from the scaling arguments fit well for $\phi = 0.2 - 0.4$ for $\lambda = 1.9, 3.8$ and 6.9 except $\phi = 0.4$ and $\lambda = 6.9$. These parameters correspond to the x values ranging from 0.7 to 2.9.

5.3.2 Coil-globule transition due to small crowders $(\lambda \gg 1)$

As the size of crowders becomes smaller, the crowding effects on the polymer also increases. Finally, when ϕ reaches a certain critical volume fraction ϕ_c, which corresponds to a crossover volume fraction at which the scaling behavior changes from $R_g(\phi) \sim \phi^{-1/3}$ to $R_g(\phi) \sim \phi^{-4/27}$, it would expect that the polymer undergoes a first order transition from a random coil to a collapsed globule. Fig. 5.4 shows the dramatic collapse of the polymer $(N = 50)$ with $\lambda = 47$, which is a minimal model system for studying a chromatin looping dynamics. In the simulation, $R_g(\phi)$

significantly decreases even at small ϕ (~ 0.05) and, as ϕ increases further, at $\phi = 0.3$, the polymer is fully collapsed into a globule whose R_g is 30% of $R_g(0)$. The distribution of R_g is also shifted to the smaller value of R_g, which indicates the significant impact of crowding particles on the polymer (Fig. 5.4b). The change of the radial distribution function is also striking. Compared with $\lambda = 3.8$ case presented in Fig. 5.2d, in $\lambda = 47$ case, the crowding particles are completely vacated from the space occupied by the polymer as ϕ increases (Fig. 5.4c).

To ascertain that the structure of the polymer is collapsed, I calculated the shape (S) and asphericity (Δ) parameters, defined by $S = 27 \prod_{i=1,2,3} (\lambda_i - \bar{\lambda})/\bar{\lambda}$ and $\Delta = \frac{3}{2} \sum_{i=1,2,3} \lambda_i^2 / \bar{\lambda}^2$ where λ_i is an eigenvalue of gyration tensor, $\tilde{\mathcal{T}}_{mn} = N^{-1} \sum_{i=1}^{N} r_m^{(i)} r_n^{(i)}$, and $\bar{\lambda} = \mathrm{Tr}\tilde{\mathcal{T}}/3$ [95,96]. Both quantities measure the anisotropy of a given conformation, and are identically zero for a perfect sphere, and are nonzero for prolate or oblate-like shape. The ensembles of SAW polymer configurations illustrated in Fig.5.4a change from prolate-like shape at low ϕ [97,98] to a spherical shape as ϕ increases. The transition is relatively sharp (Fig. 5.4d) mirroring the decrease in $\bar{R}_g(\phi)$ (Fig.5.4a). At $\phi = 0.3$, the values of $S = 0.01$ and $\Delta = 0.07$, which indicates that the polymer coil is collapsed into an almost perfect spherical globule as a result of isotropic osmotic pressure exerted by the crowding particles.

5.3.3   Depletion potential should be determined globally

The computations in which crowding particles are explicitly modeled are intensive. In order to simplify the simulation it is tempting to use an implicit potential in
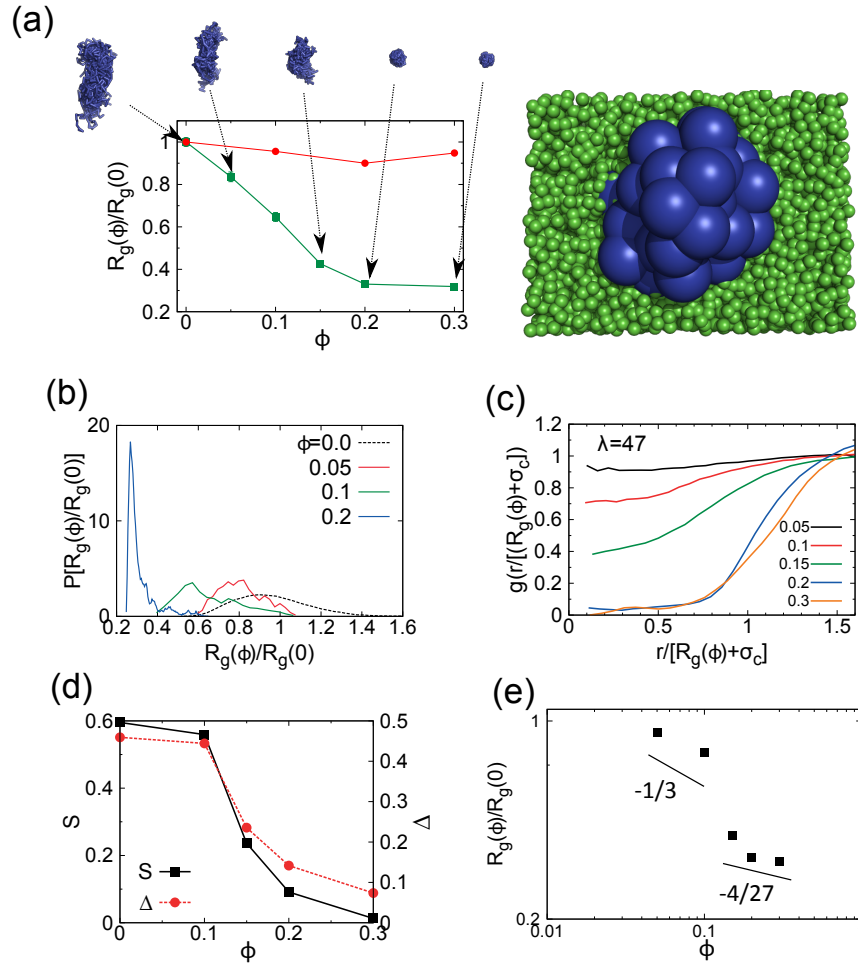
Figure 5.4: The conformational change of SAW for small ($\lambda = 47$) crowders. (a) $R_g(\phi)$ and ensembles of conformations are plotted (green square). The results with the implicit crowding potential [91] is shown in the same graph for comparison. The snapshot for $\phi = 0.2$ is drawn on the right. (b) The distribution of R_g. The compact structure is strongly favored for $\phi \geq 0.2$. (c) Radial distribution functions for small λ. At $\phi \geq 0.2$, the crowders are vacated. (d) The anisotropy and shape parameters to illustrate a coil-globule transition. (e) $R_g(\phi)$ in log-log scale. The plot shows the scaling argument holds for the SAW.

numerical simulations. Kim et al. [99] calculated the potential of mean force (PMF) between two beads each of which is located at the center of a small polymer in crowding conditions. The depletion potential of crowding particles were constructed from the PMF calculations and applied to a long polymers in order to scrutinize the effect of crrowding particles on chromatin compaction [91]. As shown in Fig.5.4a (red circles), they found a slight increase at R_g at $\phi = 0.2$ and attributed the apparent non-monotonic behavior of R_g to a repulsive barrier observed in the depletion potential created from their PMF calculations. The simulation with the SAW and explicit crowders presented in Fig.5.4a (green square) shows that the reduction of R_g largely deviates substantially from the simulation results with the implicit depletion potential. R_g monotonically decreases as ϕ increases and at $\phi = 0.3$ it saturates to a globule whereas the implicit potential only makes 7% compaction at the optimal volume fraction ($\phi \approx 0.2$). This qualitative difference between two methods shows the necessity of "explicit" crowding particles in numerical studies.

5.3.4 Critical ϕ of crowders for collapse transition.

A numerical value of the critical volume fraction ϕ can be estimated for a given λ by $x_c = (3/4\pi)^{1/3}\lambda\phi_c^{1/3}$, which gives,

$$\phi_c = \left(\frac{4\pi}{3}\right)\left(\frac{x_c}{\lambda}\right)^3. \tag{5.7}$$

Because an appropriate order parameter for a coil-to-globule transition due to crowding is not ϕ but x, I plotted $R_g(x)$ instead of $R_g(\phi)$ in Fig. 5.5. The figure shows that although the slope at the critical x value is not very sharp due to finite-size
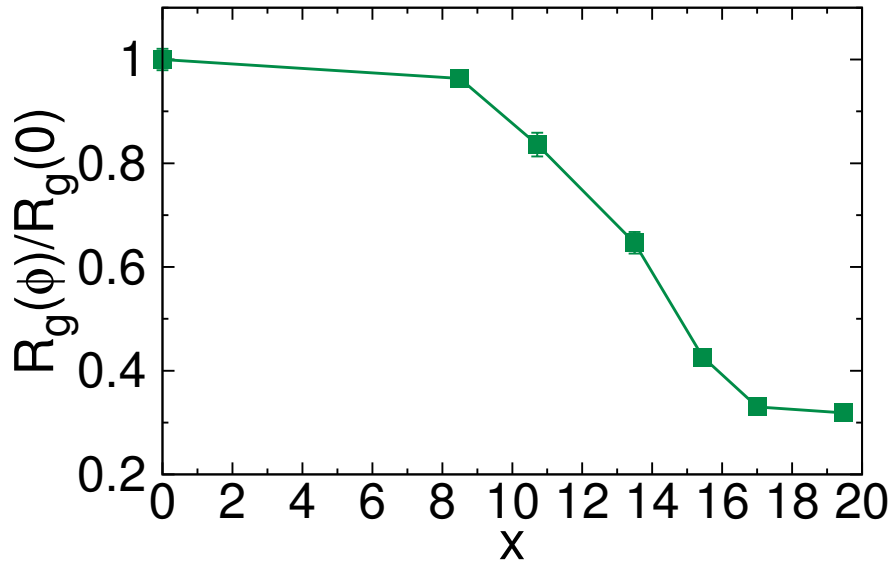
Figure 5.5: R_g of SAW with the same parameters used in Fig. 5.4 as a function of x instead of ϕ. The plot indicates that the coil-to-globule transition of SAW is first order transition rather than second or higher order transitions and the transition occurs at $x \approx 17$.

effects, the coil-to-globule transition of SAW induced by crowding effects is a first order rather than higher order transitions. This result is consistent with the experimental observations reported in ref [100].

Examining the change of R_g and its scaling relation in Fig. 5.4 for $\lambda \approx 47$ (red circle), we can estimate the critical x value is reached when $\phi \approx 0.2$ and $\lambda \approx 47$. The resulting x_c with those parameters is ≈ 17. However, the critical value, $x_c \approx 17$, may vary according to other parameters such as solvent, the length of the polymer chain, and interactions of polymers, and should be used only as a guide to understand

experimental results.

5.3.5 Insights into experiments

5.3.5.1 DNA

For the collapse of T4-DNA [78], with $N \approx 10^8$ and $l_p \approx 50$ nm, $\overline{R}_g(0) \approx$ $l_p(N/147)^{3/5} \approx 1.6 \times 10^5$ nm, and $\sigma_c = 0.0215 \times M_w^{0.583}$ nm for PEG [69], where M_w is the molecular weight of PEG; thus $\lambda \approx 7.3 \times 10^6 \times M_w^{-0.583}$, which leads to $\phi_c \ll 1$ for PEG with almost any M_w for all practical purposes. Therefore, only a small amount of PEG is sufficient to induce a coil-to-globule transition of DNA chain of a genomic size.

5.3.5.2 Intrinsically Disordered Proteins (IDP) and ribozymes

$R_g(0)$ for a typical IDP with $N \approx 100$ is approximately 3nm. The λ for the experiment using IDP and PEG, is given by $\lambda \approx 140 \times M_w^{-0.583}$ where M_w is a molecular weight of PEG. ϕ_c is estimated by

$$\phi_c \approx (4\pi/3) \times (x_c/140)^3 \times M_w^{1.75}. \tag{5.8}$$

Using the proposed value, $x_c = 17$, ϕ_c is greater than 0.4, which is the maximum possible volume fraction in physiological conditions, even with small M_w (10 Da). Therefore, IDPs are not in the proper parameter range to observe the crowding induced collapse of the polymer with the PEG. I predict there is no coil-to-globule transition if we assume that a IDP can be modeled by SAW. This result is in

qualitative accord with experimental results probing crowding effects on five IDPs studied in the two experiments [90, 101].

In the case of RNAs, the λ for the experiment with *azoarcus* group I intron ribozyme and PEG-1000, which is studied by SAXS in ref [76], is ≈ 6. In the experiment, it was shown that $R_g(0)$ for the ribozyme is 7.5nm. Hence, x for the maximum $\phi = 0.4$ is 1.2. Therefore, we predict that there should be no coil-to-globule in this system.

5.4 Summary

In this chapter, I tested the theory for the crowding-induced compaction or the collapse of a self-avoided polymer over wide range of parameters. The formula for the $R_g(\phi)$ proposed based on the scaling arguments is confirmed by low-friction Langevin dynamics simulations using a SAW and "explicit" crowders. The simulation results also show that a polymer undergoes a coil to a globule transition at a critical volume fraction ϕ_c and the critical volume fraction can be estimated from a critical dimensionless parameter $x_c = R_g(0)\phi_c^{1/3}/(4\pi\sigma_c/3) \approx 17$. By comparison with the experimental results, it is shown that $x_c \approx 17$ qualitatively predict the thermodynamic state of the chain with the accuracy.
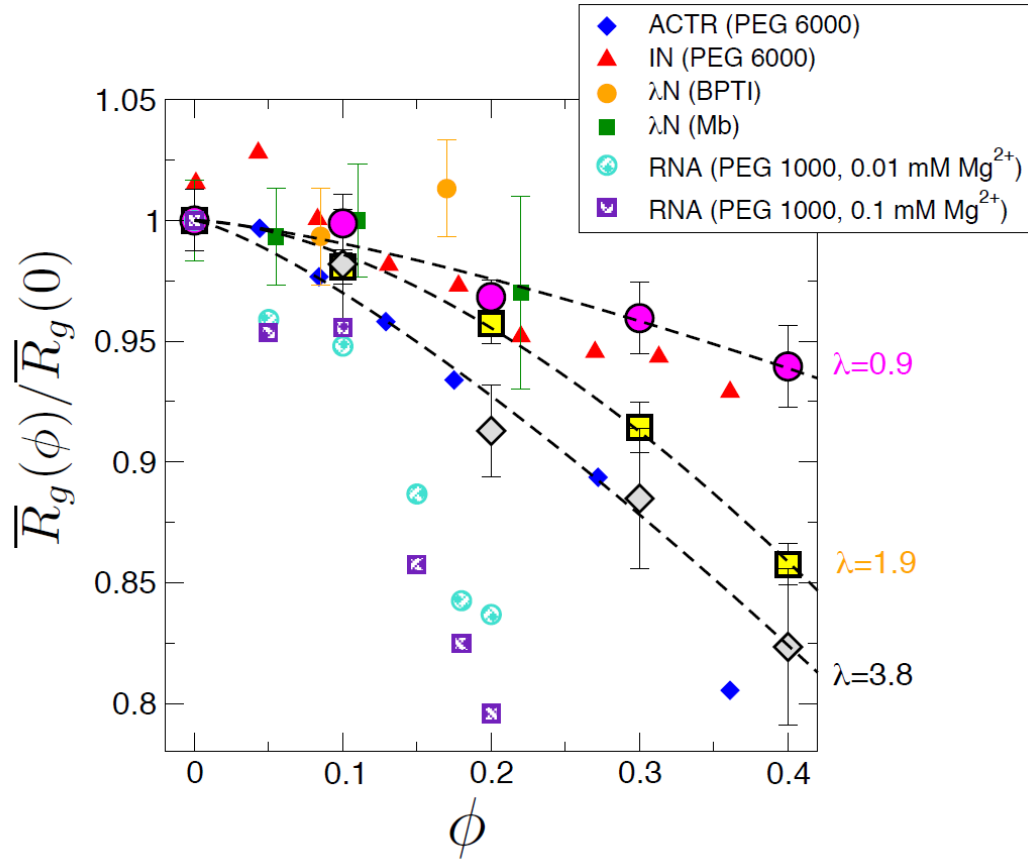
Figure 5.6: Compaction of intrinsically disordered proteins ACTR and IN in an increasing volume fraction of PEG-6000 [90] and λN in BPTI or metmyoglobin (Mb) [101]. ACTR is the activator for thyroid hormones and retinoid receptions. IN is the N-terminal domain of the HIV integrases. Data of PEG-1000 induced compaction of *azoarcus* ribyzyme (RNA) are shown for two different Mg^{2+} ion concentration as well [76]. To compare with the experiments, I superimposed my simulation results using SAW polymer with $N = 100$ and $\lambda = 0.9, 1.9, 3.8$.

Chapter 6: The effects of polydisperse crowdings on the conformation of DNA

6.1 Introduction

The influence of macromolecular crowdings on the thermodynamics and the kinetics of bio-reactions has attracted a great deal of attention because of its profound impacts on cellular functions of biopolymers. For instance, the compaction of DNA in the presence of PEG, which was experimentally shown by Lerman [78], illustrates how the crowding particles can lead the polymer to a global conformational change. Despite a long history of researches on the crowding problems and the recognition of the crowding induced compaction of DNA, the role of crowding effects on DNA is not sufficiently appreciated in computational studies. Because DNA has relatively large persistence length ($\approx$ 50nm), it would be interesting to use more detailed model beyond a SAW simulated in chapter 5 to clarify the crowding effects on DNA more precisely.

In particular, the glass-like properties of a bacterial cytoplasm, which is elucidated by a recent paper [102], drew our attention in the study of the response of DNA on a polydisperse medium. Also, the recent numerical works suggest that

the shapes as well as the sizes of crowders may considerably change the crowding effects on the polymer [87, 88]. Thus, it would be interesting to investigate how the conformations of DNA will be altered by polydisperse macromolecular crowding environments. To answer this question, I performed low-friction Langevin dynamics simulations using a Worm-like-chain (WLC), which is known to be a good model for a relatively stiff biopolymer, and explicit spherical and spherocylindrical crowding particles.

6.2   Methods

6.2.1   Model

I used a semiflexible discrete WLC model, which is known to describe elastic properties of DNA. The discrete WLC is a bead-spring model in which chain connectivity with a fixed bond length is maintained using a large spring constant connecting two consecutive beads. The bending rigidity of the chain was implemented by quadratic bond angle potential. I chose Weeks-Chandler-Anderson (WCA) potential for interactions between monomers, and soft-sphere potential is employed for excluded volume interactions for crowder-crowder and crowder-polymer beads.

6.2.1.1   Soft Spheres (SS)

The energy function for the system consisting of the WLC and soft spherical crowders is,

$$E = E_S + E_B + E_{\text{WCA}} + E_R, \tag{6.1}$$

$$E_S = \sum_{i=1}^{N_m-1} K \frac{(|\vec{r}_{i+1} - \vec{r}_i| - l_0)^2}{l_0^2}, \tag{6.2}$$

$$E_B = \sum_{i=1}^{N_m-1} G\left(\theta_i - \theta_0\right)^2, \tag{6.3}$$

$$E_{\text{WCA}} = \sum_{i,j<N_m} \Theta\left(\frac{\sigma_{ij}}{r_{ij}} - 1\right) \epsilon\left[\left(\frac{\sigma_{ij}}{r_{ij}}\right)^{12} - \left(\frac{\sigma_{ij}}{r_{ij}}\right)^{6}\right], \tag{6.4}$$

$$E_R = \sum_{i<j} \epsilon\left(\frac{\sigma_{ij}}{r_{ij}}\right)^{12}, \sigma_{ij} = \frac{\sigma_i + \sigma_j}{2} \tag{6.5}$$

where $\sigma_{ij} = \frac{\sigma_i + \sigma_j}{2}$, $\Theta(x)$ is a Heaviside step function, N_m is the number of monomers, K ($> 1000 k_B T/l_0^2$) is the spring constant with l_0 being the bond length. The bending rigidity constant is G, σ_i is the diameter of a bead, θ_i is the angle between the monomer bond vectors $(\vec{r}_{i+1} - \vec{r}_i)$ and $(\vec{r}_i - \vec{r}_{i-1})$, and ϵ is Lennard-Jones energy constant controlling the strength of the excluded volume interaction. We chose $N_m = 300$ in our simulations.

6.2.1.2 Crowders as spherocylinders (SC)

I model the spherocylindrical crowder by connecting five spherical crowders allowing for overlap (Fig. 6.1a). Five beads in the anisotropic crowders are connected using E_S and E_B in Eq. (6.2) and (6.3) with very large values for the spring and the bending rigidity constants (K_{sp} and G_{sp}, the analogues of K and G in Eq.

6.2 and Eq. 6.3) in order to maintain the cylindrical shape. I ignore excluded volume interaction among the beads in the cylindrical crowder, which is found to be unnecessary because the crowder remains rigid. By choosing the diameter of the cylinder to be $2.36\sigma_m$, volumes of hard sphere crowders and the spherocylinders are equal ($\frac{1}{6}\pi\sigma_c^3 = \frac{1}{6}\pi\sigma_{cyl}^3 + \frac{\pi\sigma_{cyl}^2}{4} \times 2\sigma_{cyl}$) (Fig. 6.1a).

6.2.1.3 Crowders containing mixture of SS and SC:

As an approximate mimic of the polydisperse nature of the cellular environment, I also considered a system containing spheres and spherocylinders. I chose equimolar mixture containing $N_1 = N_2 = \frac{N}{2}$ spheres and spherocylinders so that the total volume fraction of the crowders is $\phi = N_1 (v_s + v_{sc}) = Nv_s$ became in this study $v_s = v_{sc}$. Thus, in a mixture $\phi_s = \phi_{sc} = \phi/2$ where ϕ_s and ϕ_{sc} are the fractions of volume occupied by SS and SC, respectively.

6.2.1.4 *E. coli* cytoplasm-like mixtures:

To mimic the polydispersity in the *E. coli* cytoplasm, I used the mixture of soft-spheres with the radius of 10.4, 5.2, and 2.6nm, which model ribosomes, large protein complexes and individual proteins, respectively. The volume composition of the mixture is 11%, 11% and 8% for 10.4, 5.2, and 2.6nm particles, respectively. As a result, the total volume fraction of crowding particles is 30%.

6.2.2   Simulation details

In order to obtain adequate sampling of the conformational space of the system, I used low friction Langevin dynamics (LFLD), which is known to enhance the conformational sampling rates. It can be shown rigorously, and has been confirmed in simulations, that the thermodynamic properties of the system do not depend on the choice of the friction coefficient [77, 92].

Initially, a semi-flexible chain was placed in a simulation box without the crowders. I performed the LFLD for 10^7 timesteps to equilibrate the system. The crowding particles were added to generate a sample with $\phi = 0.05$. Higher volume fractions were reached by inserting additional crowding particles to the simulation box. Subsequently, Lennard-Jones interaction annealing was carried out for $\phi \geq 30\%$ in order to improve the speed of equilibration, and to avoid catastrophic crashes during insertion of particles. In particular, at the beginning of annealing, particles were inserted at random positions, and ϵ was decreased to $0.1 k_B T$. After an equilibration run, ϵ was slowly increased by $0.05 k_B T$ until I obtain $\epsilon = 1.67 k_B T$.

I adjusted the size of box according to the chain conformation at a given time to minimize the number of crowders. At every timestep, I checked if the chain is enclosed in the simulation box. If any monomer and the boundary of the box is closer less than three times the average distance between the crowders, I resized the box and added crowding particles to the newly extended empty spaces. As a result of constantly resizing the box (a cuboid with changing dimensions) the number of crowders varies. The volume of the cuboid and the number of crowders are varied

in such a way ϕ is constant. The average number of crowders in our simulations varies from $(4000 - 8000)$ depending on ϕ.

The diameter of the monomer σ_m, $\tau = (m\sigma_m^2/\epsilon)^{1/2}$, and ϵ were chosen as the unit length, the unit time and the unit energy, respectively. The value of σ_m suitable for DNA ≈ 3.18nm. Friction coefficients, ζ_m, for monomers and ζ_c for crowders were set at $\zeta_m = 0.05m\tau^{-1}$ and $\zeta_c = \zeta_m\sigma_c/\sigma_m$ [92, 103] (Table 5.1). The duration of each trajectory ranges from 2×10^7 to 5×10^7 Δt. I generated 25 trajectories to obtain statistical properties. I collected data for analysis after at least 10^6 timesteps of equilibration runs.

Because the simulated system sizes are large, and the simulations had to be carried out for a number of values of ϕ, I used Multiple Layered Neighbor List (MLNL) to enhance the efficiency of simulations described in Appendix B.

6.3 Results

6.3.1 Distribution of end-to-end distance and chain persistence length:

I calculated the end-to-end distance distribution, $P(r)$, in the absence of crowders to obtain the persistence length, l_p. By fitting the simulated $P(r)$ at $\phi = 0$ to analytic expression for WLC,

$$P(r) = \frac{16\pi^{-1/2}c^{3/2}e^c}{4 + 12c^{-1} + 15c^{-2}} \frac{r^2}{(1 - r^2)^{9/2}} e^{\left[-\frac{3}{4}t\frac{1}{(1-r^2)}\right]} \tag{6.6}$$

with $r = R/L$, $t = L/l_p$ and $c = \frac{3}{4}t$ where $L = (N_m - 1)\sigma_m$ is the contour length, R is the end-to-end distance, I extracted l_p, the persistence length of the chain

92

[104]. From the excellent fit at $\phi = 0$ I obtain $l_p = (15.4 \pm 0.08)\,\sigma_m \approx 49$nm using

$\sigma_m \approx 3.18$nm (Fig. 6.2a). Because $l_p/\sigma_m > 1$, I expect that the shape of the

chain in the presence of crowding particles is determined by an interplay of bending

rigidity and attractive depletion interaction due to crowders. The results of explicit

simulations, described below, substantiate this expectation.

6.3.2 Dependence of R_g on ϕ for monodisperse crowders

First, I present the results for monodisperse crowding environments consisting

of pure spherical or cylindrical crowders. Snapshots of typical conformations of the

chain and crowding particles are shown in Fig. 1b for different values of ϕs. The

radius of gyration of the chain, R_g, is computed using,

$$R_g\,(\phi) = \left\langle \frac{1}{2N^2} \sum_{i,j} r_{ij}^2 \right\rangle^{\frac{1}{2}} \tag{6.7}$$

where r_{ij} is the distance between monomer segment i and j, and $\langle \cdots \rangle$ indicates an

ensemble average. The dependence of $R_g\,(\phi)$ on ϕ for spherical and spherocylindri-

cal crowders shows substantial differences. For spherical crowders ($dR_g/d\phi \approx 0$ as

$\phi \to 0$) compaction occur only when ϕ exceeds ≈ 0.1. In contrast, for anisotropic

crowding agents ($dR_g/d\phi < 0$), $R_g\,(\phi)$ decreases monotonically for $\phi \leq 0.3$. Crowd-

ing particles lead to the compaction of the chain because of depletion interaction (or

Asakura-Oosawa (AO) interaction), which induces an effective interaction between

monomers. The strength of the AO interaction rougly given by ϕ/σ_c^2 has to exceed

the energy required to bend on scale l_p ($\sim \frac{1}{2}\left(\frac{L}{l_p}\right) k_B T$). For small ϕ it is unlikely

that the AO interaction can compete for the bending penalty. Then, we expect little change in $R_g(\phi)$ for small ϕ for spherical crowders. The strength of the AO interaction for spherocylinder is $\approx \phi P \sigma_c / \sigma_{cyl}^2$ where P is the cylinder length. For our parameters the strength of the attractive AO interaction even at low ϕ exceed the penalty for bending the chain on scale $\sim l_p$. Consequently, $R_g(\phi)$ decreases monotonically till $\phi \approx 0.3$.

For $\phi \leq 0.3$, $R_g(\phi)$ in the presence of spherocylindrical crowders is substantially lower than in spherical crowding particles. For example, at $\phi = 0.2$, $R_g(0.2)$ decreases by 4% relative to $R_g(0)$ in spherical crowders whereas $R_g(0.2)$ decreases by 17% in spherocylinder crowders. Because volume of the chain $\sim R_g^3(\phi)$ the extent of compaction induced by anisotropic particles is substantial compared with spheres. In both cases, compaction occurs due to the AO depletion interaction leading with an effective short range (on length scale $\sim \sigma_m$) attraction between monomers.

The strong effect of compaction of the WLC chain induced by spherocylindrical crowders relative to spherical crowders can be understood by comparing the volume excluded to the polymer by the crowders. Using ideas rooted in scaled particle theory, we can estimate the entropy cost of inserting a hard sphere of dimension σ_{HS} in a box containing hard fluid particles. The entropy difference for inserting the hard sphere of diameter σ_{HS} is related to $C(\sigma)$,

$$c(\sigma_{HS}) = \frac{V_{\text{cyl}}}{V_{\text{sph}}} = \frac{\frac{3}{2}\left[(\sigma_{HS} + \sigma_{\text{cyl}})^2 P + (\sigma_{HS} + \sigma_{\text{cyl}})^3\right]}{(\sigma_{HS} + \sigma_{\text{sph}})^3} \tag{6.8}$$

where V_{cyl} (V_{sph}) is the volume excluded by rod-like (spherical) crowders; P is the

length of the rod. For the parameters listed in Table 5.1, I find that $V_{cyl} > V_{sph}$ predicted $\sigma_{HS} \approx R_g > \sigma_{cyl}$ or σ_c. The entropic cost of inserting a spherical particle of size R_g into a fluid of cylindrical crowders exceeds that for inserting it into a system consisting of spherical crowders. By achieving greater compaction of the WLC in spherocylindrical crowders, the entropy difference is minimized, thus, explaining the results in Fig. 6.1b.

6.3.3 Local nematic order and increase in R_g

Interestingly, as ϕ exceeds 0.2 $R_g(\phi)$ increases in spherocylindrical crowders (Fig. 6.1b). The increase is also reflected in $P(R_g)$, which appears to acquire additional peak at $R_g(0.4) \approx 37\sigma_m$. I attribute the increase to plausible development of local nematic ordering for spherocylinders at $\phi > 0.3$. It is well known that at sufficiently high ϕ, the fluid particles consisting of spherocylinders undergo an isotropic to nematic phase transition if ϕ exceeds a critical value $\phi_{I\rightarrow N}$ [33, 105]. I calculated the liquid crystal order parameter, $\langle P_2(\cos\theta)\rangle$ where θ is the angle between the long axes of two spherocylinders, and $P_2(x) = \frac{1}{2}(3x^2 - 1)$ is the second order Legendre polynomial. The global order parameter $\langle P_2(\cos\theta)\rangle$ is almost zero (< 0.05) for all ϕ, which means that even the highest $\phi(= 0.4)$ is less than $\phi_{I\rightarrow N}$. However, locally the crowders can adopt nematic-like state. To ascertain if this is the case, I calculated $P_2(r) = \langle\sum_{i,j} P_2(\cos\theta_{ij})\delta(|\vec{r}_i - \vec{r}_j| - r)\rangle$ as a function of distance, r. Fig. 6.2d shows that the angular correlation of cylinders becomes stronger as ϕ increases at short distances.

To quantify the extent of "local" nematic ordering, I calculated $Q_2(r) = N_P^{-1} \int_0^r P_2(r') \, d\vec{r'}$ (Fig. 6.2d) where N_P is the number of pairs separated by r. At $r = 2.3\sigma_m$, $Q_2(r = 2.3\sigma_m)$ which is the distance where the pair correlation has first peak for $\phi = 0.4$ (Fig. 6.2d), significantly increases from 0.02 to 0.16 as ϕ increases from 0.1 to 0.4. When we estimate $Q_2(r)$ for the crowders closer than $2.3\sigma_m$ to any monomer of the chain, $Q_2(r) \approx 0.23$. The local nematic ordering of cylindrical crowders is reinforced in the vicinity of the chain. This result implies that relatively stiff chain induces the ordering of cylindrical crowders along the polymer axis, and strengthens the anisotropic interaction of rod-like particles. Thus, at high $\phi(< \phi_c)$ the chain may be thought of as being in a local nematic field (in a mean-field sense), which elongates the polymer along the local direction of the nematic field. Consequently, $R_g(0.4)$ increases above its value at $\phi = 0.2$. I predict further significant increase in $R_g(\phi)$ showed as $\phi \to \phi_c$.

The enhancement in R_g for $\phi \leq 0.3$ can also be correlated with shape changes. The shape anisotropy can be characterized by the aspherocity parameter (Δ) and a shape parameter (S). Both Δ and S are defined in chapter 5.

I calculated $\Delta(\phi)$ and $S(\phi)$ as a function of crowder characteristics. For spherical crowders, $\Delta(\phi)$ and $S(\phi)$, decreases with increasing ϕ, implying that the WLC becomes more spherical with increasing compaction. In contrast, there is a sharp increase in $\Delta(\phi)$ and $S(\phi)$ as the volume fraction of the spherocylindrical crowders increases beyond $\phi \approx 0.2$. The value of $\Delta(0.4) \approx \Delta(0)$ and $S(0.4) \approx S(0)$, which shows that at both $\phi = 0$ and high ϕ the WLC chain is an anisotropic ellipsoid ($S > 0$). The elongation of the chain along the local nematic axis results in an

increase in $R_g(\phi)$ when $\phi > 0.2$.

6.3.4 Mixture of spheres and spherocylinders

The dependence of $R_g(\phi)$ on ϕ of the WLC in the presence of both SS and SC crowders are shown in Fig. 6.3a. The mixture has a profound effect on the size of WLC compared to the monodisperse case. The value of $R_g(0.4)$ decreases by over 40% compared to $R_g(0)$, whereas the maximum compaction in monodisperse SC at $\phi = 0.4$ is only 10%. For comparison, I also show, at $\phi = 0.2$ and $\phi = 0.4$, the expected result for $R_g^A(\phi) = \frac{1}{2}\left[R_g^{SS}\left(\frac{\phi}{2}\right) + R_g^{SC}\left(\frac{\phi}{2}\right)\right]$ obtained using the assumption that the effect of crowders is additive. Remarkably, $R_g(\phi)$ is significantly lower than $R_g^A(\phi)$ indicating that the mixture restricts the volume available to the WLC to a much greater extent than the individual components do.

The surprising effect of significant compaction in the mixture can be qualitatively explained using the notion of depletion potentials for mixture of SS and SC [106]. Consider the interaction between two spherical interaction sites in the presence of rods. If a SC particle is trapped between these sites then the rod loses translational entropy as well as rotational entropy because of restriction in the orientation. The large unfavorable entropy loss results in the depletion of the SC from the gap between the spherical interaction sites. The result is that there would be an excess osmotic pressure due to the AO attraction that pushes the SS and the monomers together. Two consequences of the entropy-driven depletion interactions are : (i) Due to the attractive interactions, the SS particles would be more closely

packed than in the absence of the SC. Indeed, in the limit of $\sigma_{cyl} < P < \sigma_c$, it has been experimentally shown that the addition of a small fraction (by volume) of the SC can lead to crystallization of low density suspension of hard spheres. (ii) We also expect that as a consequence the excess volume available to the WLC should be greatly reduced compared to the monodisperse crowders. Such a confined space the WLC should be considerably more compact than in the presence of monodisperse crowders at the same ϕ.

The expected enhancement in the packing of the SS due to the SC is clearly evident in the pair function $g(r)$. The results for $\phi = 0.2$ and $\phi = 0.4$ show that both of radial distribution functions, $g_{SC-SC}^{Mix}(r)$, between interaction sites of the SC and $g_{SS-SC}^{Mix}(r)$, between the SC and the SS, do not exhibit significant structure. In sharp contrast, $g_{SS-SS}^{Mix}(r)$ has the structure corresponding to a high density liquid (especially at $\phi = 0.4$), which is remarkable considering that at $\phi/2$ (corresponding to the fraction of volume occupied by SS) $g_{SS-SS}^{SS}(r)$ is essentially featureless.

The much stronger depletion force due to SC results in a considerable reduction in the volume accessible to the chain, which explains the dramatic reduction of $R_g(\phi)$. The WLC at $\phi = 0.4$ is surrounded by spheres as assessed from the $g_{M-SS}(r)$ and $g_{M-SC}(r)$ where $g_{M-SS}(r)$ $(g_{M-SC}(r))$ is the radial distribution function between the monomer and the SS (monomer and the SC). The number of SS near the chain calculated using $N_{SS} = 4\pi \left(\frac{N_0}{V}\right) \int_0^{r_{min}} r^2 g_{M-SC}(r) \, dr$ where r_{min} is the minimum in the $g_{M-SS}(r)$ at $\phi = 0.4$ is 11.4. A similar calculation for SC gives $N_{SC} = 4.7$.

6.3.5   Mixture of spheres with the *E. coli* cytoplasm-like composition

Strikingly, the crowding effects were qualitatively changed in the mixture of polydisperse soft-spheres. I investigated the R_g of WLC in the polydisperse mixture of soft spheres described in section 6.2.1.4 and found that the WLC was swollen by crowding particles. The R_g of the WLC presented in Fig. 6.4a shows about 40% increase from $R_g(0)$. The resulting R_g corresponds to the R_g for the WLC with the persistence length of 122nm, which is about 2.5 times a bare persistence length (≈ 50nm). The ensemble of the chain conformations confirms the expansion of the WLC by crowdings (Fig. 6.4b). In order to find the origin of the swelling of the chain, I calculated radial distribution functions of the crowding particles. Fig. 6.4c shows that the pair correlations for the largest crowders and the monomers increases at the distance where the monomer and the largest crowder are in contact with each other in the presence of small crowders. This result indicates that the large crowders are located closer to the monomers and may act like the confinement on a segment of the polymer. The expansion of the chain conformation under the one- or two-dimensional confinements was established several decades ago [107]. The pair functions between the largest crowders demonstrate that the large crowders aggregate due to the depletion potential generated by smaller crowders and behave as larger complexes, as a result, the slit-like confinement will be enhanced (Fig. 6.4d).

6.4 Summary

I examined the crowding effects of various crowding environments on the WLC in the context of the conformational changes of DNA *in vivo*. I found that the crowding effects of SC is much larger than spherical crowders at low volume fractions and the large enhancement of crowding effects of SC disappears at high volume fraction due to local nematic ordering of rod-like particles. Remarkably, the mixture of SC ans SS exhibits "cooperative" crowding effects, which means the crowding effects of the mixture is greater than the sum of the influence of single component systems. Finally, the polydisperse *E. coli* cytoplasm-like environment is simulated by the mixture of soft-spheres. Interestingly, the simulation results show the expansion of the WLC in such a macromolecular crowding envrionment. The radial distribution functions reveal that the reason for the expansion of the chain is the confinement-like effects of large crowders reinforced by small crowders.
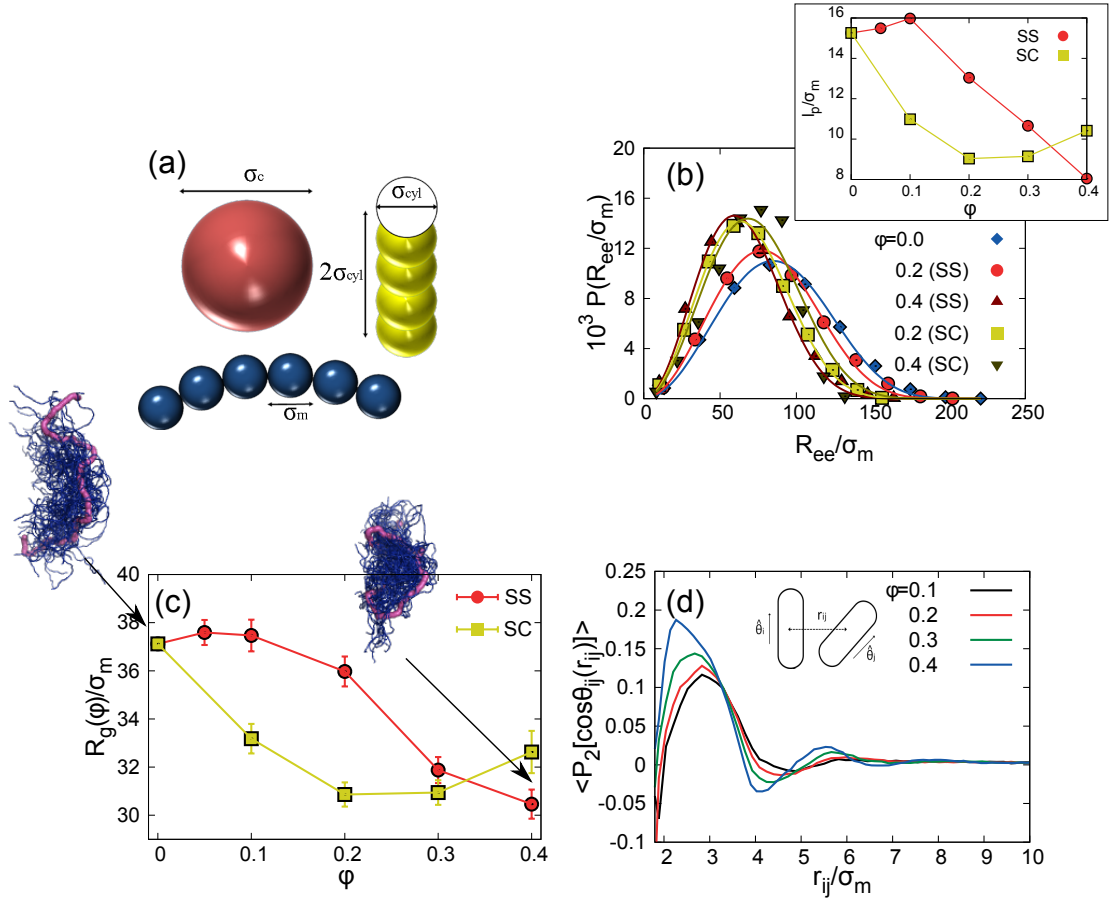
Figure 6.1: Crowding effects of soft-spheres on WLC. (a) Coarse-grained models of spherical crowder (red), spherocylinderical crowder (yellow) and WLC chain (blue) with their dimensions. (b) End-to-end distribution function of WLC chain at two different volume fractions (ϕ=0.2,0.4) of spherical (SS) and spherocylindrical crowders (SC). The inset shows the persistence length (lp) of the polymer as a function of volume fraction of SS and SC. (c) The gyration radius (Rg) of the polymer with varying volume fraction of SS and SC. (d) Liquid crystal order parameter for spherocylindrical crowders, averaged over the ensemble of crowder particles, as a function of distance.
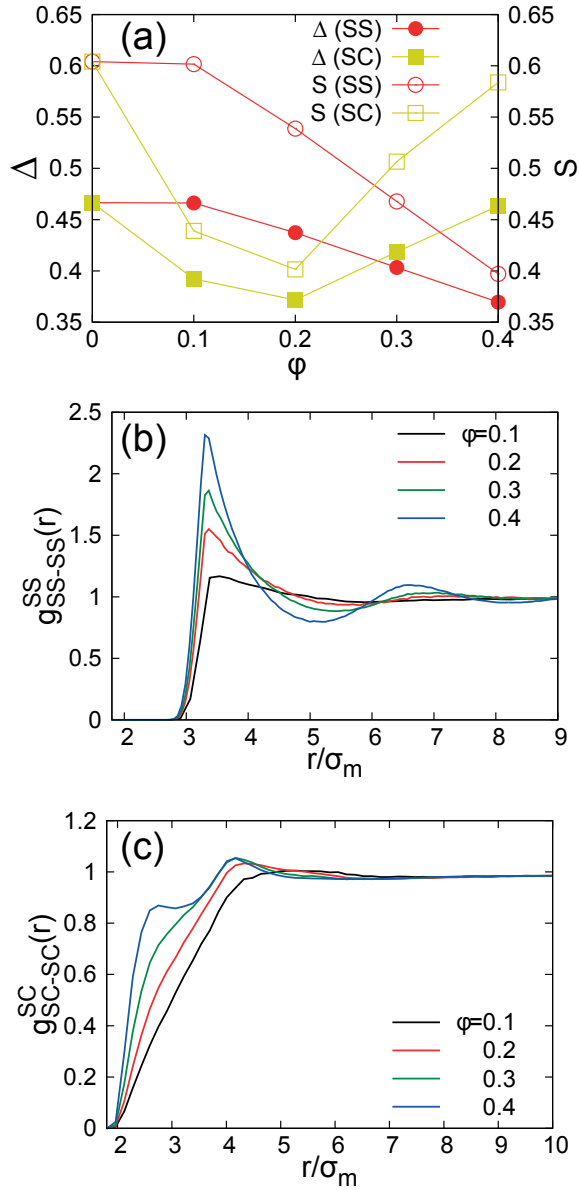
Figure 6.2: Crowding effects of SC on WLC. (a) Asphericity (Δ) and shape parameter (S) of WLC chain as a function of SS and SC volume fraction. Radial distribution functions calculated at varying volume fraction for (b) spherical crowders and for (c) spherocylindrical crowders.
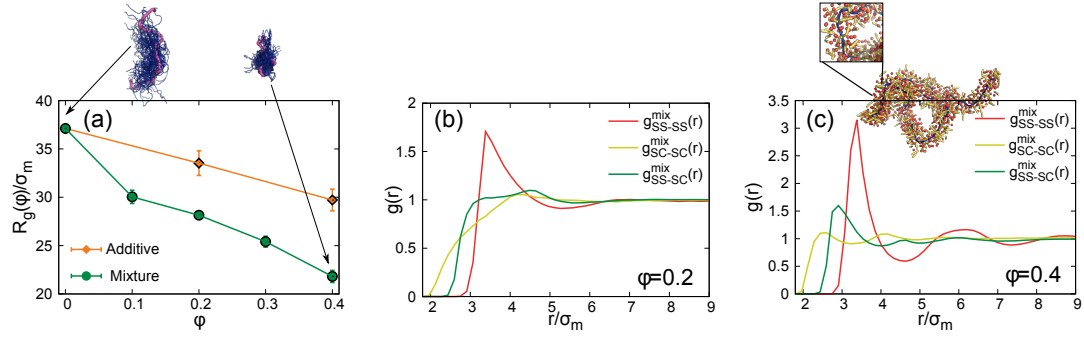
Figure 6.3: Crowding effects of the mixture of SS and SC on WLC. (a) The gyration radius of WLC chain as a function of volume fraction of 1:1 SS and SC mixture (green). The orange line is for Rg values calculated by assuming that the effect of compaction due to SS and SC crowders are additive. (b) Radial distribution functions calculated for SS-SS, SC-SC, and SS-SC pairs at $\phi= 0.2$. (c) The same calculation was done at $\phi = 0.4$. Distribution of SS and SC crowders, especially densely packed configuration of SS crowders, around WLC chain are visualized using a snapshot from Langevin dynamics simulations.
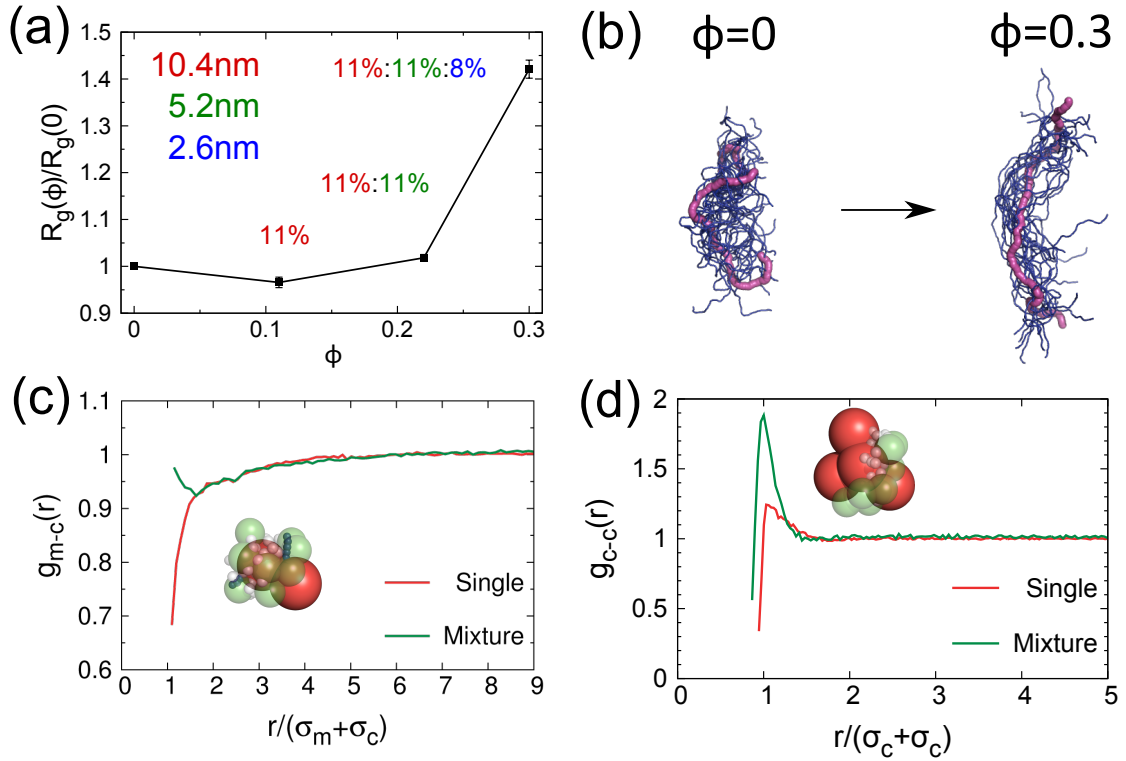
Figure 6.4: Crowding effects of polydisperse SS on the WLC. (a) R_g for $\phi = 0.11$, 0.22 and 0.3. At $\phi = 0.11$, Only 10.4nm particles are used. At $\phi = 0.22$ both 10.4nm and 5.2nm present in the system with the same volume fraction of 11% for each. At $\phi = 0.3$, the system consists of 10.4nm, 5.2nm and 2.6nm sized crowders with 0.11:0.11:0.08 volume fraction. (b) Ensemble of the WLC at $\phi = 0$ and 0.3. The ensemble visually confirms the chain is extended by crowding. (c) Radial distribution function of large crowders from a monomer in monodisperse (red) and polydisperse crowding envrionments (green). (d) Pair correlation functions of large crowders in monodisperse (red) and polydisperse crowding envrionments (green).

Chapter 7:   Concluding remarks and future perspectives

In this thesis, I demonstrated that 1) the thermodynamic theories for glasses such as MCT and RFOT theory, which covers the relaxation behavior over a broad range of temperatures, can quantitatively explain the interesting charateristics of glasses, which are found in colloidal suspensions as well as molecular glass formers, and 2) the macromolecular crowding effects of such a glass-like polydisperse medium, which reflects *in vivo* conditions in a cytoplasm, can significantly impact on thermodynamic states of various biopolymers.

Despite my efforts on these matters, certainly, there are many issues that I have not addressed in this thesis. One notable example is the influence of hydrodynamic interactions (HI) between molecules via solvent molecues. There are numorous studies asserting that the hydrodynamic interaction can significantly change the dynamics of colloids and biopolymers [108–110]. However, despite recent technical advances and development of efficient algorithms, because of tremendous increases in the computational complexities, it is still formidable to apply the HI to large systems studied here. Although there are some predictions arguing that the thermodynamics of the colloidal glasses would not depend on microscopic details of dynamic behavior [2], it is important to elucidate the possible connection of dy-

namic facilitation by HI to the interesting features of the glasses using convinicing numerical calculations.

The role of polydispersity in the crystalization and the vitrification is another challenging issue. As shown in chapter 3, the critical behavior of Bond orientational order observed in weakly frustrated system is absent in more strongly frustrated binary mixture of colloidal system. Thus, we can ascribe the formation of glasses to the hinderance of the crystalization due to the increase in compensating state entropy generated by polydispersity rather than any specific structural order parameters. The numerical investigations using materials with various polydispersity would help us to clarify this problem.

Regarding maromolecular crowding, the combination of crowding effects and confinement is also an intersting topic because most of bio-reactions occur in confined spaces surrounded by membranes, which enable a crowded condition. Some numerical calculations and experimental observations reveal that the confinements play an important role in the conformations of biomolecules [111–114]. In particular, the interplay of confinements and crowdings would provide us with more profound understanding of the many interesting thermodynamic and kinetic properties of bacterial and eukaryotic chromosomes such as bacterial chromosome segregations [115] and fractal structure of eukaryotic chromosomes [116]. I hope my works presented here can shed light on future studies of these physically and biologically relevant complex systems.

Appendix A: Dependencies of structural relaxation on microscopic dynamics and ensembles

In contrast to molecular glass formers where short-time dynamics of molecules are governed by Newton's equation of motion, the dynamics of colloidal particles are described by Brownian dynamics equation of motion because the movements of colloidal particles are driven by collisons with water molecules. Thus, inertial effects are negilible for suspension of colloidal particles in high viscosity solvent. These major differences in the dynamics precipitate examining the role of different dynamics on glass forming materials. It is, of course, expected that if Newtonian dynamics is performed for large samples for long times then they shall be equivalent to Brownian dynamics. However, several studies [2] suggest that the structural relaxation are not affected by microscopic short-time dynamics of particles, and the slowing down of dynamics is controlled by a universal mechanism that is not influenced by microscopic details of dynamics in the so-called MCT regime ($\phi < \phi_A$ in the Wigner glass, for example).

Nevertheless, the answer is still not conclusive. One of important limitations of the previous studies [117–119] is that the temperatures explorered are far from glass transition temperatures and are even much higher than the dynamic transition

temperatures or lower than the corresponding dynamic transition density. Hence, the responses of the system to microscopic details are still unknown in the regime, $\phi > \phi_A$, and the investigation of how the short-time microscopic dynamics and thermodynamic ensembles is related to the long time relaxation above the dynamic transition points would be very interesting. To answer this question, first I present a brief review of literature regarding this problem and discuss dynamic simulations performed by integrating Newtonian and Brownian equation of motion that correspond to ballistic and diffusive microscopic dynamics, respectively.

A.1 Literature review

The effects of microscopic dynamics on the structural relaxation of supercooled liquids were first explored by Löwen, Hansen, and Roux [117] a couple of decades ago. In their works, colloidal suspensions consisting of polydisperse highly charged particles interacting via purely repulsive screened coulomb potential were simulated using Newtonian (ND) and Brownian dynamics (BD). By comparing BD with ND results they concluded that there are qualitative differences in the relaxation dynamics between ND and BD in that the dynamic scattering function in BD does not show fast and β-relaxations and a plateau corresponding to a structural arrest. Fast relaxation also disappears in BD simulations. Another important conclusion is that the long time relaxation seems to be governed by hopping processes in BD as well as in ND. This implies that although the dynamics of the system are significantly different in the short and intermediate time domains, the long time dynamics

would be controlled by universal relaxation mechanism regardless of the underlying microscopic dynamics.

Subsequently, Gleim et al extended these systems to analogue of structural glass formers using 8:2 LJ mixture, the so called Kob-Anderson (KA) mixture [118]. Their findings confirmed that the general structure of the α-relaxation in the KA mixtures is not affected by microscopic dynamics, at least, above MCT temperature, T_{MCT}. The qualitative similarity of ND and BD results, and the relevance to MCT shown in colloids and KA mixture were substantiated in other glass forming systems on several subsequent papers [119–121]. These are celebrated results for MCT because the basic structure of long time relaxations should not be dependent on the details of dynamics at least within the MCT framework.

On the other hand, Berthier et al [25] discussed the dependence of four-point correlation, G_4, and susceptibility, χ_4, on microscopic dynamics within the MCT framework. They claimed that, in contrast to the long time relaxation, the quantities such as G_4 and χ_4, reflexted to fluctuations, seem to be strongly dependent on microscopic dynamics as well as statistical ensembles. They tested their predictions using KA mixtures and Beest-Kramer-van Santen model for silica, which is known as a strong glass former, and confirmed their theoretical predictions. Moreover, they argued that although G_4 and χ_4 apparently depend on microscopic dynamics. These fluctuation-related quantites are directly connected to a universal dynamic length scale that is not affected by microscopic dynamics. Only the relation between the dynamic length scale and the relaxation time is changed. This quite strong argument, however, has not been established in various systems.

These studies remind us that it is still an open question whether microscopic dynamics and ensembles will change the fundamental physics of LGT or not. In addition, in previous studies, the temperatures were above $T_{MCT} \approx T_A$ and much greater than T_K because of limited computational resources. Therefore, it might be interesting if we can investigate the dependence of the relaxations and the fluctuations on microscopic dynamics above and below T_A or ϕ_A for various glass forming model systems. With these considerations, I performed additional simulations for highly charged colloidal suspension illustrated in chapter 2 with ND and compare the results with the BD results.

A.2   Method

I used the same Hamiltonian and parameters used for highly charged colloidal particles shown in Eq. 2.1 and Table 2.1 of chapter 2. I integrated Newtonian equation of motion, instead of Brownian equation of motion with time step, $\Delta t \approx 0.1\sqrt{\frac{m\sigma_1^2}{kT}}$ using the Velocity-Verlet algorithm [122]. With these values, I was able to acheive energy conservation within $0.0001kT$ during constant energy simulations. For comparison, the simulations were performed at constant temperatures (NVT) as well as constant energy (NVE). To fix the temperature, I adopted the velocity rescaling scheme in which the velocities of particles were rescaled at every 10 time steps as,

$$\vec{v} = \vec{v}_0\sqrt{\frac{T_0}{T}} \tag{A.1}$$
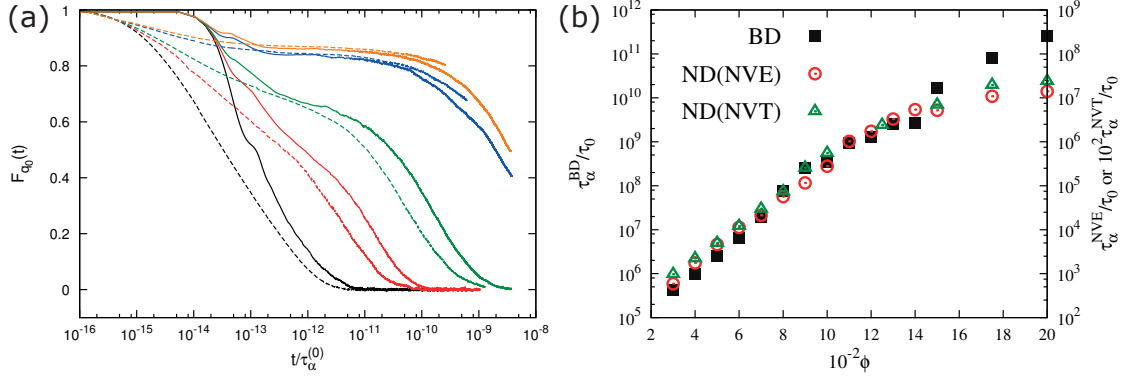
Figure A.1: (a) The dynamic scattering function, $F_q(t)$ estimated at $q = q_{max}$ for Brownian dynamics with NVT ensemble and Newtonian dynamics with NVE ensemble. (b) α-relaxation time, τ_α, obtained from fits of $F_q(t)$ to stretched exponential $\sim \exp\left[-(t/\tau_\alpha)^\beta\right]$

where T_0 is desired temperature and T is the effective temperature of the system estimated by $N^{-1} \sum_{i=1}^{N} \frac{m_i \vec{v}_{i1}^2}{3}$.

A.3   Results and discussion

First, I confirmed Löwen et al's and Gleim et al's results. As reported by Löwen et al, $F_q(t)$ shows fast and β-relaxation, both of which are absent in BD results (Fig. A.1a) but the basic structure of α-relaxation is not affected by microscopic dynamics for $\phi < \phi_A$ (Fig. A.1b). In other words, the critical volume fraction, ϕ_A, and the MCT exponent, γ, of ND were identical regardless of microscopic dynamics and ensembles. Furthermore, the dependence of τ_α on ϕ also seems not to be
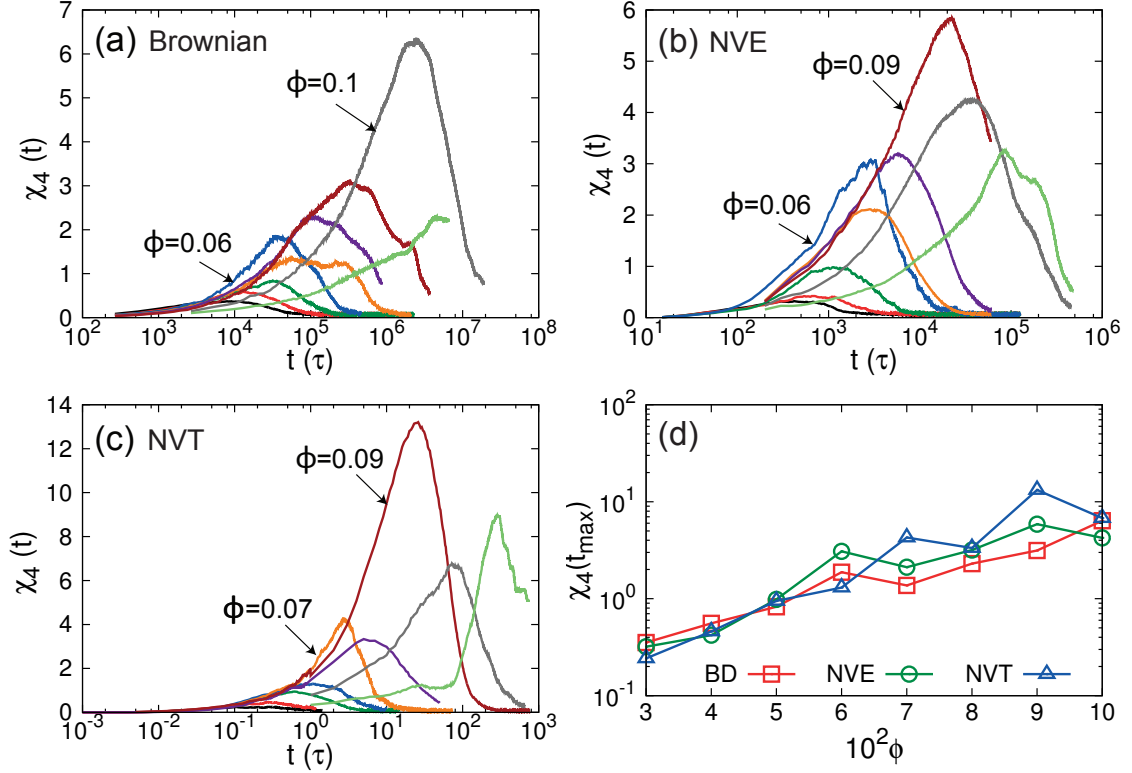
Figure A.2: 4-point susceptibility, $\chi_4(t)$, as a function of time for Brownian dynamics (BD) (a), NVE (b) and NVT ensemble (c) with Newtonian dynamics. The time is scaled by the unit time, $\tau = (\sigma_1^2/D_1)$ for BD, $\tau = (m_1\sigma_1^2/k_BT)^{1/2}$ for NVE and NVT. The volume fractions ϕ presented here are from 0.03 to 0.1 with 0.01 increment and 0.125 from left to right.

altered by statistical ensemble (ie, NVE or NVT) as well as microscopic dynamics for $\phi < \phi_A \approx 0.11$. Thus, it seems that the relaxation of colloidal suspensions in MCT regime ($\phi < \phi_A$) may be dominated by somewhat universal mechanism, which is well described by MCT.

However, the universality of α-relaxation no longer holds for $\phi > \phi_A$. Fig. A.1b clearly shows the steeper increase of τ_α using BD than ND upon compressing. On the other hand, no significant difference between NVE and NVT ensembles is observed except for changes in prefactors. These results imply that 1) the mechanism governing the longest relaxation is switched from MCT to activated transport at the transition volume fraction ϕ_A as predicted by RFOT, and 2) unlike MCT regime, in activated transport regime ($\phi > \phi_A$), microscopic dynamics (BD or ND) may affect the longest relaxation of the system.

In addition, in order to ascertain that the relatively small increase of τ_α^{ND} to τ_α^{BD} upon increasing ϕ is not due to finite size effect, I performed the simulations with 10^3, 2×10^3 and 4×10^3 particles instead of 10^4 and found no significant difference according to the size of the system. Therefore, the deviation of τ_α is the influence of microscopic dynamics rather than finite size effect.

The influences of microscopic dynamics and ensembles are more prominent in the dynamic fluctuations. The comparison of $\chi_4(t)$ in BD, NVE and NVT reveals that the fluctuations of dynamics are affected by micrscopic details in that the peak of $\chi_4(t)$ is maximized at $\phi \approx 0.1$ with BD whereas it is maximized at $\phi \approx 0.09$ with NVE and NVT. Furthermore, the peak heights are also changed by microscopic dynamics and, in particular, $\chi_4(t = \tau_\alpha)$ in NVT is about two times higher than ones

113

in NVE and BD (Fig. A.1d). More systematically, I fit $\chi_4\left(\tau_\alpha\right)$ to $\sim \tau_\alpha^\lambda$ and obtained $\lambda = 0.73$ and 0.77 for NVT and NVE, respectively, whereas $\lambda = 0.46$ for BD. These observations are consistent with the predictions from MCT and the numerical confirmations with KA mixture and the BKS considered by Berthier et al [25], suggesting that the dynamic fluctuations would diverge more strongly in NVT than in BD and the divergence in NVE would be similar as in NVT. Also, for $t < \tau_\alpha$, $\chi_4\left(t\right)$ is well fit to $\sim t^\mu$ with $\mu = 0.6$ for all sets of simulations. This universal exponent reconfirm the validity of MCT for Wigner glasses because other scenarios such as collectively rearranging regions, freely diffusing defects and kinetically constrained model predict $\mu \geq 1$ or logarithmic increase [26].

A.4 Summary

In this appendix, I examined the influences of microscopic dynamics and ensembles on the dynamics of Wigner glasses using MD simulations. Although the average dynamics of the glasses is independent of microscopic details and ensembles for $\phi < \phi_A$, the relaxation dynamics beyond the dynamic transition point ϕ_A as well as the fluctuations seems to be affected by the nature of short-time dynamics and ensembles. In addition, the anlysis of $\chi_4\left(t\right)$ confirms that MCT is the only theory that can explain the dynamic fluctuations in Wigner glasses properly in $\phi < \phi_A$, and further theoretical development would be needed to describe $\phi > \phi_A$ regime.

Appendix B: Crowding simulation details

Multiple layered neighbor list: The large system size needed to reliably simulate the WLC chain in the presence of explicit crowders is computationally demanding. Thus, it is important to develop a computer code that minimizes the number of operations to compute interaction potential. In order to acheive this goal, at least in part, we devised and implemented multiple layered neighbor list (MLNL) technique to reduce computational cost. To our knowledge, this methodology has not been used in previous simulations. In conventional Verlet algorithm, the list of neighbors, which are the particles located within a cut-off distance, R_c, is created for each particle at the beginning of the simulation. When pair-interaction is needed, we search only the neighbors instead of computing interactions between all pairs of particles. Thus, the computational cost decreases as R_c gets smaller. However, since the positions of particles are constantly evolving, we have to update the neighbor list with a certain frequency. In conventional Verlet list, all neighbor lists are updated whenever the maximum displacement of any particle exceeds R_c. The frequency of updates increases as R_c becomes smaller, thus increasing the computational costs for updating the neighbor list. The two competing demands (frequent update for small R_c and infrequent update for computation larger number of interaction pairs)
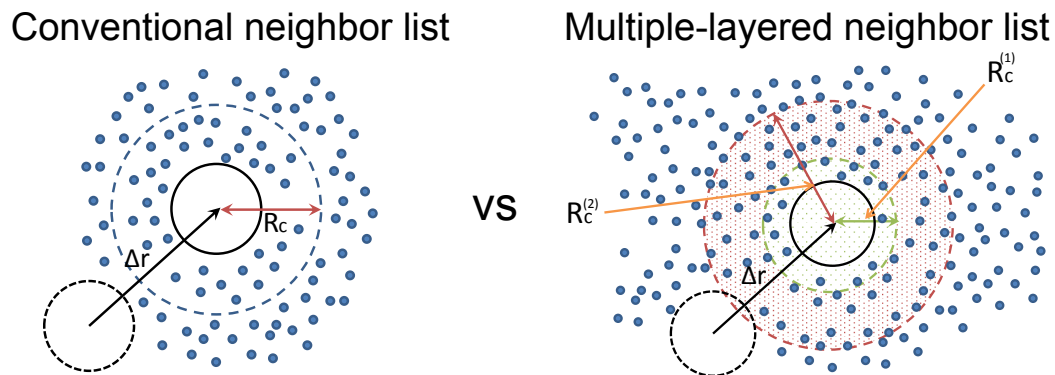
Figure B.1: Schematic descriptions of conventional (left) and multiple-layered neighbor list (right) algorithm. In conventional algorithm, when an neighbor list is updated, all pair distanced of particles in the system should be calculated to ascertain if the particle is located within the distance R_c or not. As a result, the computational cost for the update is proportional to N^2 where N is the size of the system. In contrast, in multiple-layered neighbor lists, the test is only performed among the neighbors in a upper layer neighbor list (red circle) that has larger R_c. This procedure can reduce significant amount of calculations when N is large.

requires an optimal value of R_c.

MLNL is designed to reduce the computational costs for calculating interaction potentials and updating neighbor lists by using multiple numbers of neighbor lists. It consists of several neighbor lists each with a different cut-off distances, $R_c^{(1)} < R_c^{(2)} \cdots < R_c^{(n)}$. Interaction potentials are only calculated using the upper-most layer, which has the smallest $R_c = R_c^{(1)}$. This allows us to minimize the cost of calculating interaction potentials. When the maximum displacement of a particle exceeds $R_c^{(1)}$, instead of calculating the distance between all pairs of particles as in the conventional algorithms, we update the upper-most neighbor list using the neighbor list with $R_c^{(2)}$. Thus, the requirement of computing $O(N^2)$ interactions is avoided to a large extent by using this technique. The disadvantage of the MLNL is that memory requirement can be quite large especially when the system size is large. For $N = 300$, three layers suffice. With this choice we were able to perform converged simulations.

Bibliography

[1] L. Berthier and G. Biroli. Theoretical perspective on the glass transition and amorphous materials. *Rev. Mod. Phys.*, 83:587–645, 2011.

[2] G. L. Hunter and E. R. Weeks. The physics of the colloidal glass transition. *Rep. Prog. Phys.*, 75:066501, 2012.

[3] V. Lubchenko and P. G. Wolynes. Theory of structural glasses and supercooled liquids. *Ann. Rev. Phys. Chem.*, 58:235–266, 2007.

[4] H. Bassler. Viscous-flow in supercooled liquids analyzed in terms of transport-theory for random media with energetic disorder. *Phys. Rev. Lett.*, 58:767–770, 1987.

[5] R. Richert, K. Duvvuri, and L.-T. Duong. Dynamics of glass-forming liquids. vii. dielectric relaxation of supercooled tris-naphthylbenzene, squalane, and decahydroisoquinoline. *The Journal of Chemical Physics*, 118(4):1828–1836, 2003.

[6] S. Corezzi, M. Beiner, H. Huth, K. Schrter, S. Capaccioli, R. Casalini, D. Fioretto, and E. Donth. Two crossover regions in the dynamics of glass forming epoxy resins. *The Journal of Chemical Physics*, 117(5):2435–2448, 2002.

[7] R. Richert and C. A. Angell. Dynamics of glass-forming liquids. v. on the link between molecular dynamics and configurational entropy. *The Journal of Chemical Physics*, 108(21):9016–9026, 1998.

[8] R. Casalini, K. L. Ngai, and C. M. Roland. Connection between the high-frequency crossover of the temperature dependence of the relaxation time and the change of intermolecular coupling in glass-forming liquids. *Phys. Rev. B*, 68:014201, Jul 2003.

[9] A. Mandanici, M. Cutroni, and R. Richert. Dynamics of glassy and liquid m-toluidine investigated by high-resolution dielectric spectroscopy. *The Journal of Chemical Physics*, 122(8):–, 2005.

[10] D. Sidebottom, R. Bergman, L. Börjesson, and L. M. Torell. Two-step relaxation decay in a strong glass former. *Phys. Rev. Lett.*, 71:2260–2263, Oct 1993.

[11] T. R. Kirkpatrick, D. Thirumalai, and P. G. Wolynes. Scaling concepts for the dynamics of viscous liquids near an ideal glassy state. *Phys. Rev. A*, 40:1045–1054, 1989.

[12] T. R. Kirkpatrick and D. Thirumalai. p-spin-interaction spin-glass models: Connections with the structural glass problem. *Phys. Rev. B*, 36:5388–5397, 1987.

[13] T. R. Kirkpatrick and D. Thirumalai. Mean-field soft-spin potts glass model: Statics and dynamics. *Phys. Rev. B*, 37:5342–5350, 1988.

[14] Michael E. Fisher and A. Nihat Berker. Scaling for first-order phase transitions in thermodynamic and finite systems. *Phys. Rev. B*, 26:2507–2513, Sep 1982.

[15] H.A. Kramers. Brownian motion in a field of force and the diffusion model of chemical reactions. *Physica*, 7(4):284 – 304, 1940.

[16] W. Kob. Supercooled liquids, the glass transition, and computer simulations. *eprint arXiv:cond-mat/0212344*, December 2002.

[17] David R Reichman and Patrick Charbonneau. Mode-coupling theory. *Journal of Statistical Mechanics: Theory and Experiment*, 2005(05):P05013, 2005.

[18] C. Dasgupta, A.V. Indrani, S Ramaswamy, and M.K. Phani. Is there a growing correlation length near the glass transition? *Europhys. Lett.*, 15:307–312, 1991.

[19] C. Donati, S. C. Glotzer, and Peter H. Poole. Growing spatial correlations of particle displacements in a simulated liquid on cooling toward the glass transition. *Phys. Rev. Lett.*, 82:5064–5067, 1999.

[20] S. C. Glotzer, V. N. Novikov, and T. B. Schroder. Time-dependent, four-point density correlation function description of dynamical heterogeneity and decoupling in supercooled liquids. *The Journal of Chemical Physics*, 112:509–512, 2000.

[21] E. Flenner and G. Szamel. Dynamic heterogeneity in a glass forming fluid: Susceptibility, structure factor, and correlation length. *Phys. Rev. Lett.*, 105:217801, 2010.

[22] R. Yamamoto and A. Onuki. Heterogeneous diffusion in highly supercooled liquids. *Phys. Rev. Lett.*, 81:4915–4918, Nov 1998.

[23] J. P. Bouchaud and G. Biroli. On the Adam-Gibbs-Kirkpatrick-Thirumalai-Wolynes scenario for the viscosity increase in glasses. *J. Chem. Phys.*, 121:7347–7354, 2004.

[24] L. Berthier, G. Biroli, J.-P. Bouchaud, L. Cipelletti, D. E. Masri, D. L'Hote, F. Ladieu, and M. Pierno. Direct experimental evidence of a growing length scale accompanying the glass transition. *Science*, 310(5755):1797–1800, 2005.

[25] L. Berthier, G. Biroli, J.-P. Bouchaud, W. Kob, K. Miyazaki, and D. R. Reichman. Spontaneous and induced dynamic fluctuations in glass formers. i. general results and dependence on ensemble and dynamics. *J. Chem. Phys.*, 126:184503, 2007.

[26] C. Toninelli, M. Wyart, L. Berthier, G. Biroli, and J.-P. Bouchaud. Dynamical susceptibility of glass formers: Contrasting the predictions of theoretical scenarios. *Phys. Rev. E*, 71:041505, 2005.

[27] H. Kang, T. R. Kirkpatrick, and D. Thirumalai. Manifestation of random first-order transition theory in wigner glasses. *Phys. Rev. E*, 88:042308, Oct 2013.

[28] H. M. Lindsay and P. M. Chaikin. Elastic properties of colloidal crystals and glasses. *J. Chem. Phys.*, 76:3774–3781, 1982.

[29] R. O. Rosenberg and D. Thirumalai. Order-disorder transition in colloidal suspensions. *Phys. Rev. A*, 36:5690–5700, 1987.

[30] R. O. Rosenberg, D. Thirumalai, and R. D. Mountain. Liquid, crystalline and glassy states of binary charged colloidal suspensions. *Journal of Physics: Condensed Matter*, 1:2109, 1989.

[31] S. Alexander, P. M. Chaikin, P. Grant, G. J. Morales, P. Pincus, and D. Hone. Charge renormalization, osmotic pressure, and bulk modulus of colloidal crystals - Theory. *J. Chem. Phys.*, pages 5776–5781, 1984.

[32] S. Sanyal and A. K. Sood. Brownian dynamics simulation of dense binary colloidal mixtures. I. structural evolution and dynamics. *Phys. Rev. E*, 52:4154–4167, 1995.

[33] D. Thirumalai. Liquid and crystalline states of monodisperse charged colloidal particles. *J. Phys. Chem.*, 93:5637–5644, 1989.

[34] M. E. Fisher, Y. Levin, and X. Li. The interaction of ions in an ionic medium. *J. Chem. Phys.*, 101:2273–2282, 1994.

[35] J. D. Weeks. One and two component hard sphere models for the structure of metallic glasses:an integral equation approach. *Phil. Mag.*, 35:1345–1363, 1977.

[36] R. O. Rosenberg and D. Thirumalai. Structure and dynamics of screened-Coulomb colloidal liquids. *Phys. Rev. A*, 33:4473–4476, 1986.

[37] T. R. Kirkpatrick and D. Thirumalai. Random solutions from a regular density functional Hamiltonian - A static and dynamical theory of the structural glass transition. *J. Phys. A*, 22:L149–L155, 1989.

[38] T. R. Kirkpatrick and D. Thirumalai. Comparison between dynamical theories and metastable states in regular and glassy mean-field spin models with underlying first-order-like phase transitions. *Phys. Rev. A*, 37:4439–4448, 1988.

[39] U. Bengtzelius, W. Goetze, and A. Sjolander. Dynamics of supercooled liquids and the glass-transition. *J. Phys. C*, 17:5915–5934, 1984.

[40] E. Leutheusser. Dynamical model of the liquid-glass transition. *Phys. Rev. A.*, 29(5):2765–2773, 1984.

[41] S. D. Wilke and J. Bosse. Relaxation of a supercooled low-density Coulomb fluid. *Phys. Rev. E.*, 59:1968–1975, 1999.

[42] D. Thirumalai, R. D. Mountain, and T. R. Kirkpatrick. Ergodic Behavior in supercooled liquids and in glasses. *Phys. Rev. A*, 39:3563–3574, 1989.

[43] J. E. Straub and D. Thirumalai. Exploring the energy landscape in proteins. *Proc. Natl. Acad. Sci.*, 90:809–813, 1993.

[44] C. Donati, S. Franz, S. C. Glotzer, and G. Parisi. Theory of non-linear susceptibility and correlation length in glasses and liquids. *J. Non-Cryst. Solids*, 307:215–224, 2002.

[45] J. P. Bouchaud and G. Biroli. Nonlinear susceptibility in glassy systems: A probe for cooperative dynamical length scales. *Phys. Rev. B.*, 72:064204, 2005.

[46] E. Flenner, M. Zhang, and G. Szamel. Analysis of a growing dynamic length scale in a glass-forming binary hard-sphere mixture. *Phys. Rev. E*, 83:051501, 2011.

[47] H. Sillescu. Heterogeneity at the glass transition: a review. *J. Non-Cryst. Solids*, 243:81–108, 1999.

[48] M. D. Ediger and P. Harrowell. Perspective: Supercooled liquids and glasses. *J. Chem. Phys.*, 137:080901, 2012.

[49] R. E. Nettleton and M. S. Green. Expression in terms of molecular distribution functions for the entropy density in an infinite system. *J. Chem. Phys.*, 29:1365–1370, 1958.

[50] A. Leocmach and H. Tanaka. Roles of icosahedral and crystal-like order in the hard spheres glass transition. *Nat. Comm.*, 3:974, 2012.

[51] H. Tanaka, T. Kawasaki, H. Shintani, and K. Watanabe. Critical-like behaviour of glass-forming liquids. *Nat. Mater.*, 9:324–331, 2010.

[52] H. Shintani and H. Tanaka. Frustration on the way to crystallization in glass. *Nat. Phys.*, 2:1745–2473, 2006.

[53] K. Watanabe and H. Tanaka. Direct observation of medium-range crystalline order in granular liquids near the glass transition. *Phys. Rev. Lett.*, 100:158002, Apr 2008.

[54] P. J. Steinhardt, D. R. Nelson, and M. Ronchetti. Bond-orientational order in liquids and glasses. *Phys. Rev. B*, 28:784–805, 1983.

[55] W. Lechner and C. Dellago. Accurate determination of crystal structures based on averaged local bond order parameters. *The Journal of Chemical Physics*, 129(11), 2008.

[56] R. D. Mountain and D. Thirumalai. Dynamical aspects of anisotropic correlations in supercooled liquids. *The Journal of Chemical Physics*, 92(10):6116–6123, 1990.

[57] A.C. Ladd, W. E. Alley, and B. Alder. Structural relaxation in dense hard-sphere fluids. *Journal of Statistical Physics*, 48(5-6):1147–1156, 1987.

[58] B. Bernu, Y. Hiwatari, and J.P. Hansen. A molecular dynamics study of the glass transition in binary mixtures of soft-spheres. *J. Phys. C*, 18:L371–L376, 1985.

[59] B. Bernu, J.P. Hansen, Y. Hiwatari, and G. Pastore. Soft-sphere model for the glass transition in binary-alloys - Pair structure and self-diffusion. *Phys. Rev. A*, 36:4891–4903, 1987.

[60] J. N. Roux, J. L. Barrat, and J. P. Hansen. Dynamical diagnostics for the glass transition in soft-sphere alloys. *Journal of Physics: Condensed Matter*, 1(39):7171, 1989.

[61] P. Rein ten Wolde, M. J. RuizMontero, and D. Frenkel. Numerical calculation of the rate of crystal nucleation in a lennardjones system at moderate undercooling. *The Journal of Chemical Physics*, 104(24):9932–9947, 1996.

[62] F. Sausset and G. Tarjus. Growing static and dynamic length scales in a glass-forming liquid. *Phys. Rev. Lett.*, 104:065701, Feb 2010.

[63] P. Charbonneau and G. Tarjus. Decorrelation of the static and dynamic length scales in hard-sphere glass formers. *Phys. Rev. E*, 87:042305, Apr 2013.

[64] A. H Elcock. Models of macromolecular crowding effects and the need for quantitative comparisons with experiment. *Current Opinion in Structural Biology*, 20(2):196 – 206, 2010.

[65] H. X. Zhou, G. Rivas, and A. P. Minton. Macromolecular crowding and confinement: Biochemical, biophysical, and potential physiological consequences. *Annual Review of Biophysics*, 37:375–397, 2008.

[66] O. Medalia, I. Weber, A. S. Frangakis, D. Nicastro, G. Gerisch, and W. Baumeister. Macromolecular architecture in eukaryotic cells visualized by cryoelectron tomography. *Science*, 298(5596):1209–1213, 2002.

[67] S. R. McGuffee and Adrian H. Elcock. Diffusion, crowding & protein stability in a dynamic molecular model of the bacterial cytoplasm. *PLoS Comput Biol*, 6(3):e1000694, 03 2010.

[68] K. Devanand and J. C. Selser. Asymptotic behavior and long-range interactions in aqueous solutions of poly(ethylene oxide). *Macromolecules*, 24(22):5943–5947, 1991.

[69] K.L. Linegar, A.E. Adeniran, A.F. Kostko, and M.A. Anisimov. Hydrodynamic radius of polyethylene glycol in solution obtained by dynamic light scattering. *Colloid Journal*, 72(2):279–281, 2010.

[70] A. G. Ogston and C. F. Phelps. The partition of solutes between buffer solutions and solutions containing hyaluronic acid. *Biochem. J.*, 78(4):827–0, 1961.

[71] A. P. Minton. Models for excluded volume interaction between an unfolded protein and rigid macromolecular cosolutes: Macromolecular crowding and protein stability revisited. *Biophysical Journal*, 88(2):971 – 985, 2005.

[72] B. C. McNulty, G. B. Young, and G. J. Pielak. Macromolecular crowding in the escherichia coli periplasm maintains alpha-synuclein disorder. *Journal of molecular biology*, 355:893–897, 2006.

[73] N. Tokuriki, M. Kinjo, S. Negi, M. Hoshino, Y. Goto, I. Urabe, and T. Yomo. Protein folding by the effects of macromolecular crowding. *Protein Science*, 13(1):125–133, 2004.

[74] D. Homouz, M. Perham, A. Samiotakis, M. S. Cheung, and P. Wittung-Stafshede. Crowded, cell-like environment induces shape changes in aspherical protein. *Proceedings of the National Academy of Sciences*, 105(33):11754–11759, 2008.

[75] S. I. Nakano, H. T. Karimata, Y. Kitagawa, and N. Sugimoto. Facilitation of rna enzyme activity in the molecular crowding media of cosolutes. *Journal of the American Chemical Society*, 131(46):16881–16888, 2009. PMID: 19874030.

[76] D. Kilburn, J. H. Roh, L. Guo, R. M. Briber, and S. A. Woodson. Molecular crowding stabilizes folded rna structure by the excluded volume effect. *Journal of the American Chemical Society*, 132(25):8690–8696, 2010.

[77] N. A. Denesyuk and D. Thirumalai. Crowding promotes the switch from hairpin to pseudoknot conformation in human telomerase rna. *Journal of the American Chemical Society*, 133(31):11858–11861, 2011.

[78] L. S. Lerman. A transition to a compact form of dna in polymer solutions. 68(8):1886–1890, 1971.

[79] S. C. Riemer and V. A. Bloomfield. Packaging of dna in bacteriophage heads: Some considerations on energetics. *Biopolymers*, 17(3):785–794, 1978.

[80] K. Richter, M. Nessling, and P. Lichter. Macromolecular crowding and its potential impact on nuclear function. *Biochimica et Biophysica Acta (BBA) - Molecular Cell Research*, 1783(11):2100 – 2107, 2008. Functional Architecture of the Cell Nucleus.

[81] M. Ueda and K. Yoshikawa. Phase transition and phase segregation in a single double-stranded dna molecule. *Phys. Rev. Lett.*, 77:2133–2136, Sep 1996.

[82] N. M. Toan, D. Marenduzzo, P. R. Cook, and C. Micheletti. Depletion effects and loop formation in self-avoiding polymers. *Phys. Rev. Lett.*, 97:178302, Oct 2006.

[83] F. Du, Z. Zhou, Z. Y. Mo, J. Z. Sh, J. Chen, and Y. Liang. Mixed macromolecular crowding accelerates the refolding of rabbit muscle creatine kinase: Implications for protein folding in physiological environments. *Journal of Molecular Biology*, 364:469–482, 2006.

[84] H. X. Zhou. Effect of mixed macromolecular crowding agents on protein folding. *Proteins: Structure, Function, and Bioinformatics*, 72(4):1109–1113, 2008.

[85] J. Batra, K. Xu, and H.-X. Zhou. Nonadditive effects of mixed crowding on protein stability. *Proteins: Structure, Function, and Bioinformatics*, 77(1):133–138, 2009.

[86] M. M. Waegele and F. Gai. Power-law dependence of the melting temperature of ubiquitin on the volume fraction of macromolecular crowders. *The Journal of Chemical Physics*, 134(9):095104, 2011.

[87] A. Kudlay, M. S. Cheung, and D. Thirumalai. Influence of the shape of crowding particles on the structural transitions in a polymer. *The Journal of Physical Chemistry B*, 116(29):8513–8522, 2012.

[88] E. P. O'Brien, J. E. Straub, B. R. Brooks, and D. Thirumalai. Influence of nanoparticle size and shape on oligomer formation of an amyloidogenic peptide. *The Journal of Physical Chemistry Letters*, 2(10):1171–1177, 2011.

[89] H. Reiss, H. L. Frisch, and J. L. Lebowitz. Statistical mechanics of rigid spheres. *The Journal of Chemical Physics*, 31(2):369–380, 1959.

[90] A. Soranno, I. Koenig, M. B. Borgia, H. Hofmann, F. Zosel, D. Nettels, and B. Schuler. Single-molecule spectroscopy reveals polymer effects of disordered proteins in crowded environments. *Proceedings of the National Academy of Sciences*, 111(13):4874–4879, 2014.

[91] J. S. Kim, V. Backman, and I. Szleifer. Crowding-induced structural alterations of random-loop chromosome model. *Phys. Rev. Lett.*, 106:168102, Apr 2011.

[92] D. K. Klimov and D. Thirumalai. Viscosity dependence of the folding rates of proteins. *Phys. Rev. Lett.*, 79:317–320, Jul 1997.

[93] D. Lhuillier. A simple model for polymeric fractals in a good solvent and an improved version of the flory approximation. *J. Phys. France*, 49(5):705–710, 1988.

[94] ésio B. Ramos. Macromolecular crowding and the sizes of neutral flexible polymer chains: The role of colloids sizes and concentrations. *Macromolecular Theory and Simulations*, 20(5):320–328, 2011.

[95] J. A. Aronovitz and D. R. Nelson. Universal features of polymer shapes. *Journal de physique*, 47:1445–1456, 1986.

[96] R. I. Dima and D. Thirumalai. Asymmetry in the shapes of folded and denatured states of proteins. *The Journal of Physical Chemistry B*, 108(21):6564–6570, 2004.

[97] K. Šolc and W. H. Stockmayer. Shape of a randomflight chain. *The Journal of Chemical Physics*, 54(6):2756–2757, 1971.

[98] J. D. Honeycutt and D. Thirumalai. Static properties of polymer chains in porous media. *The Journal of Chemical Physics*, 90(8):4542–4559, 1989.

[99] J. S. Kim and I. Szleifer. Depletion effect on polymers induced by small depleting spheres. *The Journal of Physical Chemistry C*, 114(48):20864–20869, 2010.

[100] V. V. Vasilevskaya, A. R. Khokhlov, Y. Matsuzawa, and K. Yoshikawa. Collapse of single dna molecule in poly(ethylene glycol) solutions. *The Journal of Chemical Physics*, 102(16):6595–6602, 1995.

[101] D. P. Goldenberg and B. Argyle. Minimal effects of macromolecular crowding on an intrinsically disordered protein: A small-angle neutron scattering study. *Biophysical Journal*, 106:905–914, 2014/04/16.

[102] B. R. Parry, I. V. Surovtsev, M. T. Cabeen, C. S. O'Hern, E. R. Dufresne, and C. Jacobs-Wagner. Glass-like properties and is fluidized by metabolic activity. *Cell*, 156:183–194, 2014.

[103] T. Veitshans, D. Klimov, and D. Thirumalai. Protein folding kinetics: timescales, pathways and energy landscapes in terms of sequence-dependent properties. *Folding and Design*, 2(1):1 – 22, 1997.

[104] J. K. Bhattacharjee, D. Thirumalai, and J. D. Bryngelson. Distribution Function of the End-to-End Distance of Semiflexible Polymers. *ArXiv Condensed Matter e-prints*, September 1997.

[105] M. A. Cotter. Hard-rod fluid: Scaled particle theory revisited. *Phys. Rev. A*, 10:625–636, 1974.

[106] G. A. Vliegenthart and H. N. W. Lekkerkerker. Phase behavior of colloidal rod-sphere mixtures. *The Journal of Chemical Physics*, 111(9):4153–4157, 1999.

[107] P. G. de Gennes. *Scaling Concepts in Polymer Physics*. Cornell University Press, 1979.

[108] M. Hinczewski, X. Schlagberger, M. Rubinstein, O. Krichevsky, and R. R. Netz. End-monomer dynamics in semiflexible polymers. *Macromolecules*, 42(3):860–875, 2009.

[109] T. Ando and J. Skolnick. Crowding and hydrodynamic interactions likely dominate in vivo macromolecular motion. *Proceedings of the National Academy of Sciences*, 107(43):18457–18462, 2010.

[110] T. Kawasaki, T. Araki, and H. Tanaka. Correlation between dynamic heterogeneity and medium-range order in two-dimensional glass-forming liquids. *Phys. Rev. Lett.*, 99:215701, Nov 2007.

[111] S. Jun and B. Mulder. Entropy-driven spatial organization of highly confined polymers: Lessons for the bacterial chromosome. *Proceedings of the National Academy of Sciences*, 103(33):12388–12393, 2006.

[112] S. Jun, D. Thirumalai, and B. Y. Ha. Compression and stretching of a self-avoiding chain in cylindrical nanopores. *Phys. Rev. Lett.*, 101:138101, Sep 2008.

[113] J. J. Jones, J. R. C. van der Maarel, and P. S. Doyle. Effect of nanochannel geometry on dna structure in the presence of macromolecular crowding agent. *Nano Letters*, 11(11):5047–5053, 2011.

[114] S.-H. Hong, E. Toro, K. I. Mortensen, M. A. D. de la Rosa, S. Doniach, L. Shapiro, A. J. Spakowitz, and H. H. McAdams. Caulobacter chromosome in vivo configuration matches model predictions for a supercoiled polymer in a cell-like confinement. *Proceedings of the National Academy of Sciences*, 110(5):1674–1679, 2013.

[115] S. Jun and A. Wright. Entropy as the driver of chromosome segregation. *Nat Rev Micro*, 8:600–607, 2010.

[116] L. A. Mirny. The fractal globule as a model of chromatin architecture in the cell. *Chromosome Research*, 19(1):37–51, 2011.

[117] H. Löwen, J. P. Hansen, and J. N. Roux. Brownian dynamics and kinetic glass transition in colloidal suspensions. *Phys. Rev. A*, 44:1169–1181, Jul 1991.

[118] T. Gleim, W. Kob, and K. Binder. How does the relaxation of a supercooled liquid depend on its microscopic dynamics? *Phys. Rev. Lett.*, 81:4404–4407, Nov 1998.

[119] G. Szamel and E. Flenner. Independence of the relaxation of a supercooled fluid from its microscopic dynamics: Need for yet another extension of the mode-coupling theory. *EPL (Europhysics Letters)*, 67(5):779, 2004.

[120] F. Hofling, T. Munk, E. Frey, and T. Franosch. Critical dynamics of ballistic and brownian particles in a heterogeneous environment. *The Journal of Chemical Physics*, 128(16):164517, 2008.

[121] A. M. Puertas. Aging of a hard-sphere glass: effect of the microscopic dynamics. *Journal of Physics: Condensed Matter*, 22(10):104121, 2010.

[122] M. P. Allen and D. J. Tildesley. *Computer Simulation of Liquids*. Oxford science publications. Oxford University Press, USA, reprint edition, June 1989.